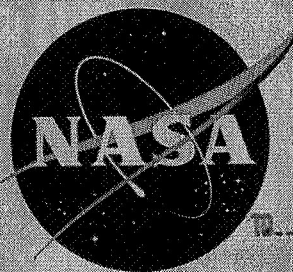


Copy 524

NASA TM X-536

NASA TM X-536



CLASSIFICATION MARKED
UNCLASSIFIED

By Authority of

1071-635 10/18/71

TECHNICAL MEMORANDUM

X-536

HYPERSONIC AERODYNAMIC CHARACTERISTICS OF SEVERAL SERIES OF LIFTING BODIES APPLICABLE TO REENTRY VEHICLE DESIGN

By William O. Armstrong

Langley Research Center
Langley Field, Va.

Declassified by authority of NASA
Classification Change Notices No. 215
Dated 12/31/71

FACILITY FORM 602

(ACCESSION NUMBER)

N71-75639

(THRU)

(PAGES)

97

(CODE)

none

(NASA CR OR TMX OR AD NUMBER)

(CATEGORY)

NATIONAL AERONAUTICS AND SPACE ADMINISTRATION
WASHINGTON

June 1961

NATIONAL AERONAUTICS AND SPACE ADMINISTRATION

TECHNICAL MEMORANDUM X-536

HYPERSONIC AERODYNAMIC CHARACTERISTICS OF SEVERAL SERIES
OF LIFTING BODIES APPLICABLE TO REENTRY
VEHICLE DESIGN*

By William O. Armstrong

SUMMARY

An investigation was carried out in the Langley 11-inch hypersonic tunnel at a Mach number of 9.6 to determine the longitudinal aerodynamic characteristics of a variety of lifting body shapes with sharp leading edges of varying cross section and nose bluntness. This paper presents the variations in lift, drag, and pitching-moment characteristics of these configurations due to changes in the body geometry and compares predicted values of maximum lift and maximum lift-drag ratio from Newtonian theory with those obtained experimentally. The results of limited tests on vehicles of varying leading-edge bluntness indicate that leading-edge radii representative of realistic vehicle design, in general, have small effects on the longitudinal characteristics of the vehicle.

The flat-bottom configurations were generally found to have higher values of maximum lift and lift-drag ratio than the round-bottom shapes. Eliminating the drag-producing, low-lift regions of the round-bottom half-cones did, however, provide a considerable increase in the maximum lift and lift-drag ratio of these configurations. Span-height ratio was found to produce different variations in the values of maximum lift and maximum lift-drag ratio of all elliptic half-cone bodies depending upon the body geometric parameter selected as a basis of comparison. Bodies of constant planform and, to a lesser degree, vehicles of constant volume showed an increase in maximum lift as body span-height ratio was increased. However, increasing body span-height ratio resulted in a reduction of maximum lift-drag ratio and an increase in maximum lift for vehicles of constant height. Variation in nose cant was found to produce little change in the maximum lift and lift-drag ratio of the flat-bottom half-cone series for values of nose bluntness ratio up to 0.6. A comparison of predictions of maximum lift and lift-drag ratio from Newtonian theory with values obtained experimentally indicates that this theory provides a useful means of estimating the trends produced in vehicles of these types.

INTRODUCTION

Numerous studies have pointed out improvements in corridor width, lateral and longitudinal range control, and peak decelerations which may be realized through use of aerodynamic lift during vehicle reentry into the earth's atmosphere (refs. 1 to 5). Since current trends in the design of orbital and lunar reentry vehicles focuses on configurations composed of full or partial conic, elliptic, and spheric bodies of revolution, it would be highly desirable to know the aerodynamic characteristics of these body shapes throughout the angle-of-attack range over which they might operate.

A rather complete discussion of the hypersonic longitudinal characteristics of sharp full-cone configurations is presented in reference 6. However, only a very limited amount of data is available for the more generalized body shapes at high Mach numbers and over a wide range of angle of attack.

In order to provide longitudinal data on a number of the basic body shapes mentioned, an extensive investigation was initiated in the Langley 11-inch hypersonic tunnel at a Mach number of 9.6 to study the hypersonic longitudinal characteristics of a wide variety of generalized body shapes of varying geometry. These configurations include full-cones, round-bottom half-cones, and elliptic half-cones of varying bluntness, flat-bottom half-cones of varying types and amounts of nose bluntness, and conic-sectored body shapes. Tests were conducted throughout an angle-of-attack range from 0° to 60° .

Most of the models studied during this investigation had sharp leading edges. However, practical reentry vehicle design generally requires some degree of nose and leading-edge rounding to provide satisfactory reentry heating characteristics in the vicinity of these leading edges. Several representative model shapes were tested with and without nose and leading-edge rounding to determine the effect of this blunting on the longitudinal characteristics of these configurations.

Some preliminary data obtained during this investigation are presented in reference 7. The present paper presents basic longitudinal aerodynamic characteristics of all the configurations tested during this study and compares the effects of such geometric variables as nose bluntness and cant of circular cones and body span-height ratio of elliptic cones on the maximum lift, maximum lift-drag ratio, and pitching moment of the various series of configurations tested. Newtonian predictions of the lift-drag characteristics are also included for a number of these configurations in order to access the usefulness of this theory in estimating the characteristics of these types of body shapes.

SYMBOLS

a	height of elliptic half-cone vertical semiaxis, in. (see fig. 1(d))
b	span of elliptic half-cone horizontal semiaxis, in. (see fig. 1(d))
C	linear viscosity coefficient
C_D	drag coefficient $F_D/q_\infty S$
C_f	average skin-friction coefficient
C_L	lift coefficient, $F_L/q_\infty S$
C_m	pitching-moment coefficient, $M_y/q_\infty S D$
D	maximum body diameter, in.
F_D	drag force, lb
F_L	lift force, lb
h	body height at juncture of nose and afterbody, in.
l	body length, in.
l_t	body length of the unblunted conic body, in.
L/D	lift-drag ratio, C_L/C_D
M_y	pitching moment, in-lb
N_{Re}	Reynolds number
q	dynamic pressure, lb/sq in.
q_e	effective dynamic pressure, lb/sq in.
r	local radius, in.
R	maximum body radius, in.

4

S	area, sq in.	
\bar{x}	horizontal distance from body base to center of gravity	
\bar{z}	vertical distance from body center line to center of gravity, in.	
α	angle of attack, angle between body axis and free-stream flow direction, deg	
δ_N	nose cant angle, deg (fig. 1(g))	L
θ_c	cone semiapex angle, deg	1
θ_{eq}	equivalent cone semiapex angle, $\tan^{-1} \frac{\sqrt{ab}}{l_t}$, deg	4
θ_{xy}	elliptic cone horizontal semiapex angle, deg	3
θ_{xz}	elliptic-cone vertical semiapex angle, deg	7
ϕ	body radial cutoff angle, deg	

Subscripts:

B	base
l	local
max	maximum
min	minimum
P	planform
w	wetted
∞	free stream

MODELS

Drawings showing the model details and dimensions of the configurations tested during this investigation are presented in figure 1. Photographs of representative models of each series of body shapes are presented in figure 2.

The first series of models shown in figure 1(a) consisted of a group of spherically blunted full cones varying in cone half-angle (θ_c) from 10° to 40° and having a nose bluntness ratio (h/R) equal to 0.2. The nose bluntness ratio of these and subsequent models is defined as the ratio of the height between the nose tangency point and the model axis to the base radius. The series of spherically blunted round-bottom half-cones shown in figure 1(b) also varied in cone half-angle from 10° to 40° and in values of nose bluntness from $h/R = 0$ to $h/R = 0.6$. In order to obtain an end point when examining the effects of nose bluntness on the characteristics of the round-bottom half-cone bodies, a round-bottom quarter-spheric body (see fig. 1(c)) was also tested. The ellipsoidally blunted elliptic half-cone series (fig. 1(d)) varied in vertical semiapex angle (θ_{xz}) from 10° to 30° and in nose bluntness ratio from 0 to 0.4 for two values of body span-height ratio, $b/a = 0.5$ and $b/a = 2$. Tests were also made on a series of conic-sectored bodies shown in figure 1(e) for which nose bluntness ratio was varied from 0 to 0.4. One configuration series having a value of cone half-angle θ_c of 10° had a conic sector that varied from $\phi = 0^\circ$ (a half-cone) to a value of $\phi = 60^\circ$. A conic-sectored body series having a value of $\phi = 45^\circ$ was also tested for three values of cone half-angles, $\theta_c = 10^\circ$, 15° , and 20° .

Two series of flat-bottom half-cone bodies were also tested. Figure 1(f) shows a series of spherically blunted half-cone configurations varying in cone half-angle from 10° to 40° for two values of bluntness ratio, $h/R = 0$ and $h/R = 0.4$. Another series of flat-bottom configurations, shown in figure 1(g), consisted of a group of 10° half-angle cones varying in nose cant angle (δ_N) from 90° to 45° and in nose bluntness ratio from 0.2 to 0.8.

The centroid of the side-view area was chosen as the center-of-gravity position shown in figure 1 and represents the moment reference center used only for comparing the effects of varying vehicle geometry on the pitching-moment characteristics of the various model series. Maximum body diameter was used as the reference length for all the moment data presented.

APPARATUS AND TEST PROCEDURES

These tests were conducted in the Langley 11-inch hypersonic tunnel at an average Mach number of 9.6 and an average stagnation pressure of 1,350 in. Hg absolute. Stagnation temperature was maintained at an average value of 1,150° F for all test results presented. Test section Reynolds number based on the test conditions was approximately

0.11 $\times 10^6$ per inch. Absolute humidity was kept to a value less than 1.9×10^{-5} pounds of water per pound of dry air.

Lift, drag, and pitching moment were obtained by means of a six-component internal strain-gage balance mounted through the base of the model. The angle of attack of the models, the angle between the model axis and the free-stream flow direction, was measured optically by means of a lens prism attached to the model base which reflected a point-source light beam onto a calibrated scale. This method allowed the true angle of attack of the model to be determined irrespective of the deflection of the balance and sting under load. Base-pressure measurements were recorded during each test run; however, calculations showed that at a Mach number of 9.6, base-pressure corrections to the drag coefficient were negligible (much lower than the balance measuring accuracy) and were therefore neglected.

Test results for all the configurations considered in this investigation were obtained in the test-section core free from boundary-layer effects (approximately 4 inches square, ref. 8) except in the case of a few of the sharp-nose more slender configurations ($\theta_c = 10^\circ$) where nose sections did extend into the tunnel boundary layer at the higher angles of attack ($\alpha > 45^\circ$). This would be expected to have a negligible effect on the lift and drag forces of the configuration since the area affected would be very small in the nose region of these cones. However, pitching moment would be somewhat more questionable in this angle-of-attack range because of the large moment arm over which the incremental force changes would act. Therefore, the pitching-moment data presented for the more slender models in this angle-of-attack region should be useful only to indicate trends.

ACCURACY OF DATA

With base area as the reference area and body diameter as the reference length, the average probable errors in the force and moment coefficients for the various test points due to the force balance system are as follows:

C_L	± 0.06
C_D	± 0.04
C_m	± 0.06

Since average probable error is dependent upon the area and reference length of the configuration, these probable errors are representative of values for an average configuration studied during this investigation. The more slender model shapes had smaller than average areas and reference

lengths and could possibly have a probable error somewhat higher than those listed whereas the probable error for the larger half-angle bodies would be expected to be smaller.

The limited size of the bodies that could be tested during this investigation necessitated mounting these models on the balance in such a manner that the balance moment center was located some distance behind the model base. The calculated accuracy in the moment data was determined about a body reference center located at the juncture of the body axis and the base. Since errors in moment data are a function of balance measuring error in normal force times the transfer ratio (\bar{x}/D) as well as a function of measuring errors in moment, moment data presented about the model center of gravity could have a considerably larger probable error than that indicated. This is particularly true for the more slender configurations because of the increased moment transfer distance involved. For this reason, data about this more forward center-of-gravity location are useful only to indicate trends in the moment characteristics of these configurations about a somewhat more realistic moment center.

Since the strut mechanism of the 11-inch hypersonic tunnel can operate through a strut angle of only 30° , it was necessary to use a dual-position model-mounting procedure in order to cover the full angle-of-attack range presented in this paper. Two steps or runs were required for each model tested to cover the entire α range, 0° to 30° and 30° to 60° . The rather good agreement in the duplicated data near $\alpha = 30^\circ$, resulting from the overlapping between the two runs, indicates the accuracy with which data can be obtained using a dual-mounting procedure to cover a wide range of angle of attack.

Angle of attack was measured within $\pm 0.10^\circ$ of the nominal value and Mach number was determined to within ± 0.05 . The stagnation pressure was measured to an accuracy of ± 2.0 in. Hg.

PRESENTATION OF DATA

The basic longitudinal aerodynamic characteristics (C_L , C_D , L/D , and C_m) obtained during this investigation are presented in figures 3 to 24 for each of the configurations tested. For these basic data plots, the configuration base area was used as the reference area and the juncture of the model axis and base as the moment reference center.

In order to evaluate the effects of varying such geometric parameters as nose bluntness, body cross section, and nose cant, a comparative study was made of the longitudinal characteristics of the various

series of configurations investigated. The results of this comparison are presented in figures 25 to 34 and show the variation in $C_{L,max}$, $(L/D)_{max}$, and C_m as a function of the different geometric variables studied. When comparing the maximum lift characteristics of these configurations, the model projected planform area was chosen as the reference, rather than the base area used in figures 3 to 24, since it more nearly represents the lifting surface of the model and provides a more realistic basis for comparing the lift characteristics of the various body shapes. The pitching-moment comparisons were based on a more realistic, although arbitrary, moment center located at the centroid of the side-view area but still retained the body base area as the reference area in order to retain consistency with data presented in reference 7.

RESULTS AND DISCUSSION

Numerous shape variables, such as nose bluntness, body cross section, body apex angle, and leading-edge bluntness, have been studied for a variety of lifting bodies to determine the effect that these variations have on the aerodynamic characteristics of the configurations. Newtonian estimates, determined by use of unpublished closed-form expressions, of the lift and drag characteristics of both the elliptic and circular cone bodies also have been included and compared with results obtained experimentally on the body shapes.

In order to determine the variations that occur in the characteristics of a given vehicle design with and without nose and leading-edge rounding, tests were repeated on several representative configurations with rounded noses and leading edges. These configurations included a 10° half-angle spherically blunted half-cone body studied both as a round-bottom and a flat-bottom configuration along with a flat-bottom half-cone having a flat canted nose. A comparison of the results obtained on these bodies with and without rounding are presented in figure 24. These results show that leading-edge radii on the order of those associated with realistic vehicle designs ($r/R = 0.10$) generally have small effects on the overall longitudinal characteristics of these configurations throughout the angle-of-attack range. The differences that do occur are most noticeable in the very low and rather high ($\alpha > 40^\circ$) angle-of-attack range. The differences between configurations with sharp and blunted leading edges also tend to become more significant for low-fineness-ratio bodies having large canted noses as can be seen by comparing the result presented in figure 24(c) with that shown in figures 24(a) and (b). Lift-drag ratio, however, appears to show only negligible effects due to this blunting for all three configurations. Generally, then, it appears that the data presented in this

investigation for vehicles having sharp leading edges should be representative of the characteristics of a realistic vehicle design and provides a useful means of comparing the aerodynamic characteristics of a wide range of lifting body shapes. Of course, the effects of leading-edge rounding must be included in determining the characteristics of any finalized vehicle design.

Spherically Blunted Round- and Flat-Bottom Half-Cones

The effects of varying nose bluntness ratio on the values of $(L/D)_{\max}$ and $C_{L,\max}$ of the round-bottom half-cone series is presented in figure 25. It may be seen from this figure that both inviscid Newtonian theory and experiment show that values of $(L/D)_{\max}$ of the more slender half-cone bodies are substantially reduced due to slight nose bluntness. Nose bluntness caused relatively small reductions, however, in the values of $(L/D)_{\max}$ of the larger half-angle half-cones. Increasing the bluntness of the various half-cone bodies reduces the values of $(L/D)_{\max}$ of the configurations and these values approach that of a hemisphere at the higher values of bluntness ratio. Newtonian theory without viscous corrections gives relatively good predictions of the $(L/D)_{\max}$ values of the more blunt body shape; however, as expected, this theory overpredicts the $(L/D)_{\max}$ values of the more slender, higher $(L/D)_{\max}$ configurations where viscous effects become important.

In order to ascertain the extent that viscous forces account for the difference between experimental and predicted values of $(L/D)_{\max}$, estimates were made of the skin friction for several of the more slender sharp half-cone bodies at zero angle of attack. These estimates were made by using the following equation obtained from reference 9 and modified for cones as suggested in reference 10:

$$C_f = \frac{1.328 \sqrt{C}}{\sqrt{N_{Re,l}}} \frac{S_w}{S} \frac{q_e}{q_\infty} \frac{2\sqrt{3}}{3}$$

For the tunnel conditions considered, a constant value of 0.86 was assumed for C . Since the value of $(L/D)_{\max}$ of these half-cone bodies occurs at an angle of attack near $\alpha = 0^\circ$, skin-friction approximations determined by using this procedure should provide a fairly reliable estimate of skin friction at $(L/D)_{\max}$. By combining these viscous corrections with inviscid Newtonian calculations, a difference of less than 5 percent was obtained between experimental and predicted values

of $(L/D)_{\max}$ for these sharp half-cone bodies. Therefore, the difference between experimental and inviscid Newtonian predictions of $(L/D)_{\max}$ shown in figure 25 is due primarily to viscous effects. Both experiment and Newtonian theory show that the value of $C_{L,\max}$ is increased by increasing cone half-angle regardless of the body nose bluntness. This increase is due to the increase in the ratio of the lifting surface area to planform area as cone half-angle is increased.

Figure 26 presents experimental results and Newtonian predictions of the values of $(L/D)_{\max}$ and $C_{L,\max}$ for a series of spherically blunted flat-bottom and round-bottom half-cone bodies of varying cone half-angle. Results are presented for two values of nose bluntness ratio, $h/R = 0$ and $h/R = 0.4$. As pointed out in reference 7, both experiment and theory show that the more slender flat-bottom configurations have a higher $(L/D)_{\max}$ than the round-bottom configurations. However, as cone angle is increased, the difference in $(L/D)_{\max}$ is reduced until for a cone half-angle of about 40° there is essentially no difference between the round-bottom and the flat-bottom configurations. Although increasing the bluntness ratio is shown to reduce the magnitude of the $(L/D)_{\max}$ value of these bodies, the $(L/D)_{\max}$ characteristics of these configurations follow the same trend regardless of nose bluntness.

As previously mentioned, $C_{L,\max}$ of the round-bottom half-cone bodies increases with increasing cone half-angle as predicted by theory. The $C_{L,\max}$ of the flat-bottom bodies, on the other hand, is not as greatly affected by varying cone half-angle. Theoretical predictions show a very gradual reduction in $C_{L,\max}$ with increasing θ_c due to an increase in the downward force of the upper conic surface, whereas experimental data show an increase in $C_{L,\max}$ for the flat-bottom series as θ_c increases up to a value of $\theta_c = 30^\circ$. To explain this behavior, it should be pointed out that results presented in reference 11 show that flat lifting surfaces operating at high angles of attack ($C_{L,\max}$ occurs at $\alpha \approx 50^\circ$ for these configurations) experience a reduction in surface pressure near the leading edge due to cross-flow effects over the lifting surface. Since the geometry of these models is such that the proportion of the area affected by the pressure reduction is reduced as θ_c increases, $C_{L,\max}$ increases with increasing θ_c . However, as θ_c continues to increase, the influence of the upper surface becomes overriding and the trend in $C_{L,\max}$ follows that predicted by theory.

It can be seen from figure 26 that the value of $C_{L,max}$ is substantially greater for the more slender flat-bottom bodies than for the round-bottom bodies. However, for the larger half-angle cones the reverse is true and $C_{L,max}$ is greater for the round-bottom shapes. The crossover is shown both experimentally and theoretically to occur at a value of θ_c near 35° . Nose bluntness does not produce any notable changes in the trends of $C_{L,max}$ of either of these body shapes but is shown to increase the value of $C_{L,max}$ for both body series.

Trends in the pitching-moment data about the center of gravity for two values of nose bluntness ratio are shown in figure 27 throughout the angle-of-attack range of the investigation. For convenience of presentation, this figure shows data for a round-bottom half-cone series throughout an angle-of-attack range from -60° to 60° . In order to compare the effect of body orientation, it should be noted that data for the round-bottom configurations over the angle-of-attack range from 0° to -60° may also be considered as representing data for a flat-bottom half-cone body.

The important thing to notice from figure 27 is that most of the bodies (both flat-bottom and round-bottom) exhibit essentially neutral stability about the centroid of side-view area throughout the angle-of-attack range. Thus relatively small control forces would be required for trim about this center-of-gravity location. The more slender round-bottom and flat-bottom configurations ($\theta_c = 10^\circ$), however, are relatively stable in the higher angle-of-attack range.

Flat-Bottom Half-Cones of Varying Nose Bluntness and Cant

Figure 28 presents the $(L/D)_{max}$ and $C_{L,max}$ characteristics of a series of flat-bottom 10° half-angle half-cones of varying nose bluntness and nose cant. This figure shows that both experimental and theoretical values of $C_{L,max}$ and $(L/D)_{max}$ of these body shapes exhibit little change due to varying nose cant for a given value of nose bluntness up to bluntness ratios of about 0.6. Thus it appears that for values of $h/R < 0.6$, nose cant can be tailored to provide the desired pitch characteristics of a given body as shown in reference 7 without regard to its effect on $C_{L,max}$ or $(L/D)_{max}$ for $\theta_c = 10^\circ$. As bluntness ratio is increased to 0.8, increasing nose cant is shown to reduce both $C_{L,max}$ and $(L/D)_{max}$ up to a nose cant of approximately 75° . Further increases in cant result in increased values of both $C_{L,max}$ and $(L/D)_{max}$.

Newtonian theory considerably overpredicts the values of $C_{L,max}$ for the less blunt body shapes but appears to agree fairly well with experiment for the more blunt configurations. This overprediction is again due to the previously discussed large leading-edge losses associated with the less blunt shape. As bluntness is increased, the ratio of the area affected by the leading edge to the overall lifting area is reduced, and this fact explains the closer agreement between theory and experiment for the blunt models.

Overprediction of $(L/D)_{max}$, using inviscid Newtonian theory, of the less blunt body shapes is due largely to the increased influence of viscous effects on these higher $(L/D)_{max}$ configurations rather than to loss in lift near the leading edge. This is true because $(L/D)_{max}$ occurs at an angle of attack ($\alpha < 30^\circ$) well below the angle of attack at which cross flow becomes important. (See ref. 11.)

The moment characteristics of this series of body shapes were discussed in reference 7.

Conic-Sectored Bodies

In an effort to evaluate the effects of eliminating the drag-producing, low-lift regions of the round-bottom conic half-bodies, tests were made on a series of conic-sectored bodies which varied the body radial cutoff angle from a value of $\phi = 0^\circ$ (half-cone) to $\phi = 60^\circ$. The results of these tests are presented in figure 29 and show $C_{L,max}$ and $(L/D)_{max}$ of the sectored body to $C_{L,max}$ and $(L/D)_{max}$ of the half-cone body plotted against body radial cutoff angle (ϕ).

For the sharp-nose configurations, Newtonian theory estimates of the variation in the ratio of $C_{L,max}$ of the sectored body to $C_{L,max}$ of the half-body show a rather gradual initial rate of increase in this ratio with increasing radial cutoff angle; however, the increase in this ratio shows a more accelerated rate of change as values of radial cutoff angle continue to increase above $\phi = 30^\circ$. This type of variation in the ratio of $C_{L,max}$ with ϕ should be expected since the ratio of the lifting area to planform area increases very slowly as radial cutoff angle increases from the half-cone configuration. However, as ϕ continues to increase, the ratio of lift producing area to planform area continues to increase until at the higher values of ϕ almost all the exposed area is primarily lift producing. Experimental results follow approximately the same trend as predicted by theory up to values of $\phi \approx 45^\circ$. Above this value of ϕ , experimental results show a marked

fall off from the predicted results. This fall-off is again due to the reduced pressure near the leading edge which, at these higher values of ϕ , is felt primarily as a loss in lift. This reduction in pressure near the vehicle leading edge occurs regardless of the value of cutoff angle. For small values of ϕ (bodies approaching the half-cone configuration) this reduction occurs on the side or nonlifting area of the vehicle and has little or no effect on lift. However, for the higher values of ϕ ($\phi > 45^\circ$) this reduction occurs primarily over a lift-producing area of the configuration, and experimental results would be expected to fall below the predicted values of the ratio of $C_{L,max}$ of the sector to $C_{L,max}$ of the half-cone.

The predicted ratio of $(L/D)_{max}$ of the sector to $(L/D)_{max}$ of the half-cone appears to vary in approximately a linear fashion with increasing ϕ . Experimental results tend to fall below the predicted value of this ratio because of the increased influence of the viscous effects as the value of $(L/D)_{max}$ of the model increases. The difference between the predicted and experimental results is further increased at the higher values of ϕ as shown in figure 29 because of the increasing loss in lift with increasing ϕ discussed previously.

Tests were also made which varied cone half-angle for a series of configurations having a value of radial cutoff angle equal to 45° . These tests show that the ratio of $(L/D)_{max}$ of the sector to $(L/D)_{max}$ of the half-cone increased substantially as θ_c was increased from 10° to 15° . A further increase in θ_c to 20° resulted in very little gain in this ratio. Increasing cone half-angle had little effect on the $C_{L,max}$ ratio of the various configurations.

Figure 29 also shows the effects of variations in radial cutoff angle for two values of bluntness ratio. The experimental results indicate that bluntness tends to increase the ratios of both $C_{L,max}$ and $(L/D)_{max}$; however, trends in these two parameters with increasing radial cutoff angle are similar for both the blunt and sharp body shapes.

Figure 30 presents the variation of pitching-moment coefficient with angle of attack for the various conic-sectored bodies just discussed. The moment reference center was again chosen as the centroid of the vehicle side-view area. These data show that for the sharp 10° half-angle conic-sectored series, the value of $C_{m,\alpha=0^\circ}$ increased as the value of ϕ increased. Longitudinal instability is increased in the low angle-of-attack range due to increasing radial cutoff angle; however, at the higher angles of attack, stability increases with increasing values of ϕ .

Blunting the model nose to a value of $h/R = 0.4$ produced a smaller increase in $C_{m,\alpha=0^\circ}$ as ϕ increased. The blunted configurations are generally shown to be longitudinally stable throughout the angle-of-attack range; however, the degree of stability at the higher angles of attack ($\alpha > 20^\circ$) is somewhat less than that shown for the sharp body shapes.

Increasing the cone half-angle for the $\phi = 45^\circ$ conic-sectored bodies reduced the nose-up pitching moment of both the sharp- and blunt-nose body shapes. Instability was also reduced through the low angle-of-attack range due to increased θ_c . On the other hand, increasing θ_c resulted in decreased longitudinal stability over the high angle-of-attack range ($\alpha > 25^\circ$). Increasing the nose bluntness ratio from 0 to 0.4 produced no change in the trends of these comparisons but did tend to reduce the degree of change in the pitching-moment characteristics of the configurations due to varying cone apex angle.

Elliptic Half-Cone Bodies

The effects of varying body span-height ratio on the longitudinal characteristics of a series of round-bottom elliptic half-cone bodies were also investigated. Since internal storage capacity is an important consideration from the standpoint of vehicle design, it would be interesting to observe the effect that varying span-height ratio (b/a) has on the lift and drag characteristics of these elliptic bodies having a constant body volume. In order to make this comparison for elliptic bodies of equal volume, they may be represented by an equivalent circular cone of the same length and of equal volume defined by the parameter

$$\theta_{eq} = \tan^{-1} \frac{\sqrt{ab}}{l_t}$$

Figure 31 shows the variation in $C_{L,max}$ and $(L/D)_{max}$ with θ_{eq} of these elliptic half-cones for values of b/a of 0.5, 1.0, and 2.0. Although the volume of this equivalent circular cone is exact for the sharp or unblunted configurations only, the error in volume due to nose bluntness shape is less than 1 percent for values of $h/R \leq 0.4$ and is, therefore, used for comparing the characteristics of the elliptic bodies of bluntness ratio 0.4 also.

It may be seen from figure 31 that $(L/D)_{max}$ is increased by increasing body span-height ratio regardless of equivalent cone half-angle or body bluntness. The value of $C_{L,max}$ is also shown to

increase with increasing b/a ; however, this effect appears to be reduced at the higher values of θ_{eq} . Predictions of $(L/D)_{max}$ using Newtonian theory show the same trends as those exhibited by the experimental data. As previously mentioned, however, for the more slender bodies the inviscid theory greatly overpredicts the magnitude of this parameter. Trends in $C_{L,max}$ predicted by theory also follow very closely those obtained experimentally. It should be noted that theory agrees quite well with experimental results for the elliptical bodies having span-height ratio of 0.5. The agreement between theory and experiment becomes increasingly poorer as b/a is increased and undoubtedly this change results from the reduction in leading-edge pressure associated with the more nearly flat-bottomed highly eccentric bodies.

Although the results presented in figure 31 provide a basis of comparing the effects of b/a for elliptic bodies of constant volume, body geometric parameters other than volume are of interest in comparing the longitudinal characteristics of a series of body shapes. The effects of body height and planform area should also be considered in evaluating the effect of b/a on the lift and drag characteristics of this series of elliptic half-cone body shapes. Figure 32 presents the variation of $C_{L,max}$ and $(L/D)_{max}$ with b/a for elliptic half-bodies of constant height with $\theta_{xz} = 20^\circ$ and for constant planform area with $\theta_{xy} = 20^\circ$ where body length is assumed constant. As previously pointed out, if vehicle volume is of primary concern, $(L/D)_{max}$ increases slightly with increasing b/a . The value of $C_{L,max}$ is also shown to increase slightly with increasing b/a for this case. If vehicle planform area is a controlling design criterion, an even more marked increase in $(L/D)_{max}$ is noted with increasing b/a . For this case the value of $C_{L,max}$ is slightly reduced by variation in b/a . In the case of a design where vehicle height is of primary importance, however, this figure shows that $(L/D)_{max}$ is slightly reduced due to increasing b/a whereas the value of $C_{L,max}$ shows some increase with increasing b/a . Similar trends are also shown for the blunted configurations, but the effects of variations in b/a on $(L/D)_{max}$ are somewhat reduced due to bluntness whereas the effects on $C_{L,max}$ are increased. Although Newtonian theory does not adequately predict the experimental results, especially for the more slender bodies, it does provide a useful means for predicting the trends in both $C_{L,max}$ and $(L/D)_{max}$.

The variation in pitching-moment coefficient of several elliptic half-cones of different span-height ratio with angle of attack are

shown in figure 33. Results are presented for two cone vertical semi-apex angles ($\theta_{xz} = 10^\circ$ and 20°) and two bluntness ratios ($h/R = 0$ and 0.4). This figure shows that the longitudinal stability is reduced as body span-height ratio is increased for both the $\theta_{xz} = 10^\circ$ and $\theta_{xz} = 20^\circ$ elliptic half-bodies. The nose-up pitching-moment coefficient near $\alpha = 0^\circ$ is also reduced as b/a increased for the $\theta_{xz} = 10^\circ$ body series but was not significantly changed with b/a for $\theta_{xz} = 20^\circ$ bodies. Similar trends were noted for the blunted configurations; however the nose-up pitching-moment coefficient was slightly increased and the vehicle stability reduced due to increased nose bluntness.

Ratio of Maximum Lift to Minimum Drag

It has been pointed out in reference 3 that large reductions in peak deceleration can be effected by utilizing variations in the resultant aerodynamic force of a reentry configuration. Since the degree of lift modulation attainable on a given vehicle is shown in reference 3 to be largely a function of the ratio of the reentry trajectory parameter ($C_{L,max}/C_{D,min}$), it would be of interest to compare the value of this ratio for the group of bodies discussed in this report. Figure 34 presents the value of $C_{L,max}/C_{D,min}$ as a function of $(L/D)_{max}$ for a large variety of these body shapes of varying body geometry and nose bluntness. This figure indicates that in general the value of $C_{L,max}/C_{D,min}$ varies over a relatively narrow band at a given $(L/D)_{max}$ and can be reasonably well approximated by the logarithmic relationship indicated in figure 34. This empirical relationship indicates that the ratio of the maximum lift to minimum drag of a vehicle is largely influenced by the maximum lift-drag ratio of the body. Thus for simple lifting-body configurations such as considered in this study, vehicles falling in a specified range of $(L/D)_{max}$ can be expected to provide very limited variation in the value of the ratio $C_{L,max}/C_{D,min}$ due to variation in configuration geometry.

CONCLUSIONS

An investigation has been made in the Langley 11-inch hypersonic tunnel at a Mach number of 9.6 to determine the longitudinal aerodynamic characteristics of a wide variety of lifting body shapes of varying cross section and nose bluntness. Analysis of the results obtained in this investigation have led to the following conclusions:

1. The results of limited tests on models of varying leading-edge bluntness indicate that leading-edge radii representative of realistic vehicle designs, in general, have small effects on the longitudinal characteristics of these bodies.

2. The more slender flat-bottom half-cone bodies have higher maximum lift-drag ratios and maximum lift coefficients than the round-bottom configurations of the same geometry and size. The value of maximum lift coefficient remains essentially constant for the flat-bottom half-cones as cone half-angle increases but shows a substantial increase with increasing cone half-angle for the round-bottom case. Maximum lift-drag ratio falls off with increasing cone half-angle until for a cone half-angle of 40° there is essentially no difference in this parameter for the round-bottom and flat-bottom half-cones.

3. Variations in nose cant are found to have little effect on the maximum lift coefficient and maximum lift-drag ratio of the flat-bottom half-cone series for values of nose-bluntness ratio up to about 0.6.

4. The results of tests on the conic-sectored bodies indicate that elimination of the drag-producing, low-lift regions of the round-bottom half-cones increased the maximum lift coefficient and maximum lift-drag ratio of the configurations.

5. For elliptic half-cone bodies of constant length, if body height is held constant, maximum lift-drag ratio decreased and maximum lift coefficient increased as body span-height ratio was increased. For bodies of constant volume, span-height ratio was found to have relatively small effects on both maximum lift coefficient and maximum lift-drag ratio. However, if the model planform area were held constant, the maximum lift-drag ratio increased markedly with increasing span-height ratio whereas maximum lift coefficient was slightly reduced.

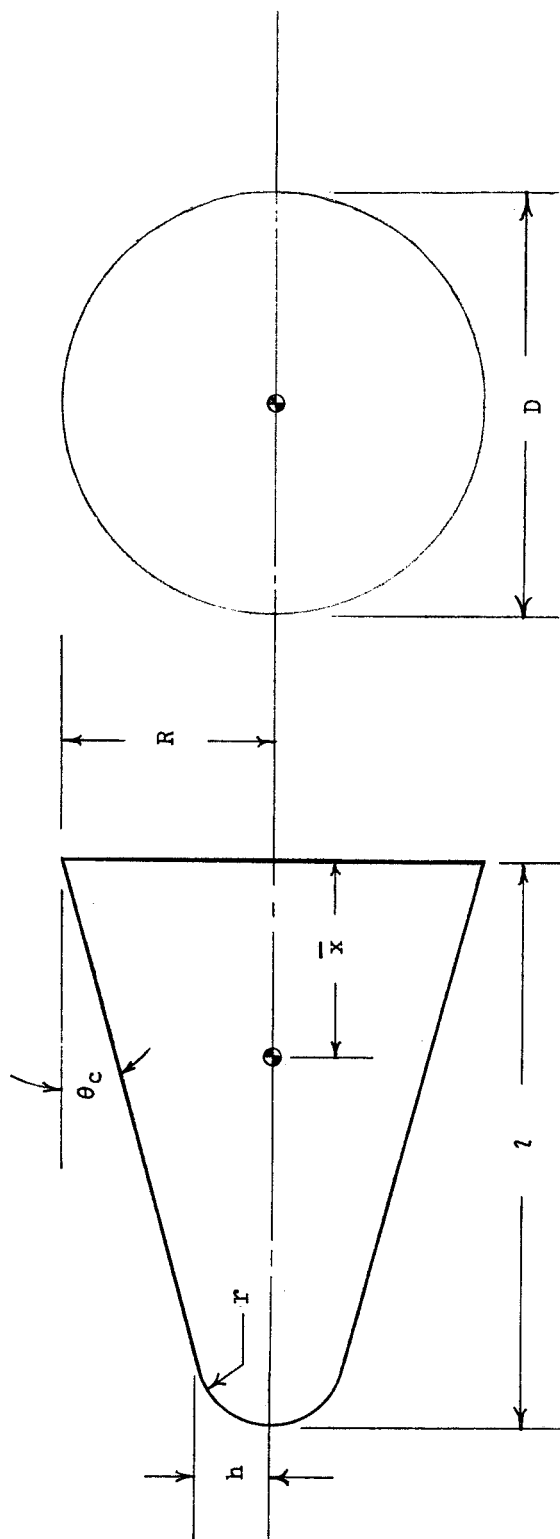
6. The value of the reentry trajectory parameter, the ratio of maximum lift coefficient to minimum drag coefficient, can be correlated as a simple relation in terms of the maximum lift-drag ratio of the body.

7. For these body shapes, Newtonian theory was found to provide an effective means of estimating the trends in the lift and drag characteristics and, in fact, also provided reasonable estimates of the magnitudes of these parameters where viscous effects and leading-edge pressure reductions were not of major importance.

Langley Research Center,
National Aeronautics and Space Administration,
Langley Field, Va., March 20, 1961.

REFERENCES

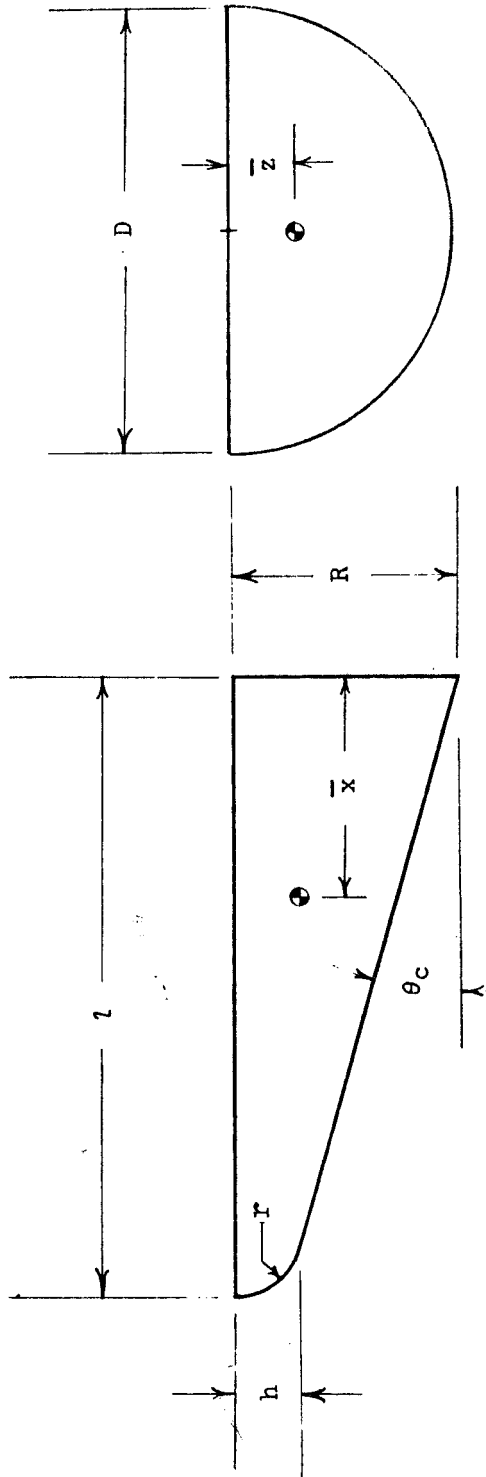
1. Eggers, Alfred J., Jr., Allen, H. Julian, and Neice, Stanford E.: A Comparative Analysis of the Performance of Long-Range Hypervelocity Vehicles. NACA Rep. 1382, 1958. (Supersedes NACA TN 4046.)
2. Lees, Lester, Hartwig, Fredric W.; and Cohen, Clarence B.: Use of Aerodynamic Lift During Entry Into the Earth's Atmosphere. ARS Jour., vol. 29, no. 9, Sept. 1959, pp. 633-641.
3. Grant, Frederick C.: Importance of the Variation of Drag With Lift In Minimization of Satellite Entry Acceleration. NASA TN D-120, 1959.
4. Faget, Maxime A., Garland, Benjamine J., and Buglia, James J.: Preliminary Studies of Manned Satellites - Wingless Configurations: Nonlifting. NACA RM L58E07a, 1958.
5. Chapman, Dean R.: An Approximate Analytical Method for Studying Entry Into Planetary Atmospheres. NASA TR R-11, 1959. (Supersedes NACA TN 4276.)
6. Penland, Jim A.: Aerodynamic Force Characteristics of a Series of Lifting Cone and Cone-Cylinder Configurations at a Mach Number of 6.83 and Angles of Attack up to 130°. NASA TN D-840, 1961.
7. Armstrong, William O., Stainback, P. Calvin, and McLellan, Charles H.: The Aerodynamic-Force and Heat-Transfer Characteristics of Lifting Reentry Bodies. NASA TM X-352, 1960.
8. Bertram, Mitchel H.: Boundary-Layer Displacement Effects in Air at Mach Numbers of 6.8 and 9.6. NASA TR R-22, 1959. (Supersedes NACA TN 4133.)
9. Chapman, Dean R., and Rubesin, Morris W.: Temperature and Velocity Profiles in the Compressible Laminar Boundary Layer With Arbitrary Distribution of Surface Temperature. Jour. Aero. Sci., vol. 16, no. 9, Sept. 1949, pp. 547-565.
10. Eckert, Ernst R. G.: Survey on Heat Transfer at High Speeds. WADC Tech. Rep. 54-70, U.S. Air Force, Apr. 1954.
11. Bertram, Mitchel H., Feller, William V., and Dunavant, James C.: Flow Fields, Pressure Distributions, and Heat Transfer for Delta Wings at Hypersonic Speeds. NASA TM X-316, 1960.



θ_c , deg	10	20	30	40
h/R	0.2	0.2	0.2	0.2
R , in.	1.00	1.35	1.50	1.75
S_B , in. 2	3.14	5.71	7.00	9.58
S_B/S_P	1.25	.86	.53	.35
\bar{x} , in.	1.70	1.15	.83	.67
\bar{z} , in.	0	0	0	0
r , in.	.20	.29	.35	.46
l , in.	4.68	3.16	2.22	1.74

(a) Full-cone series.

Figure 1.- Model drawings. (Linear dimensions in inches.)

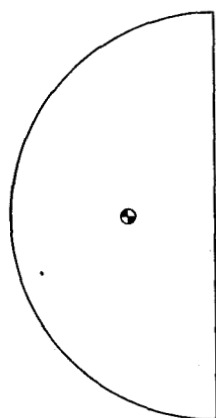


θ_c , deg	10					20					30					40				
h/R	0	0.2	0.4	0.6		0	0.2	0.4	0.6		0	0.2	0.4	0.6		∞	0.2	0.4	0.6	
R , in.	1.00	1.00	1.00	1.00		1.35	1.35	1.35	1.35		1.50	1.50	1.50	1.50		1.75	1.75	1.75	1.75	
S_B , in. ²	1.57	1.57	1.57	1.57		2.84	2.84	2.84	2.84		3.48	3.48	3.48	3.48		4.78	4.78	4.78	4.78	
S_P/S_B	3.61	3.50	3.00	2.57		1.75	1.71	1.50	1.36		1.10	1.06	.93	.89		.76	.70	.65	.63	
\bar{x} , in.	1.89	1.70	1.42	1.22		1.24	1.19	.98	.90		.87	.84	.75	.69		.70	.68	.63	.59	
\bar{z} , in.	.33	.34	.35	.39		.45	.46	.47	.50		.50	.51	.52	.54		.58	.59	.60	.62	
r , in.	0	.20	.41	.61		0	.29	.58	.86		0	.35	.69	1.04		0	.46	.91	1.37	
l , in.	5.67	4.68	3.74	2.76		3.71	3.16	2.71	2.03		2.59	2.22	1.89	1.48		2.08	1.74	1.57	1.32	

(b) Round-bottom half-cone series.

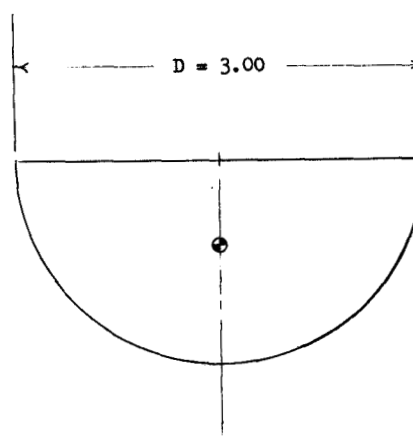
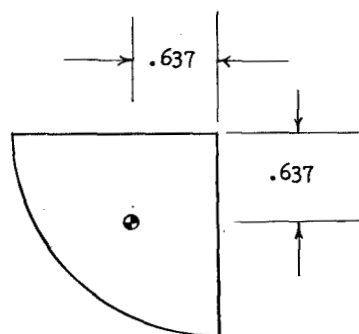
Figure 1.- Continued.

L-1437



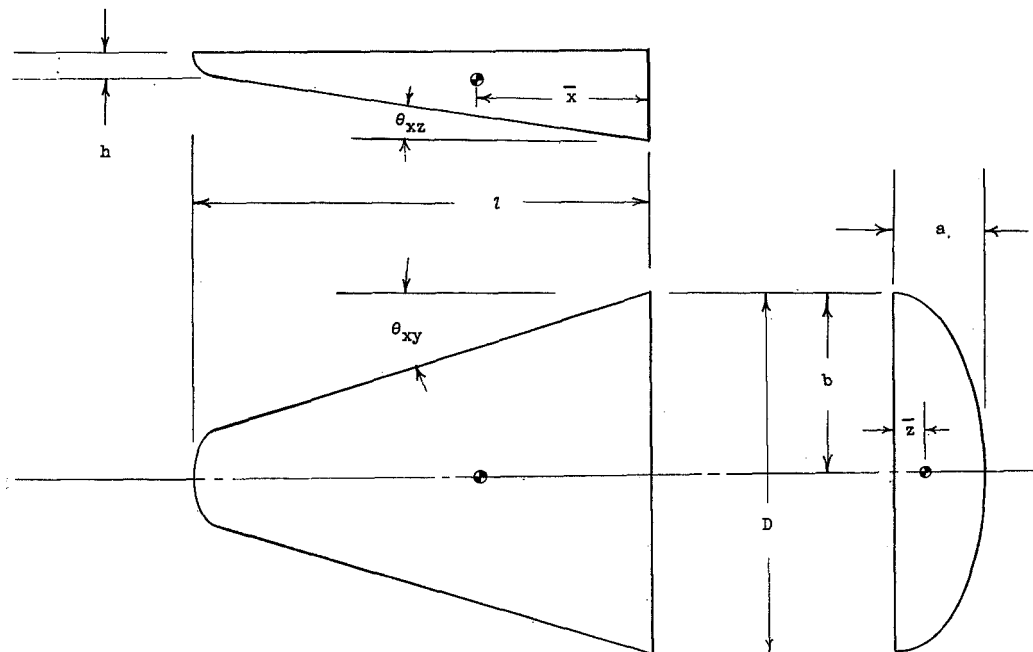
$$S_B = 3.14 \text{ in.}^2$$

$$S_B/S_P = 1.00$$



(c) Round-bottom quarter-spheric body.

Figure 1.- Continued.



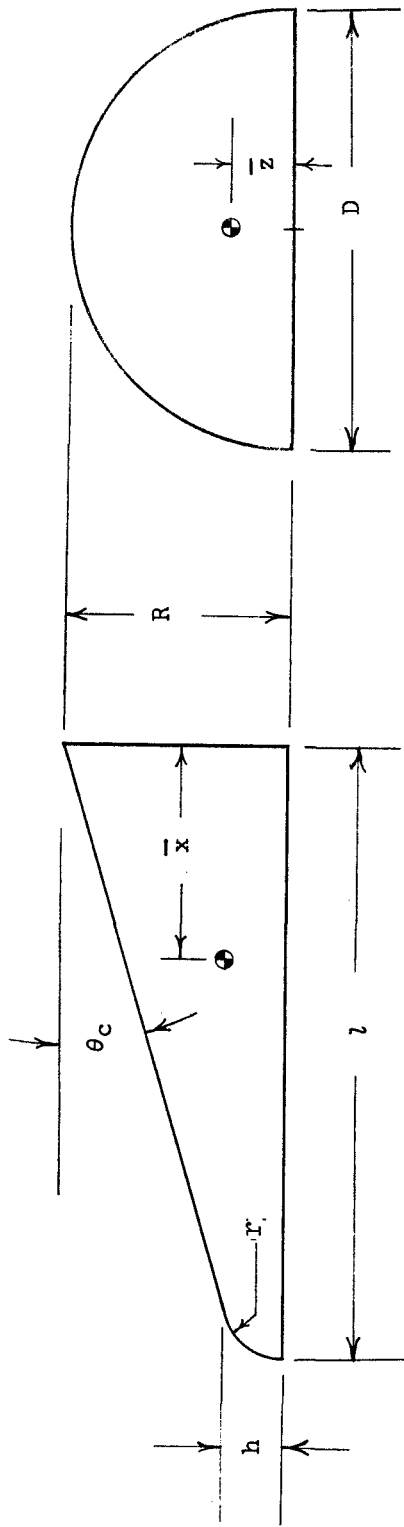
θ_{xz} , deg	10						20						30		
b/a	0.5			2.0			0.5			2.0			2.0		
h/R	0	0.2	0.4	0	0.2	0.4	0	0.2	0.4	0	0.2	0.4	0	0.2	0.4
b , in.	.50	.50	.50	2.00	2.00	2.00	.75	.75	.75	2.00	2.00	2.00	2.00	2.00	2.00
S_B , in. ²	.78	.78	.78	3.14	3.14	3.14	1.78	1.78	1.78	3.14	3.14	3.14	3.14	3.14	3.14
S_p/S_B	3.61	3.51	3.04	3.61	3.51	3.03	1.75	1.69	1.43	1.75	1.68	1.39	1.10	1.06	.95
\bar{x} , in.	1.89	1.83	1.54	1.89	1.83	1.54	1.38	1.32	1.21	.92	.89	.78	.58	.55	.54
z , in.	.33	.34	.36	.33	.34	.36	.50	.51	.53	.33	.34	.36	.33	.34	.35
l , in.	5.67	4.68	3.74	5.67	4.68	3.74	4.12	3.50	2.89	2.75	2.34	1.92	1.73	1.49	1.26
θ_{xy} , deg	5.1	5.1	5.1	19.4	19.4	19.4	10.3	10.3	10.3	36.0	36.0	36.0	49.2	49.2	49.2

(d) Elliptic half-cone series.

Figure 1.- Continued.



Figure 1.- Continued.



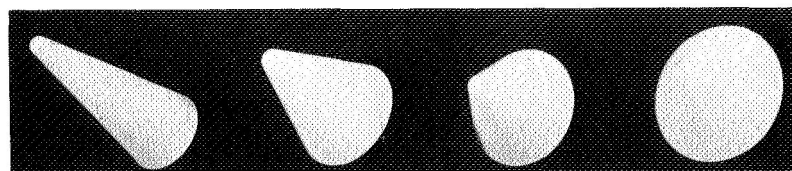
θ_c , deg	10		20		30		40	
h/R	0	0.4	0	0.4	0	0.4	0	0.4
R , in.	1.00	1.00	1.35	1.35	1.50	1.50	1.75	1.75
S_B , in. ²	1.57	1.57	2.85	2.85	3.54	3.54	4.80	4.80
S_P/S_B	3.61	3.00	1.75	1.50	1.10	.93	.76	.65
\bar{x} , in.	1.89	1.42	1.24	.98	.87	.75	.70	.63
\bar{z} , in.	.33	.35	.45	.47	.50	.52	.58	.60
r , in.	0	.41	0	.58	0	.69	0	.90
l , in.	5.67	3.74	3.71	2.71	2.59	1.89	2.08	1.57

(f) Spherically blunted flat-bottom half-cone series.

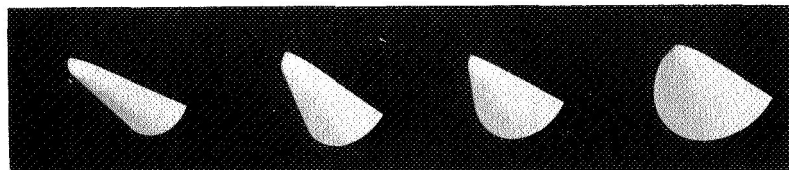
Figure 1.- Continued.



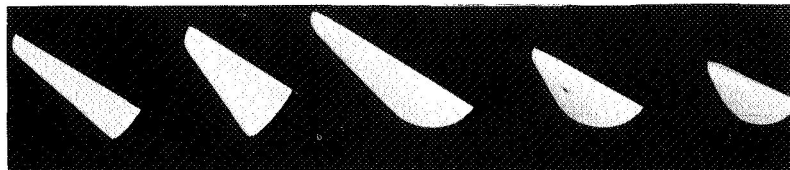
Figure 1. - Concluded.



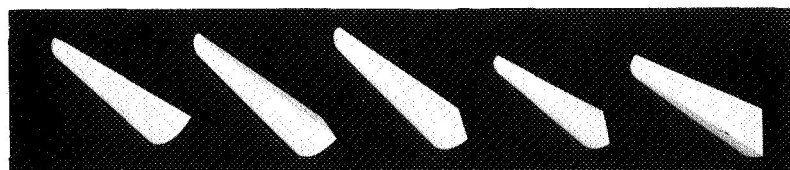
Full-cone series; $\theta_c = 10^\circ, 20^\circ, 30^\circ, 40^\circ$; $h/R = 0.2$.



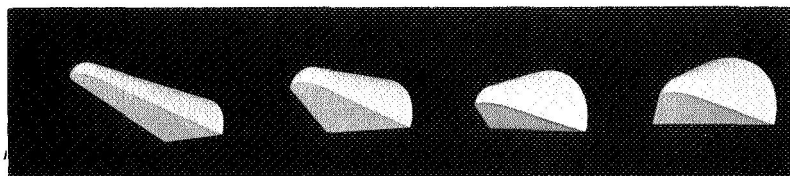
Round-bottom half-cone series; $\theta_c = 10^\circ, 20^\circ, 30^\circ, 40^\circ$; $h/R = 0.4$.



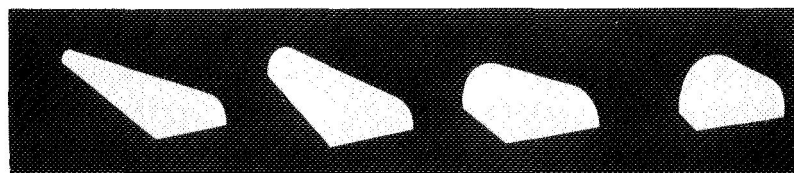
Elliptic half-cone series; $b/a = 0.5$; $\theta_{xz} = 10^\circ, 20^\circ$; $b/a = 2.0$;
 $\theta_{xz} = 10^\circ, 20^\circ, 30^\circ$; $h/R = 0.4$.



Conic-sectored series; $\phi = 0^\circ, 15^\circ, 30^\circ, 45^\circ, 60^\circ$; $\theta_c = 10^\circ$; $h/R = 0.4$.



Spherically blunted flat-bottom half-cone series;
 $\theta_c = 10^\circ, 20^\circ, 30^\circ, 40^\circ$; $h/R = 0.4$.

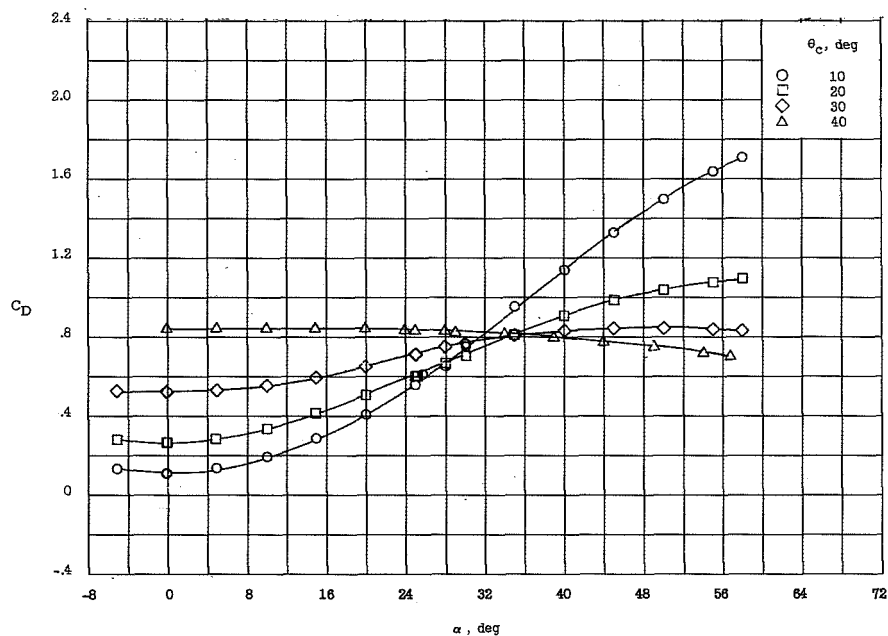
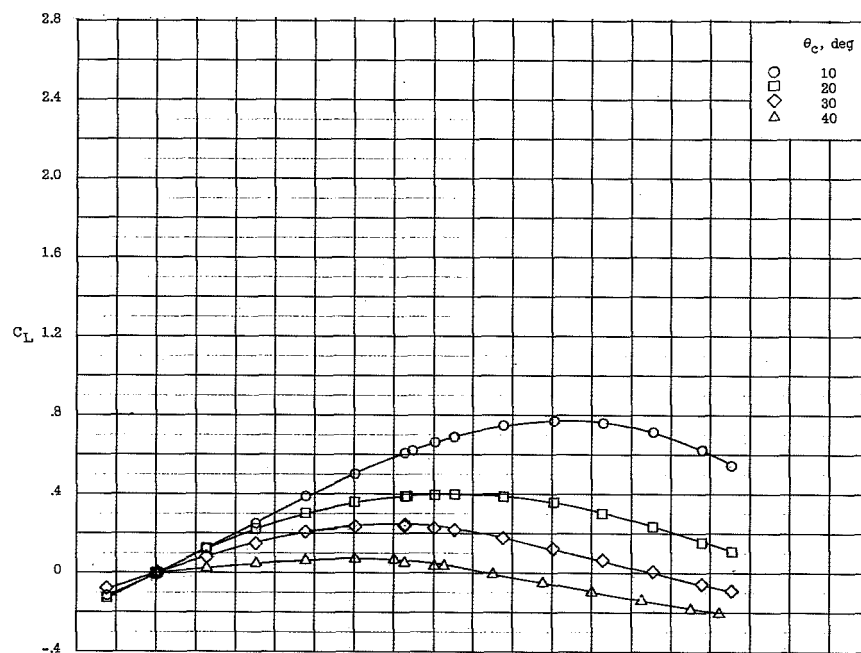


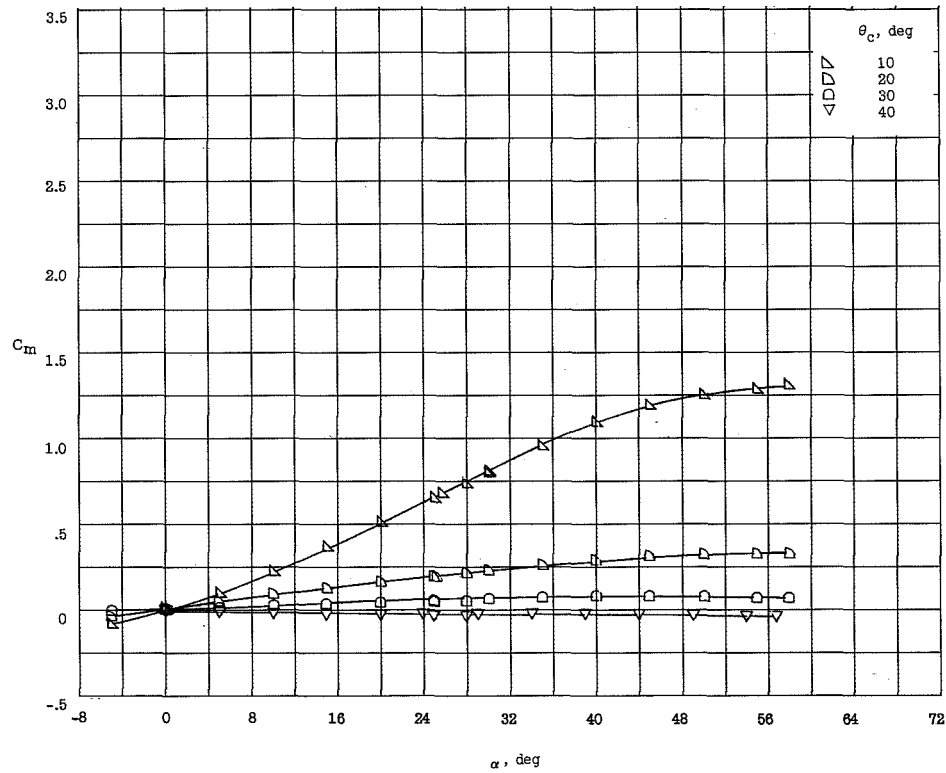
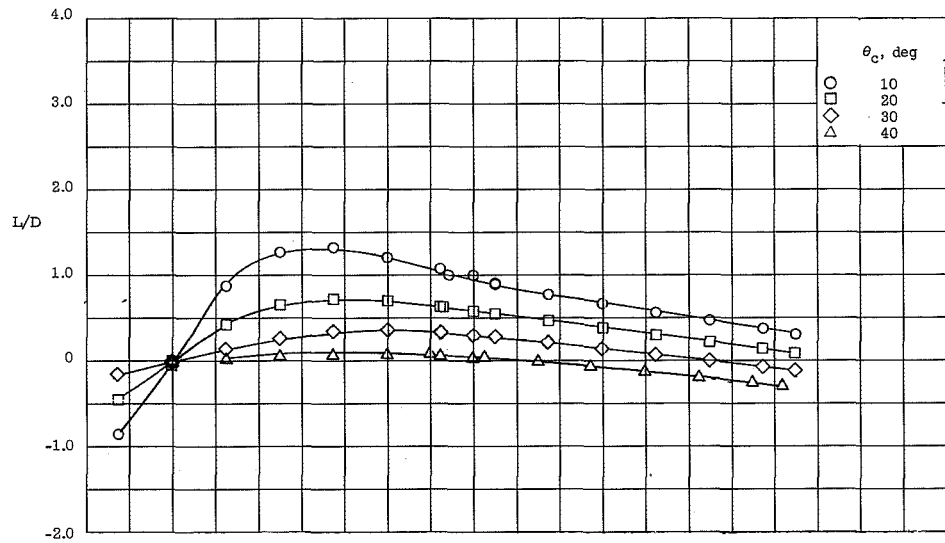
Flat-bottom half-cone series of varying nose bluntness and cant;
 $h/R = 0.2, 0.4, 0.6, 0.8$; $\theta_c = 10^\circ$; $\theta_N = 60^\circ$.

L-61-1064

Figure 2.- Photographs of representative models of each body series.

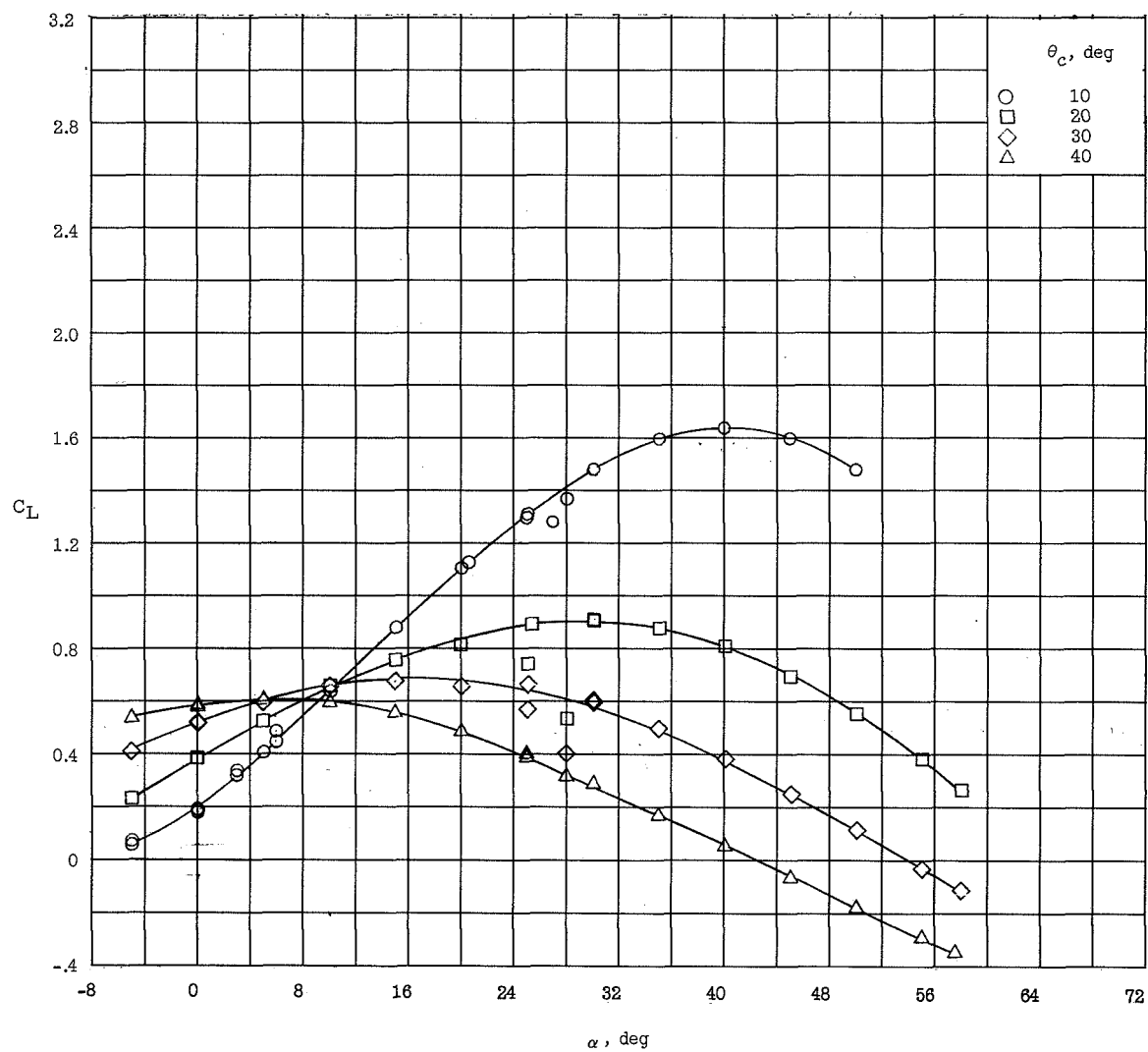
L-1437

(a) C_L and C_D .Figure 3.- Longitudinal characteristics of the full-cone series.
 $h/R = 0.2$.



(b) L/D and C_m about the body base.

Figure 3.- Concluded.

(a) C_L .Figure 4.- Longitudinal characteristics of the round-bottom half-cone series. $h/R = 0$.

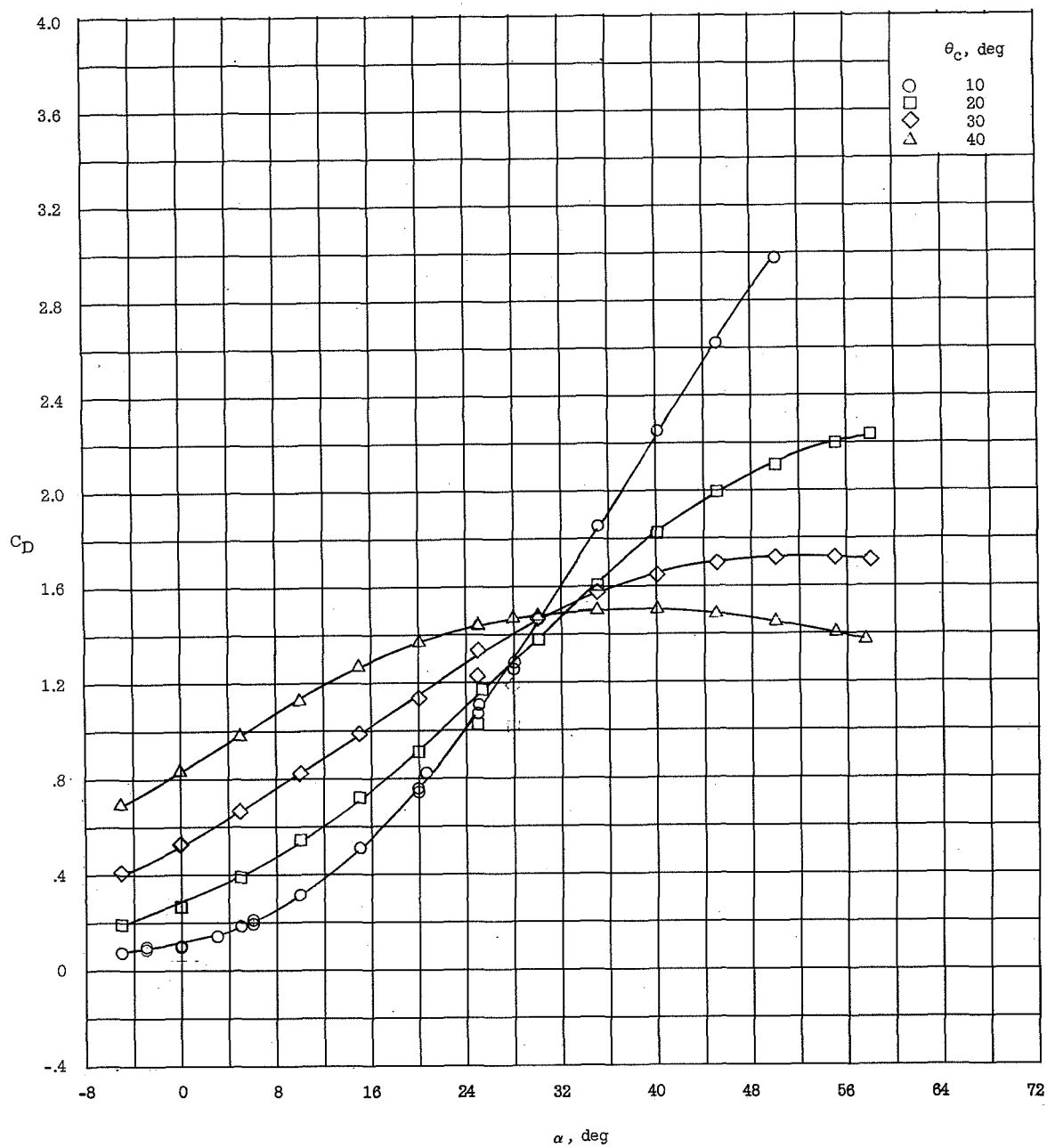
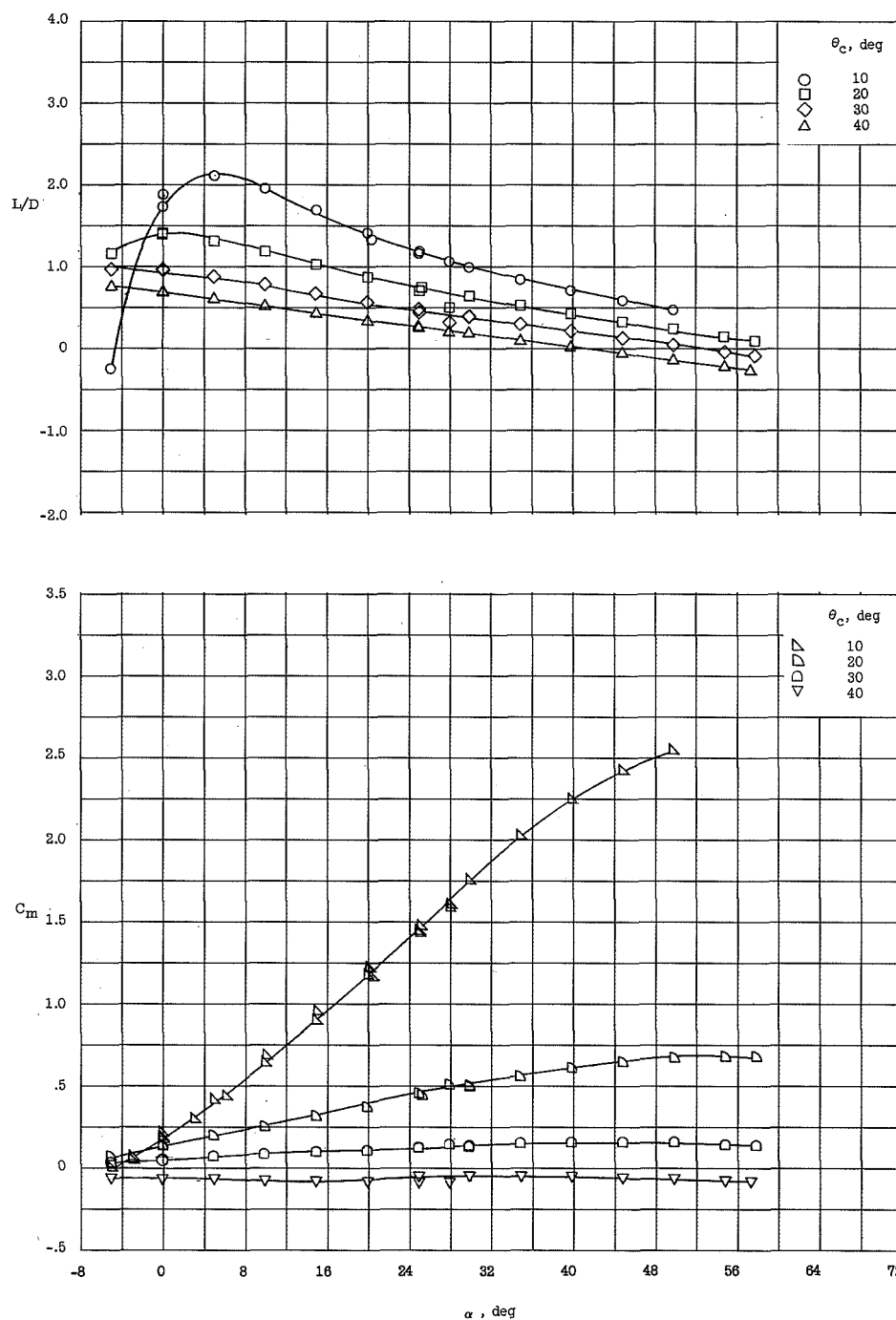
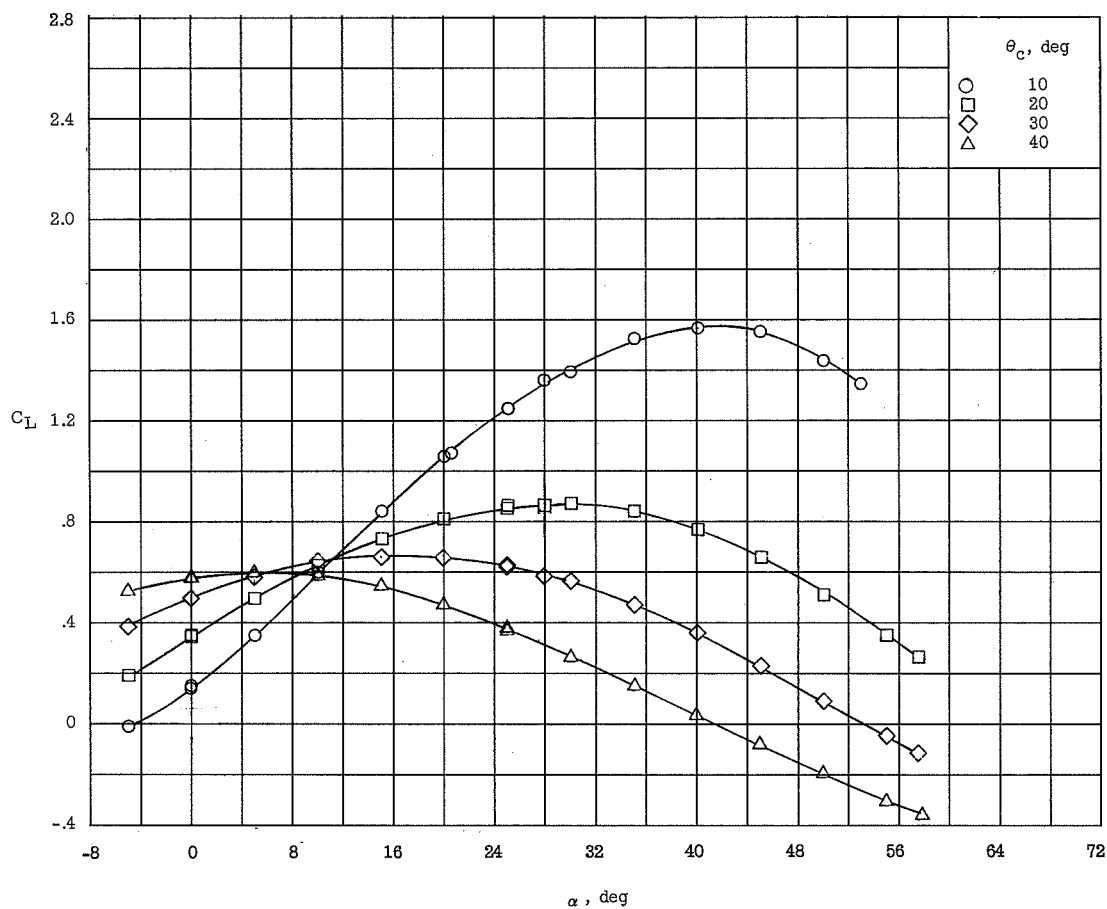
(b) C_D .

Figure 4.- Continued.

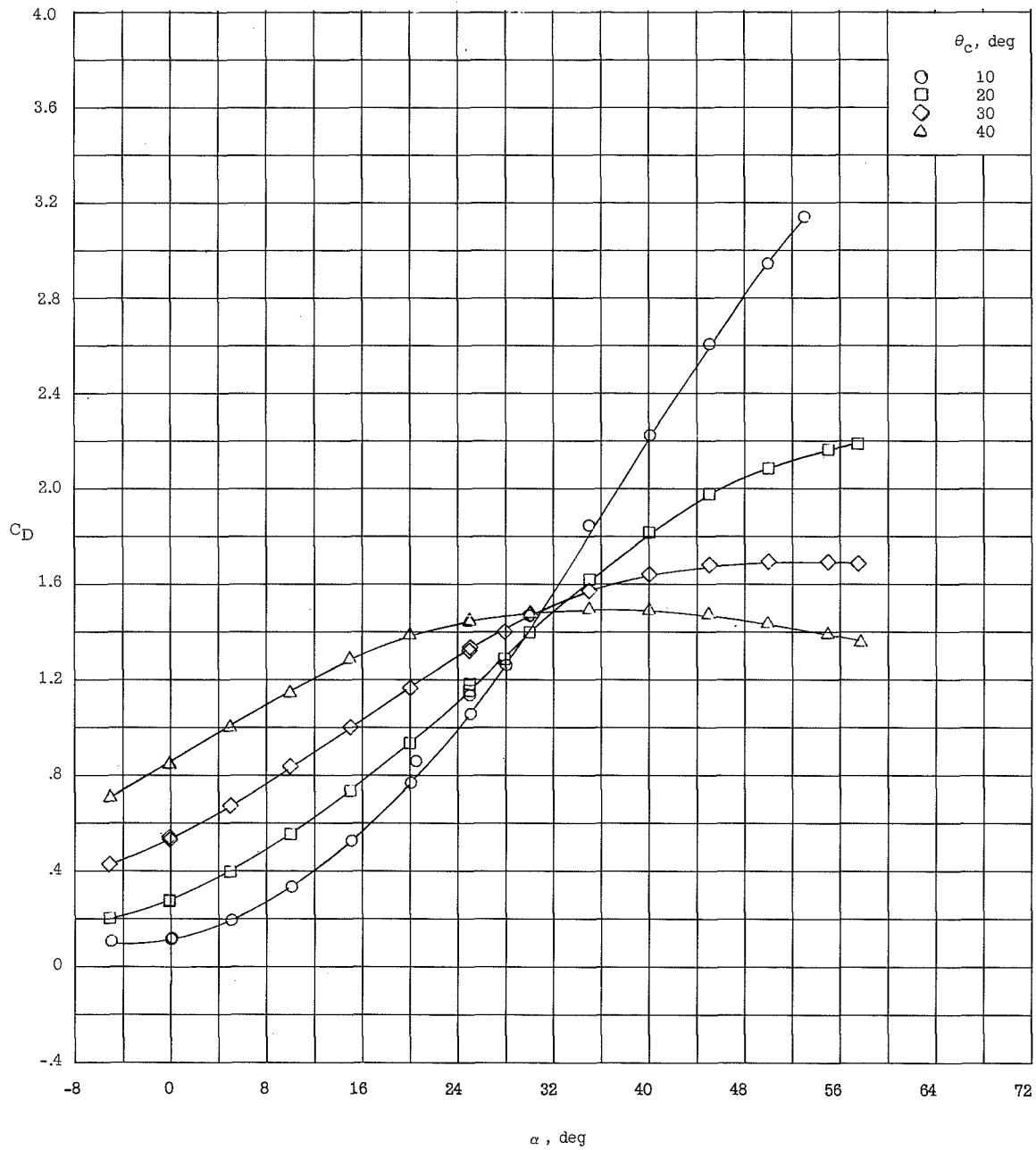


(c) L/D and C_m about the body base.

Figure 4.- Concluded.

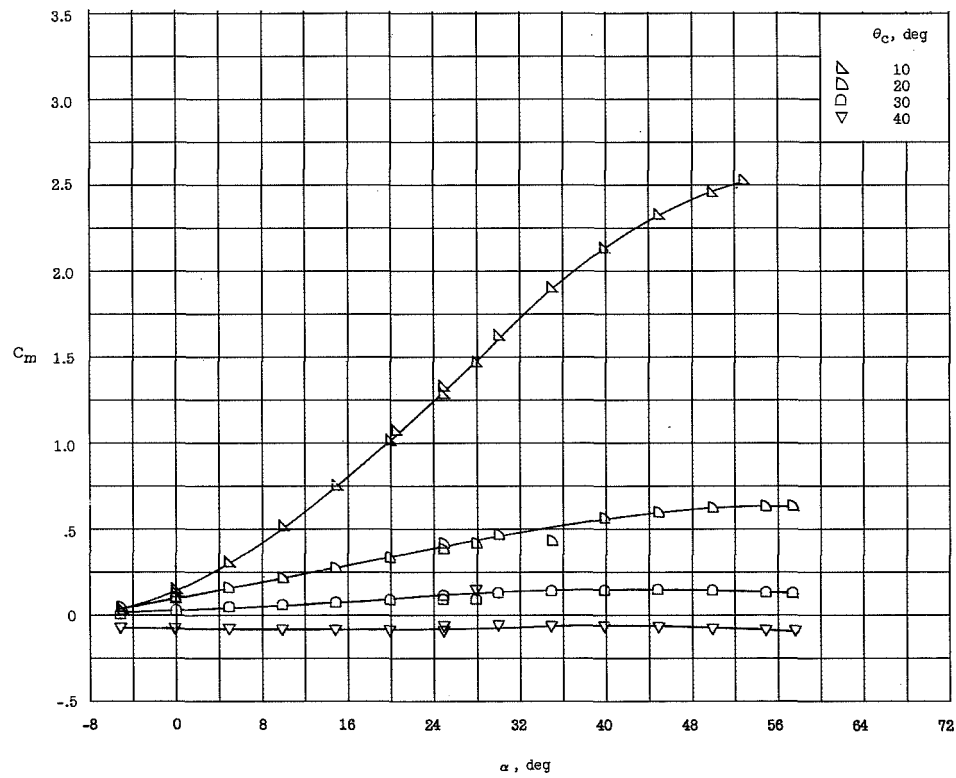
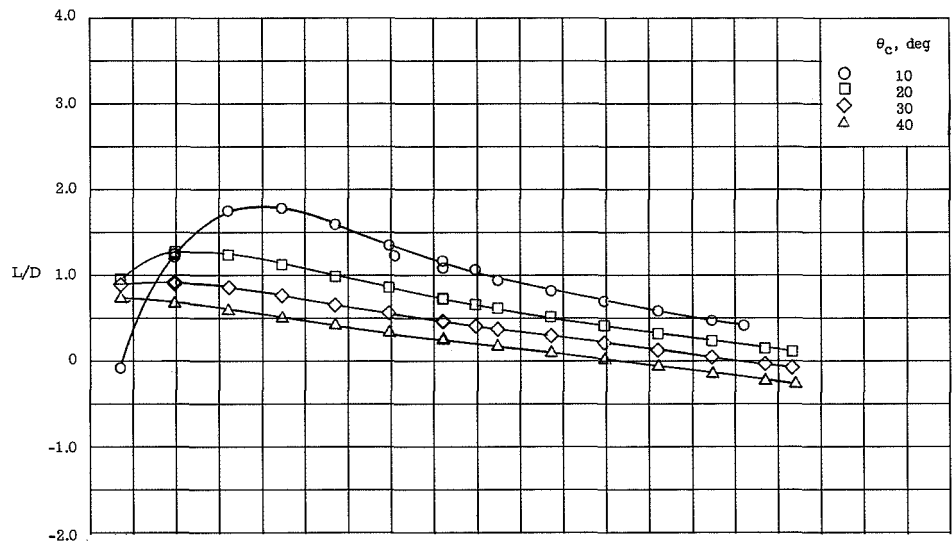
(a) C_L .Figure 5.- Longitudinal characteristics of the round-bottom half-cone series. $h/R = 0.2$.

L-1437



(b) C_D .

Figure 5.- Continued.



(c) L/D and C_m about the body base.

Figure 5.- Concluded.

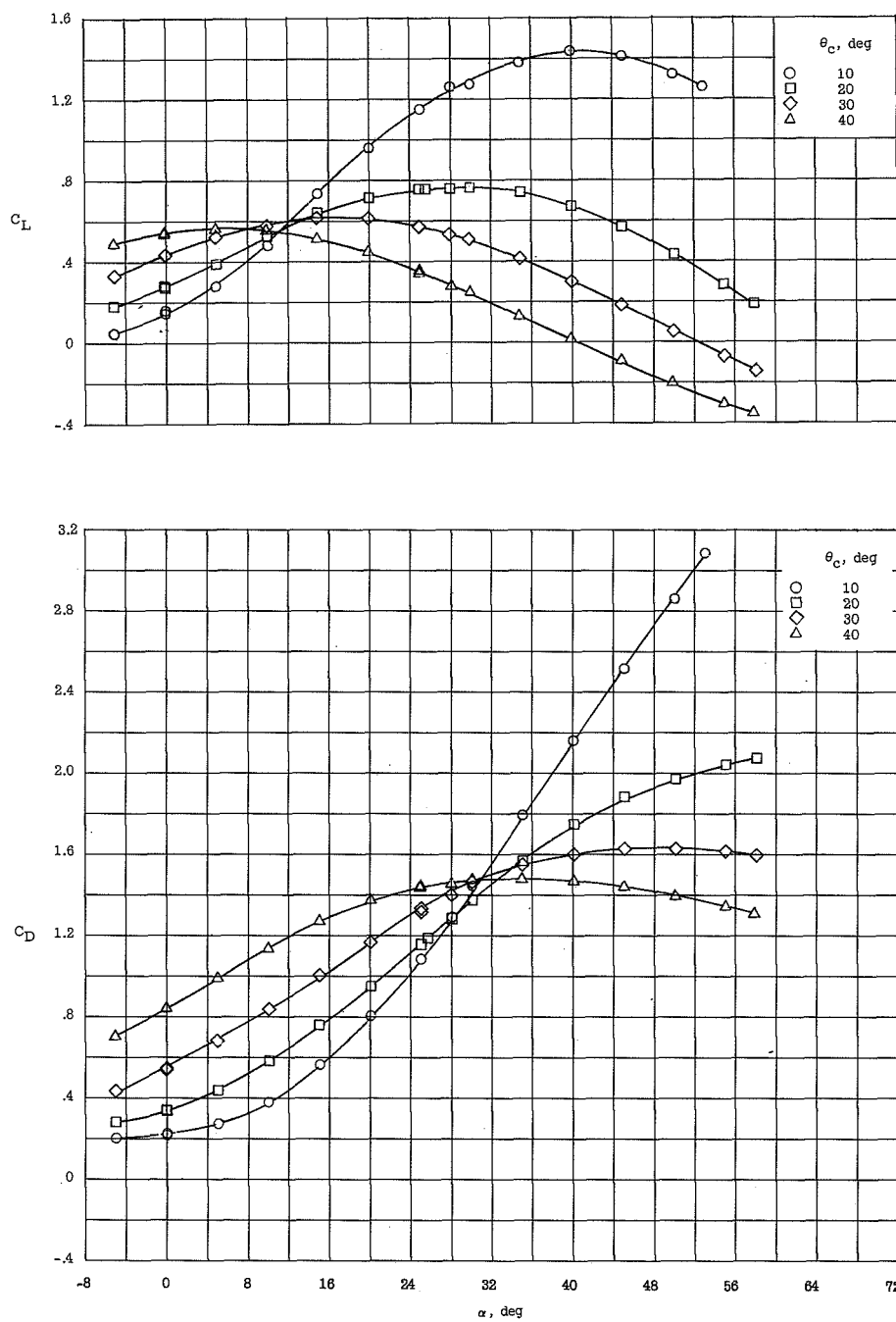
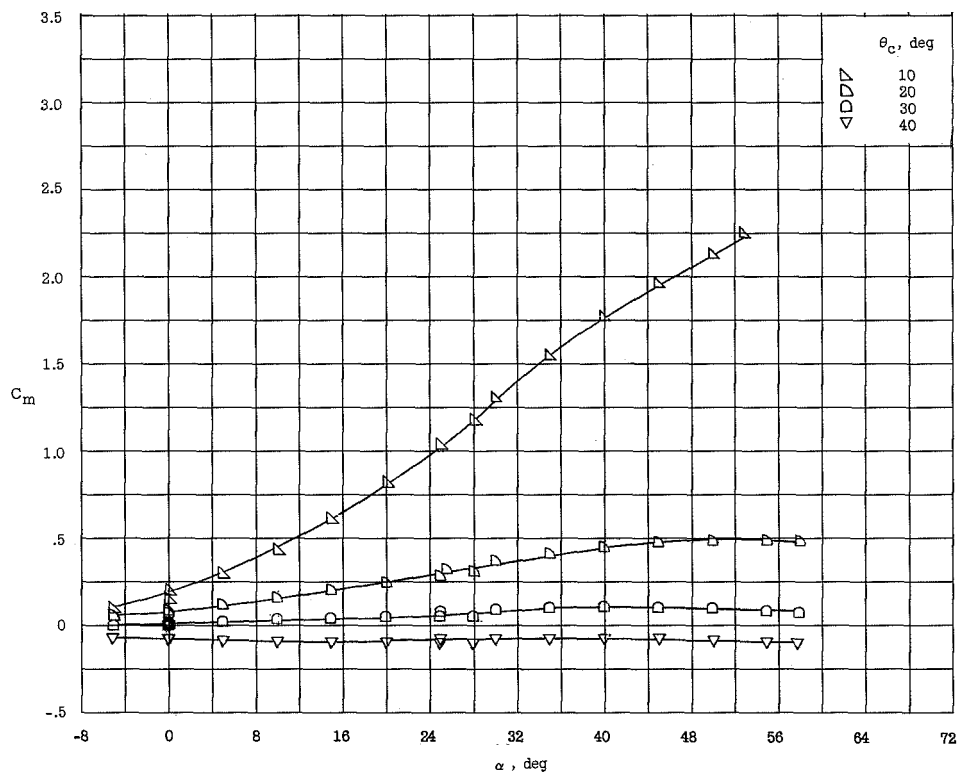
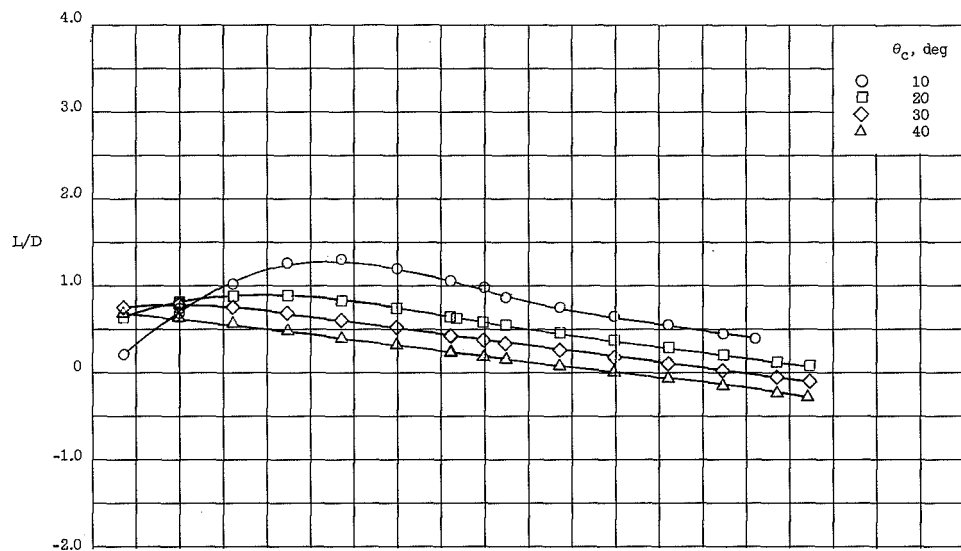
(a) C_L and C_D .

Figure 6.- Longitudinal characteristics of the round-bottom half-cone series. $h/R = 0.4$.



(b) L/D and C_m about the body base.

Figure 6.- Concluded.

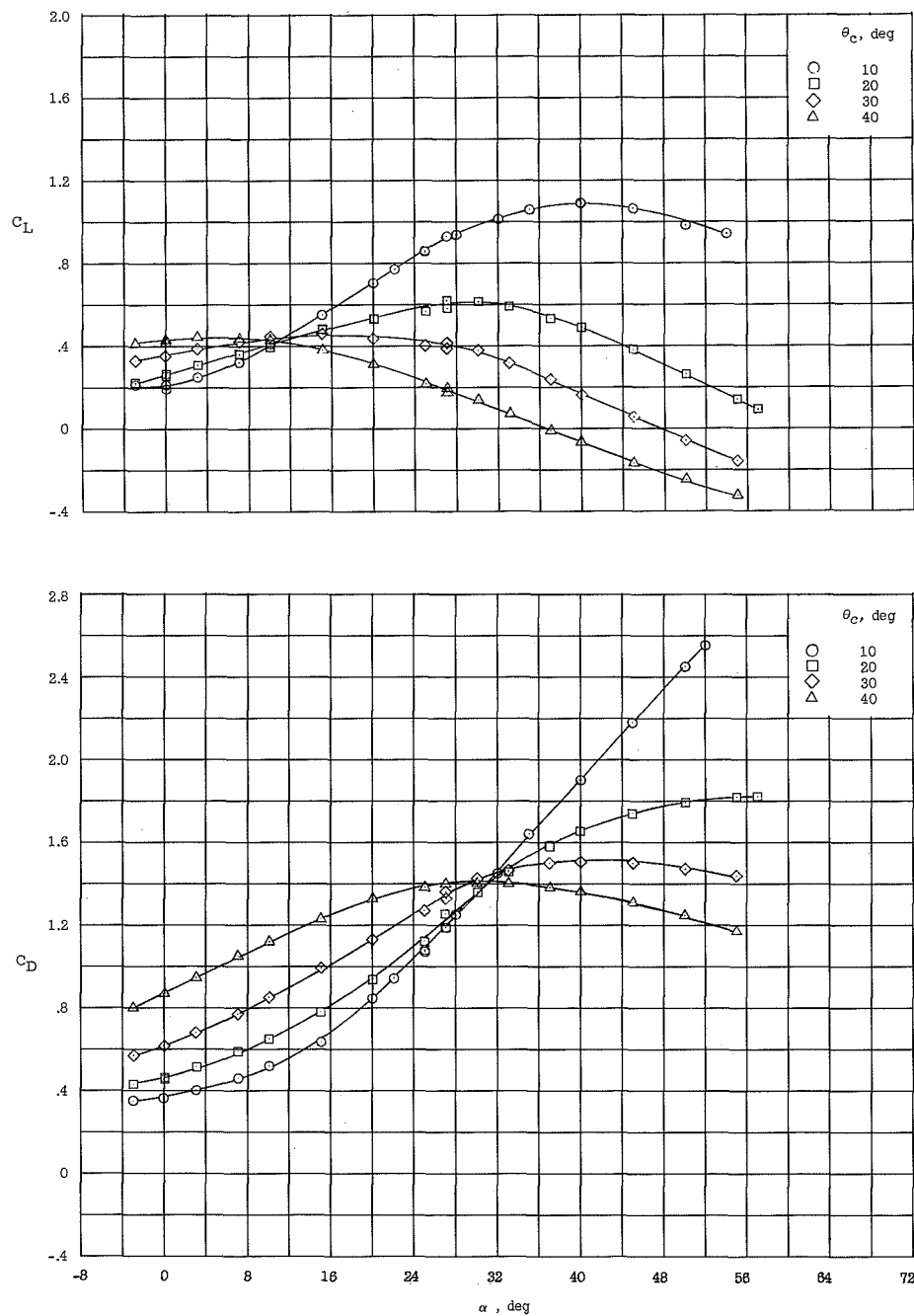
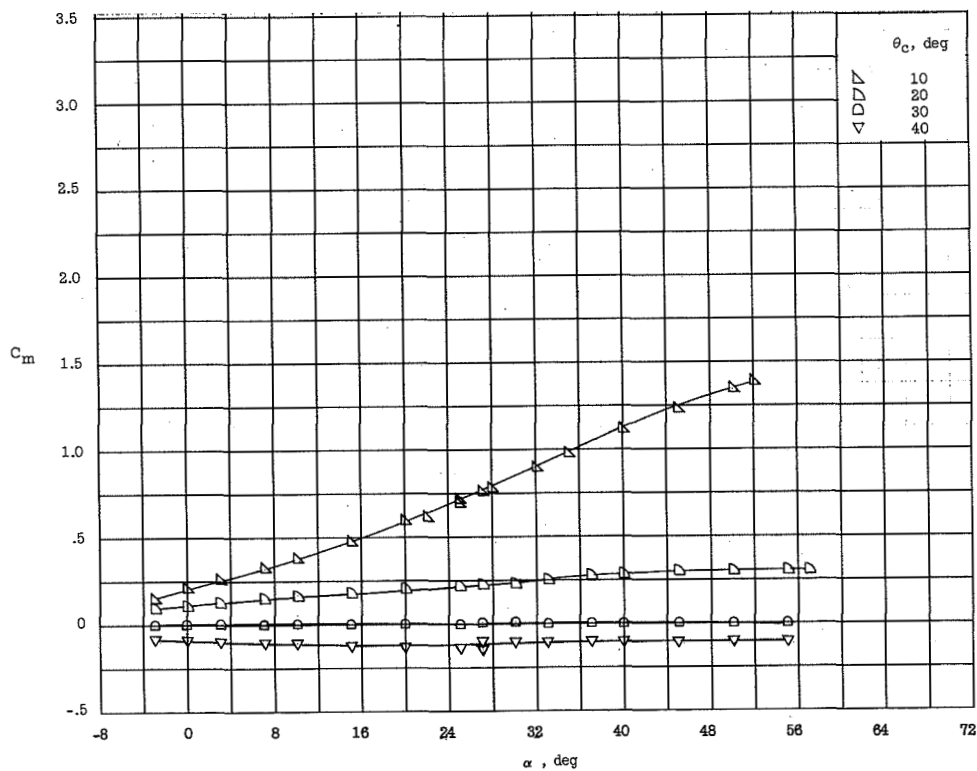
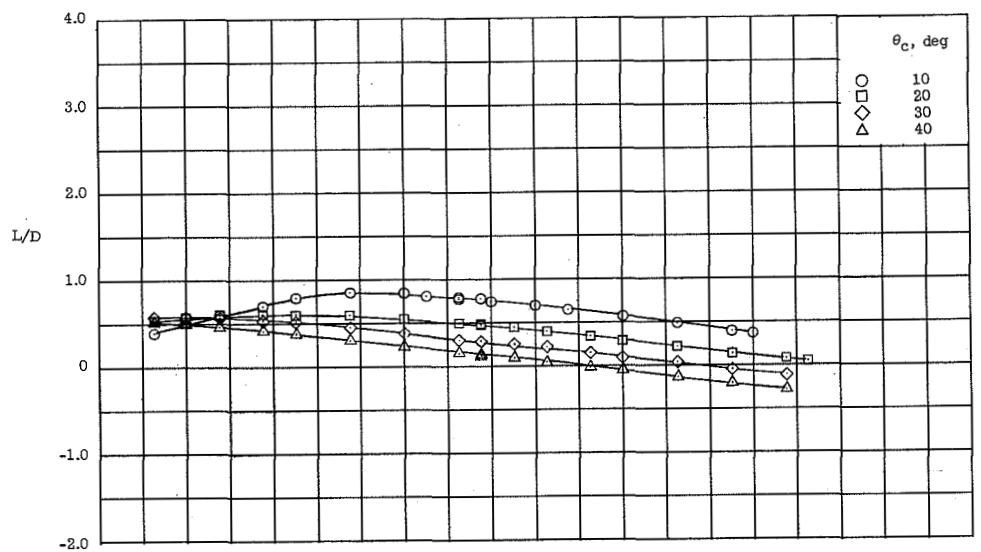
(a) C_L and C_D .

Figure 7.- Longitudinal characteristics of the round-bottom half-cone series. $h/R = 0.6$.



(b) L/D and C_m about the body base.

Figure 7.- Concluded.

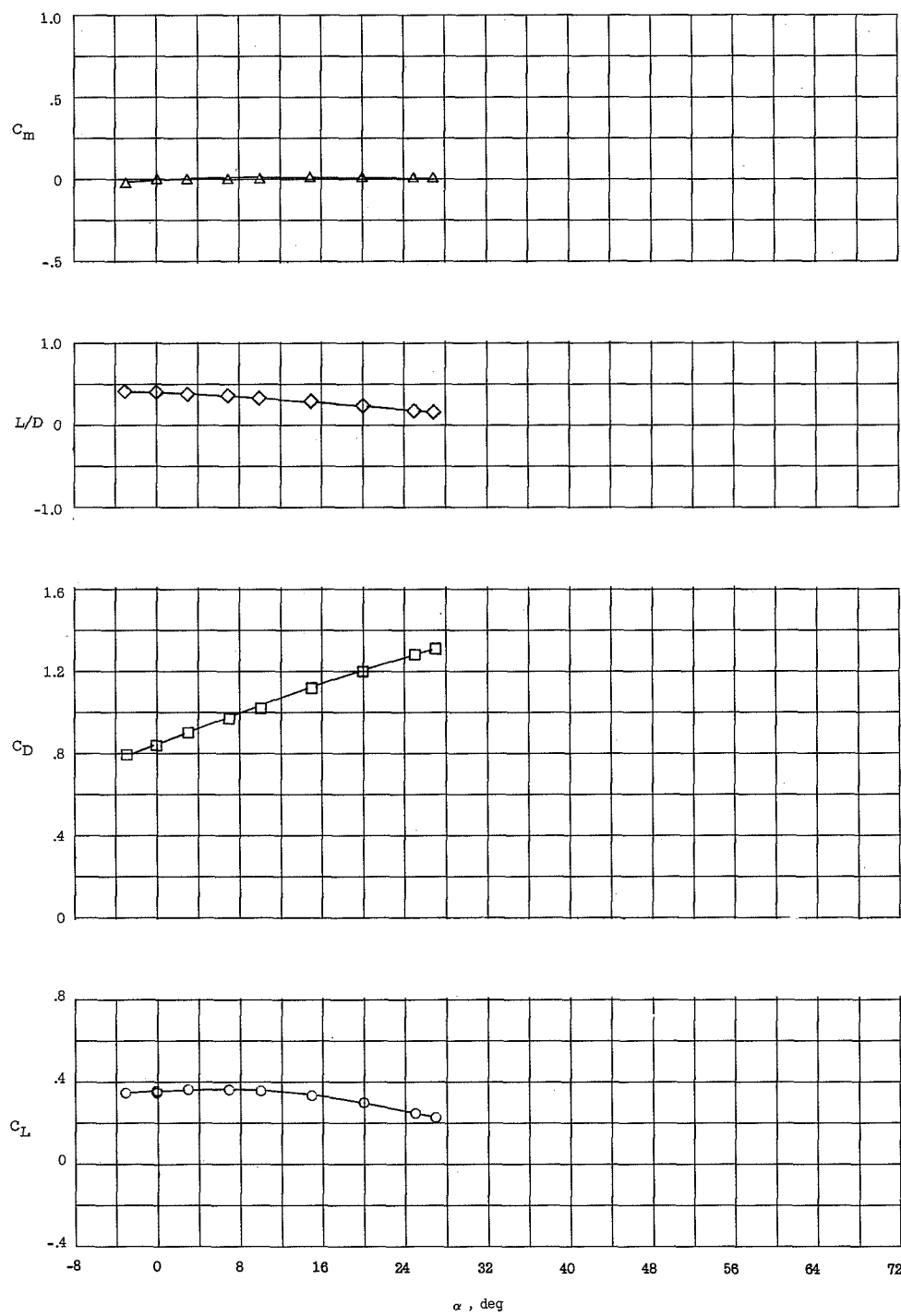


Figure 8.- Longitudinal characteristics of a round-bottom quarter sphere.

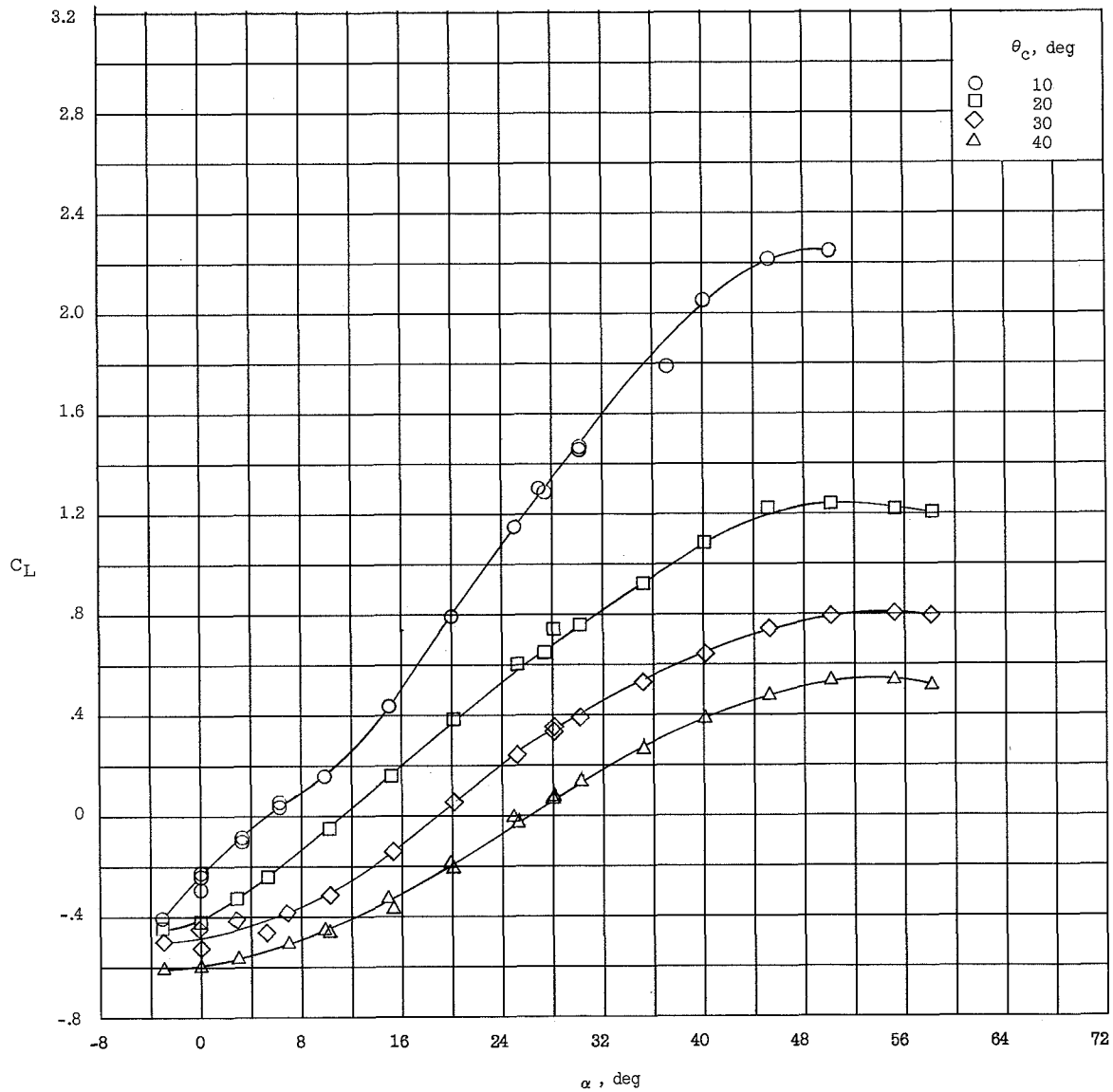
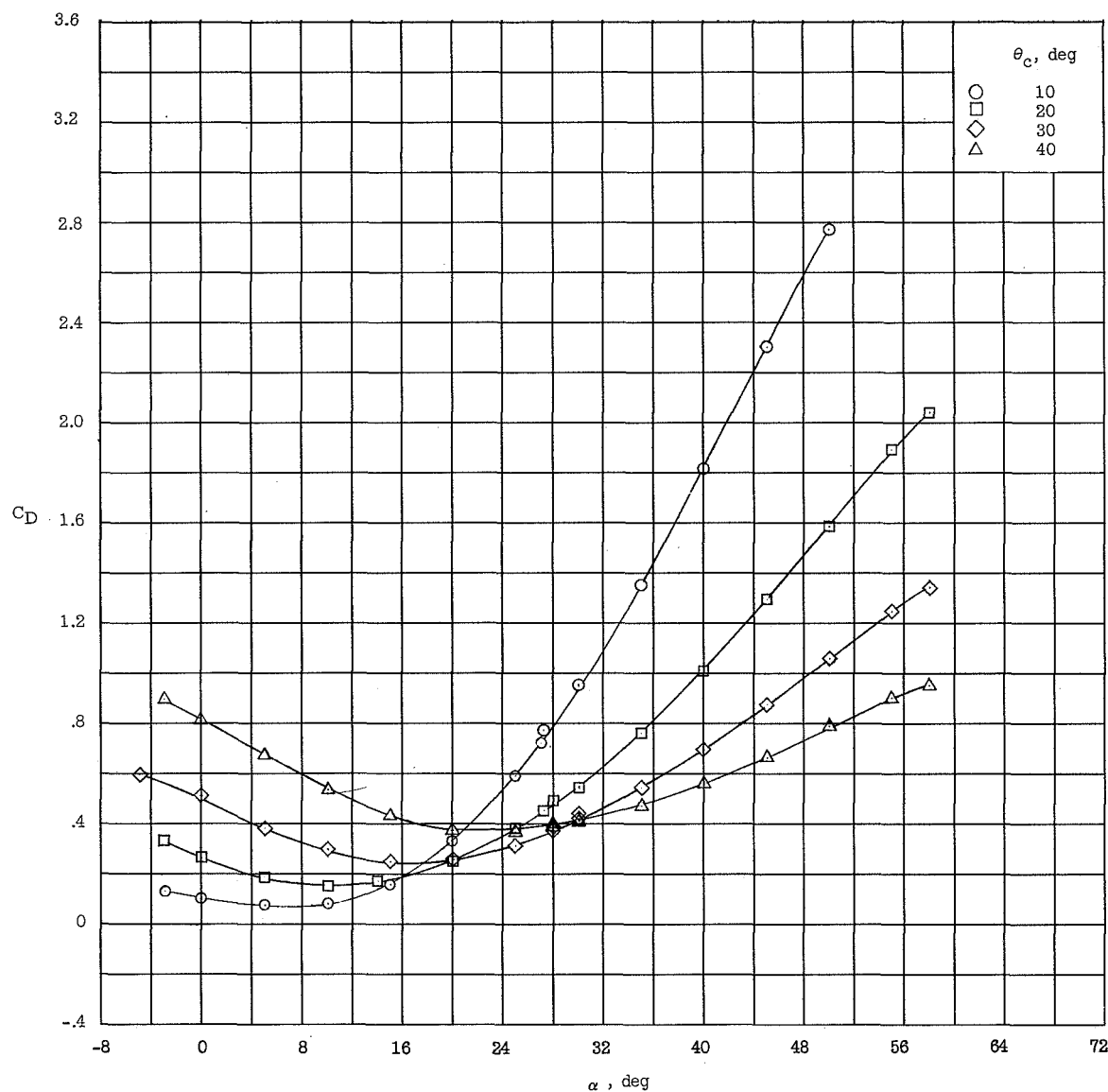
(a) C_L .

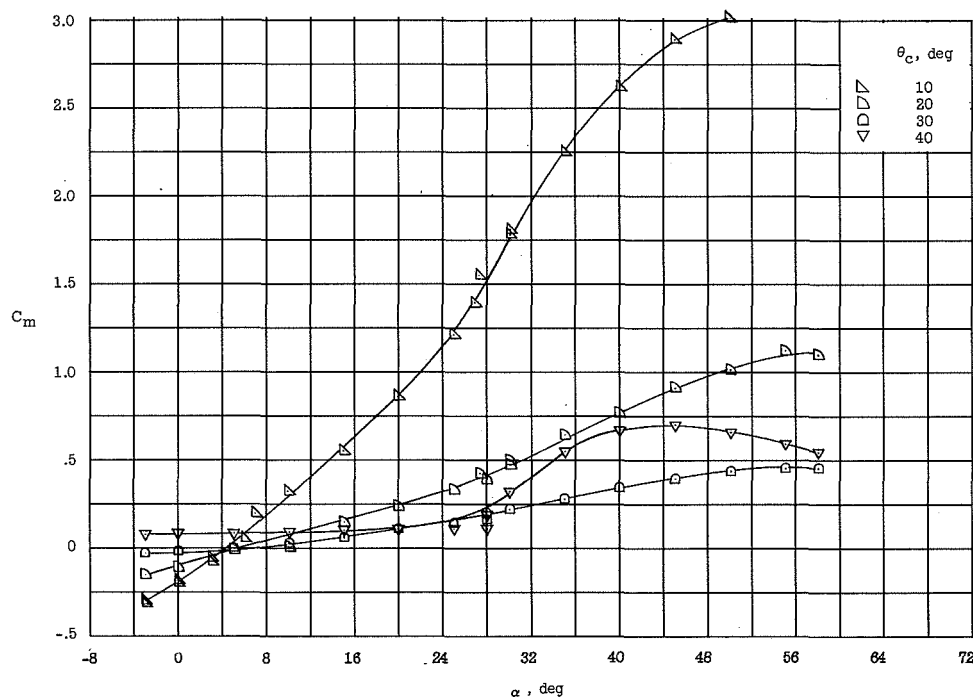
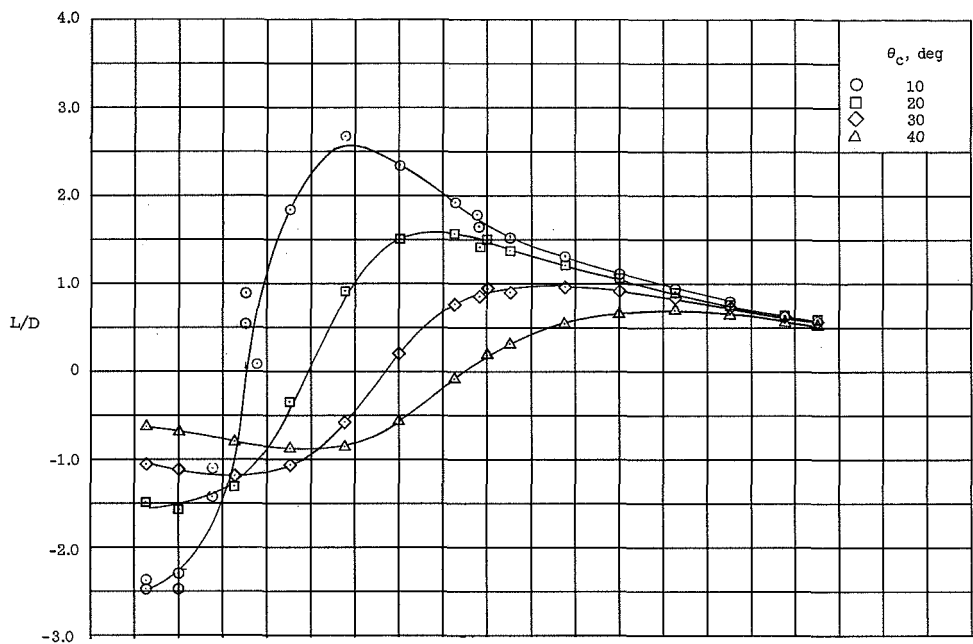
Figure 9.- Longitudinal characteristics of the spherically blunted flat-bottom half-cone series. $h/R = 0$.

L-1437



(b) C_D .

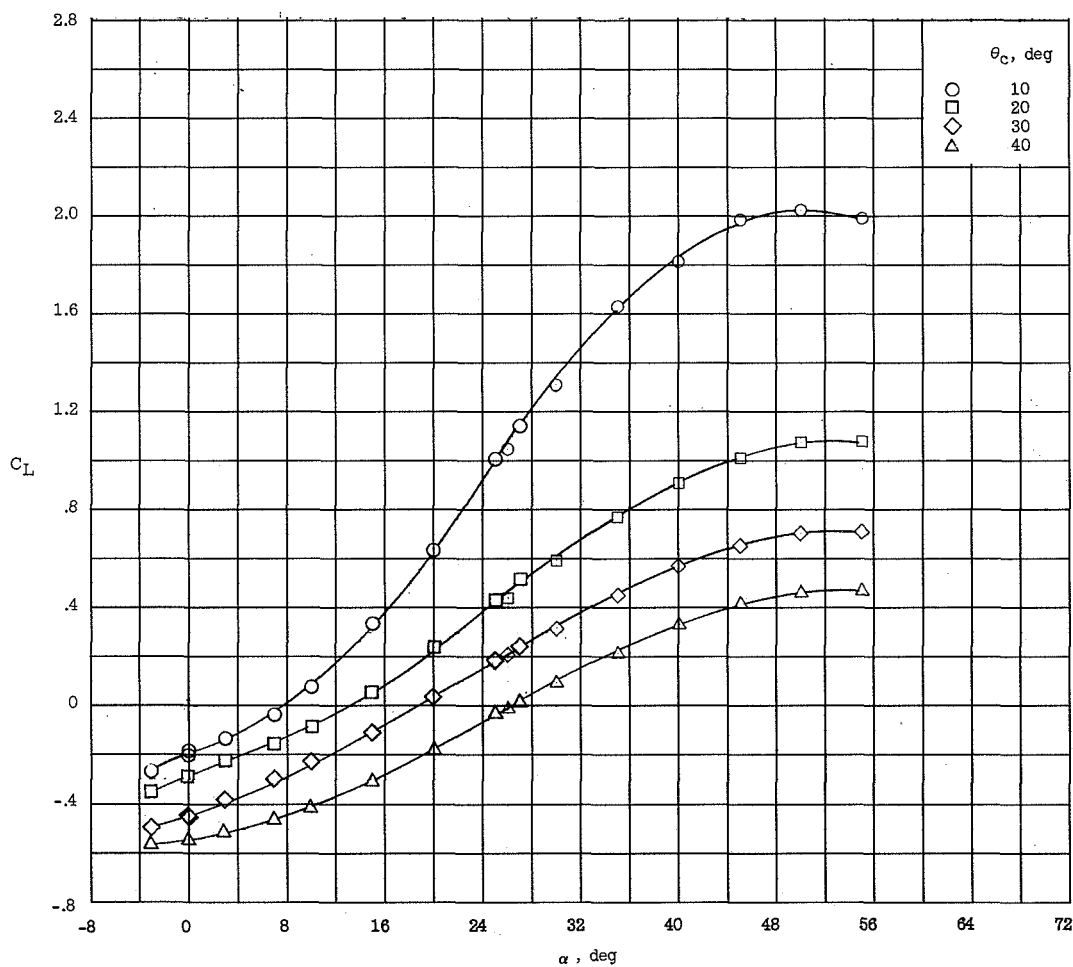
Figure 9.- Continued.



(c) L/D and C_m about the body base.

Figure 9.- Concluded.

L-1437



(a) C_L .

Figure 10.- Longitudinal characteristics of the spherically blunted flat-bottom half-cone series. $h/R = 0.4$.

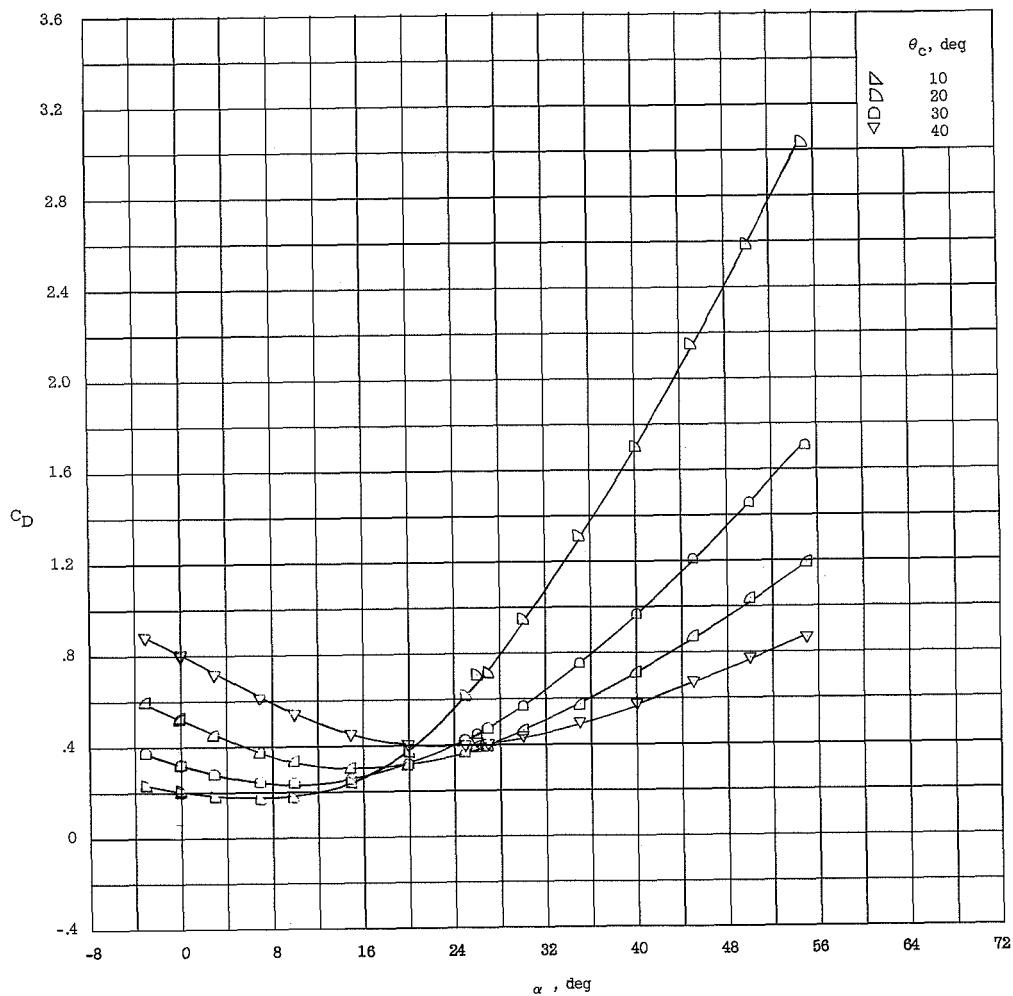
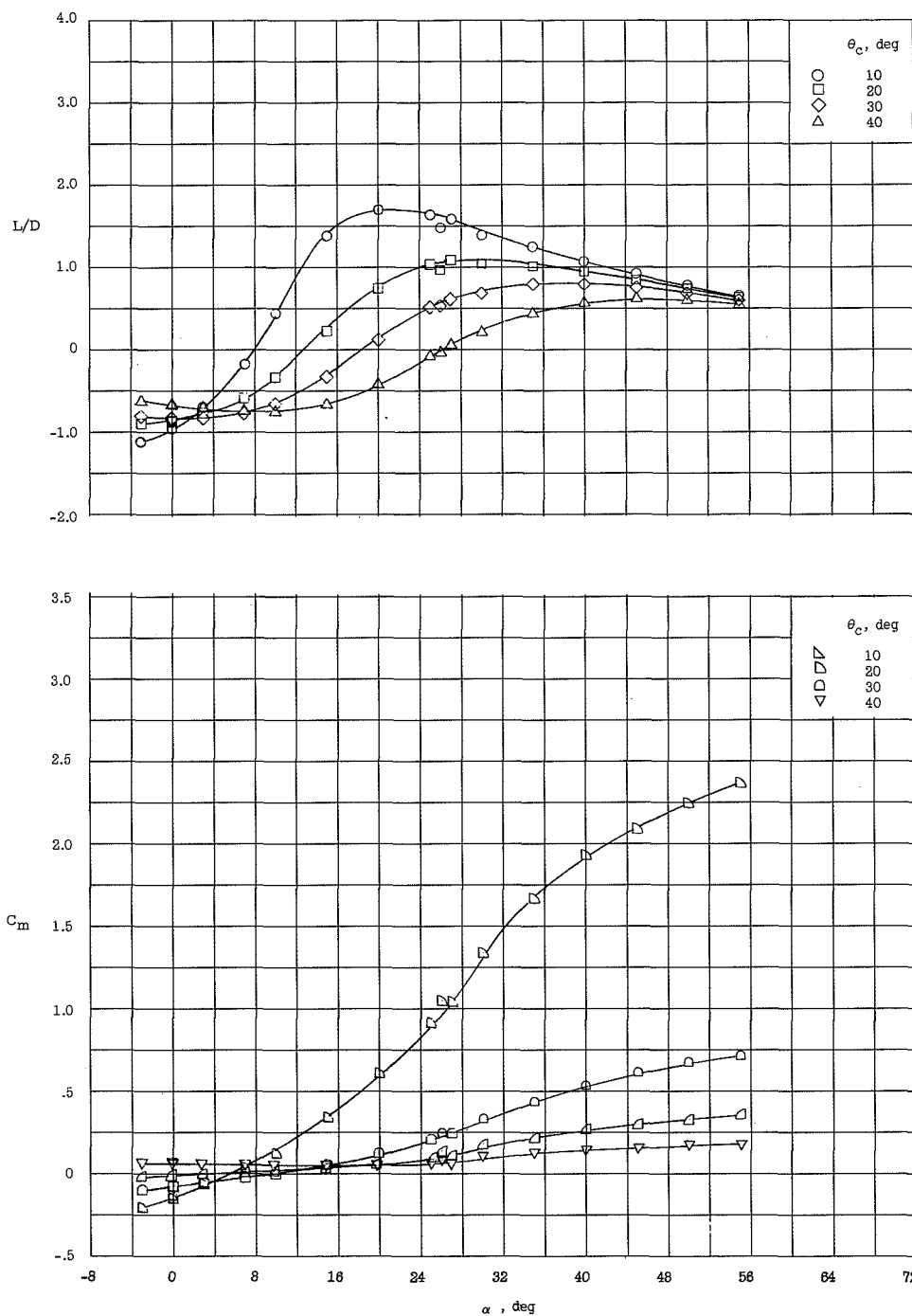
(b) C_D .

Figure 10.- Continued.

L=1437



(c) L/D and C_m about the body base.

Figure 10.- Concluded.

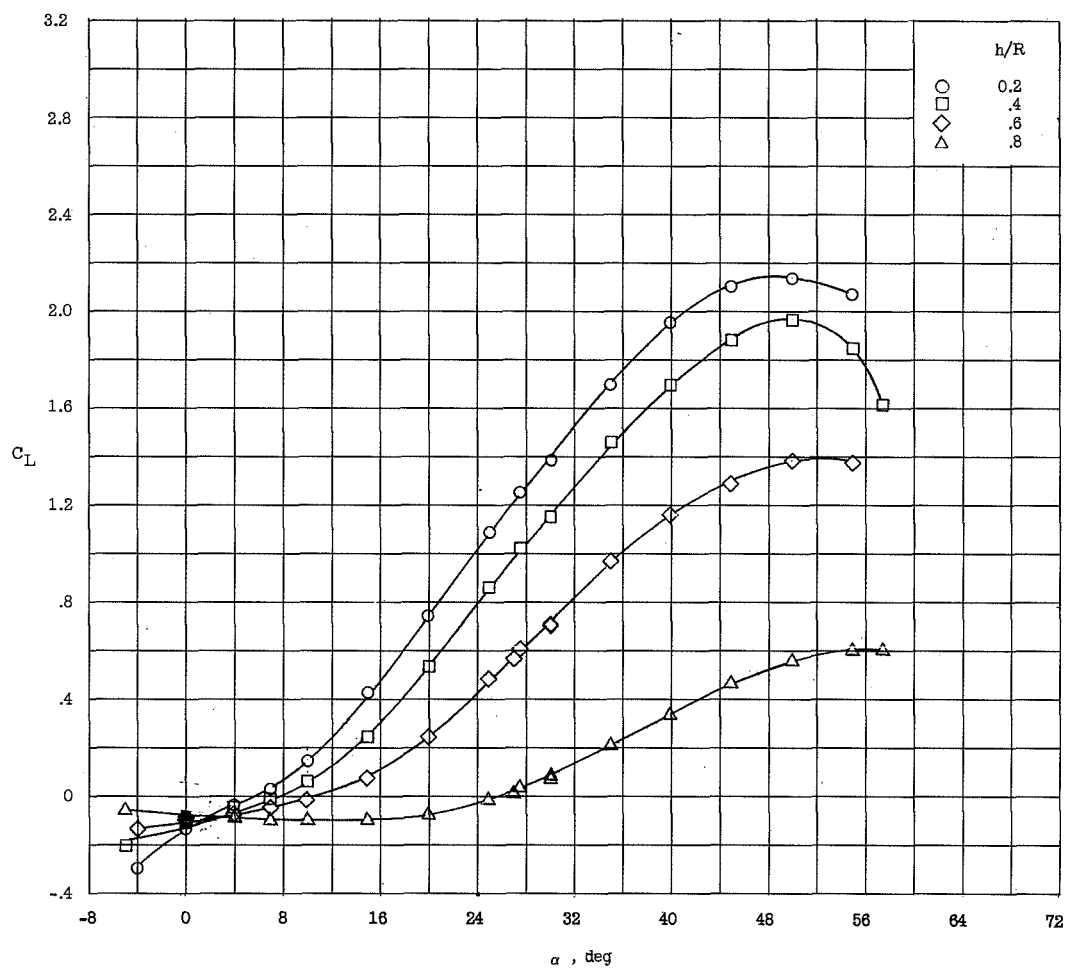
(a) C_L .

Figure 11.- Longitudinal characteristics of the flat-bottom half-cone series of varying nose bluntness and cant. $\delta_N = 90^\circ$.

I-1437

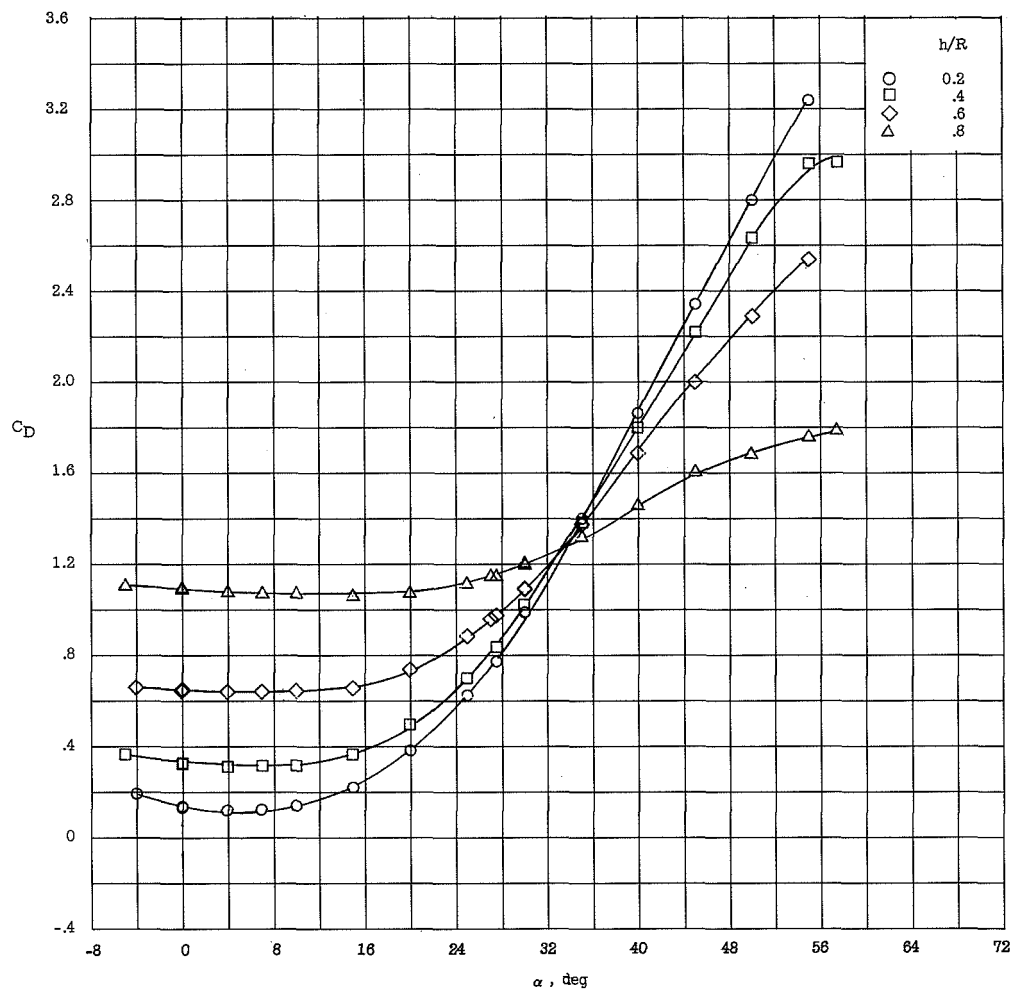
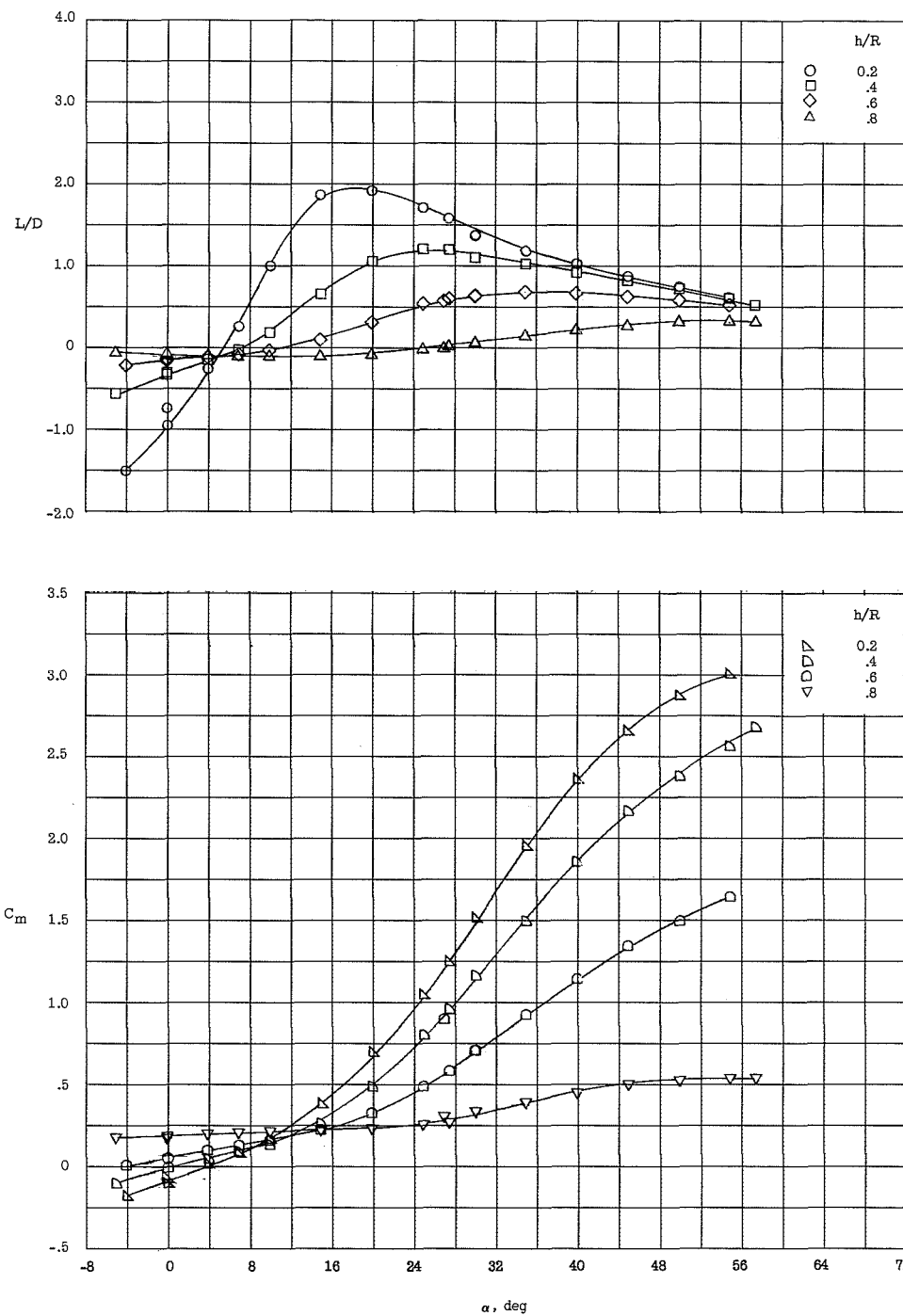
(b) C_D .

Figure 11.- Continued.



(c) L/D and C_m about the body base.

Figure 11.- Concluded.

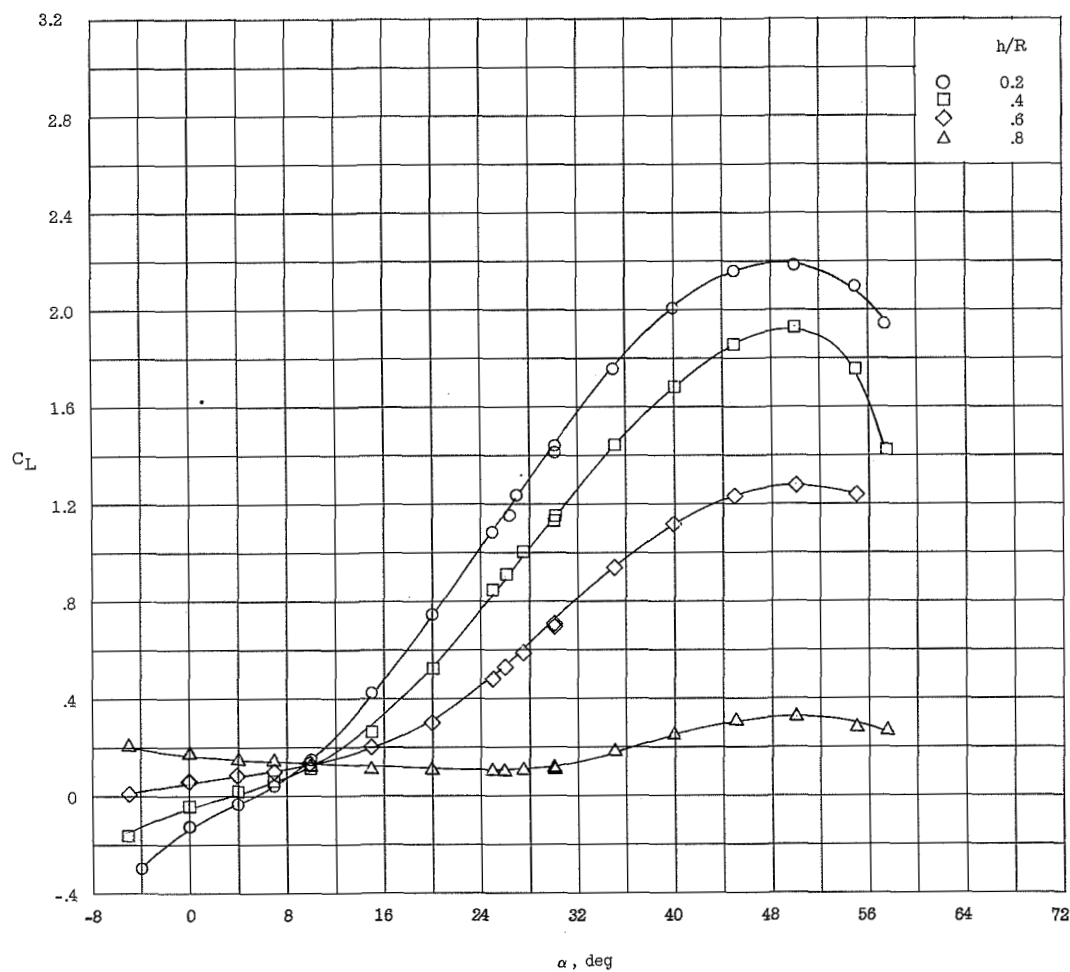
(a) C_L .

Figure 12.- Longitudinal characteristics of the flat-bottom half-cone series of varying bluntness and cant. $\delta_N = 75^\circ$.

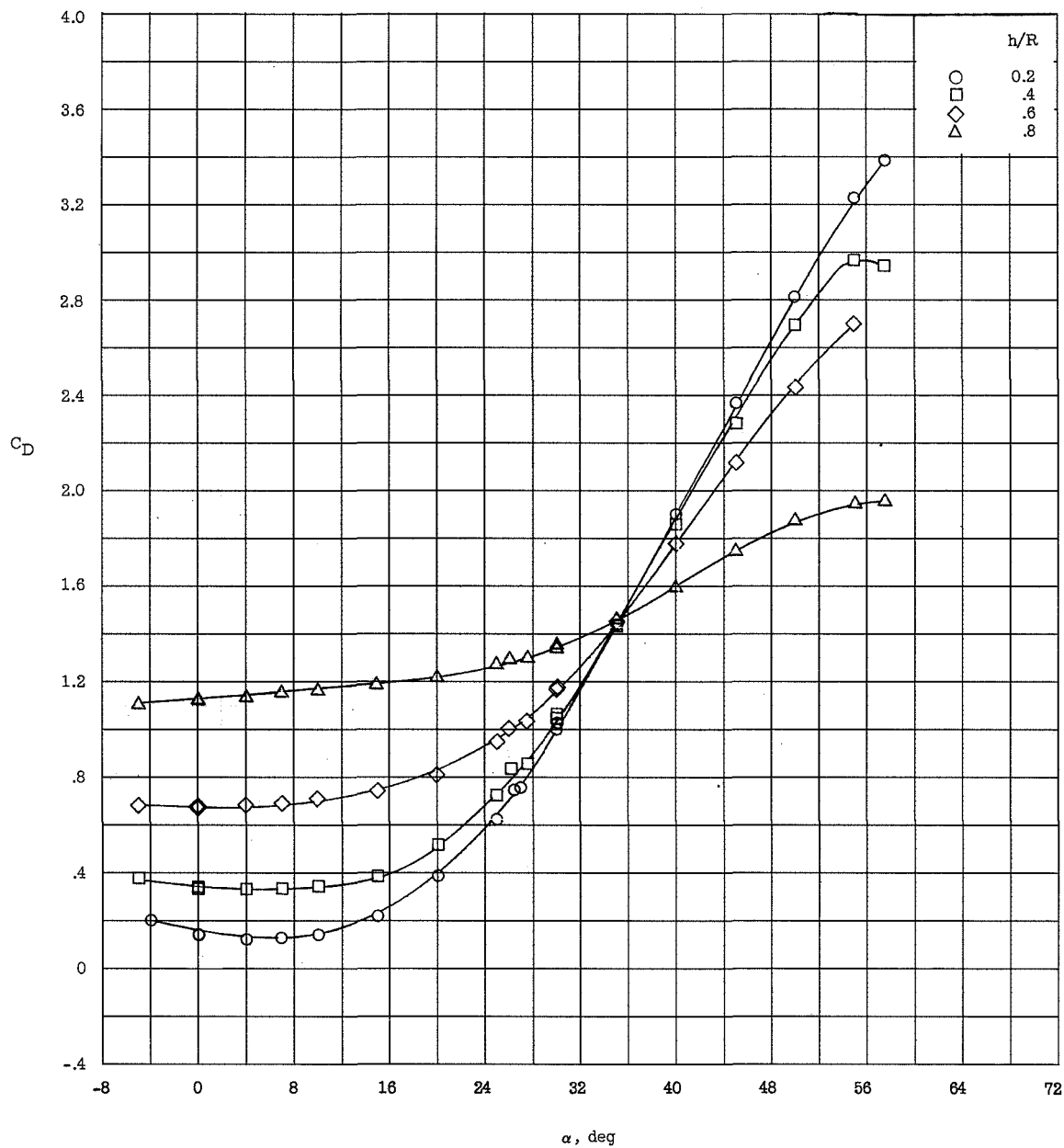
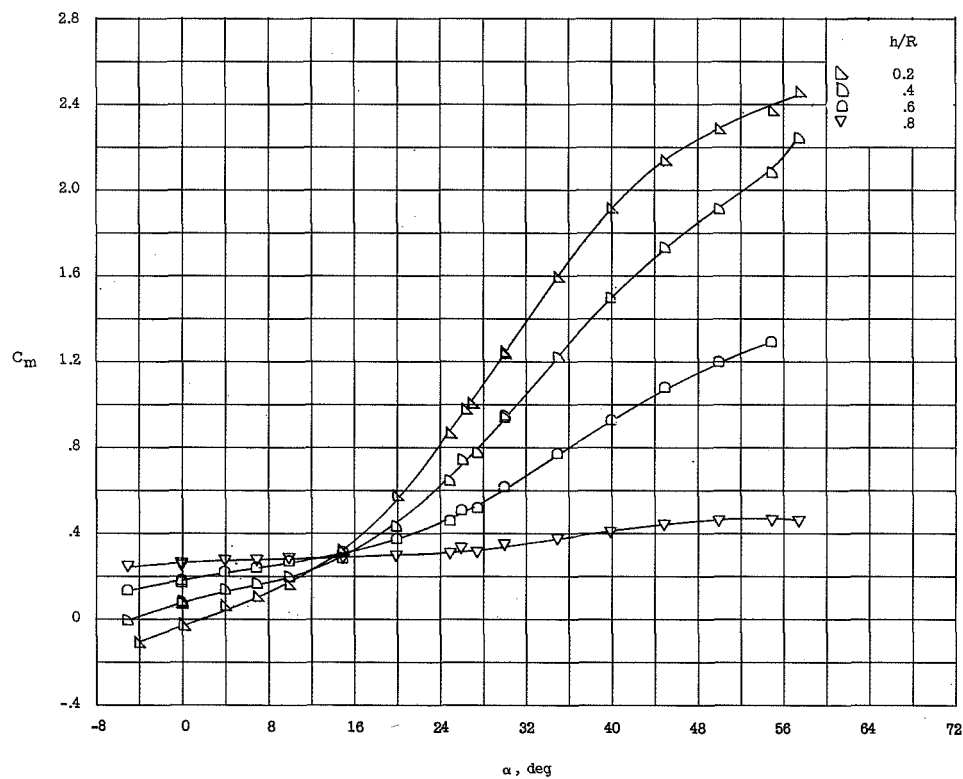
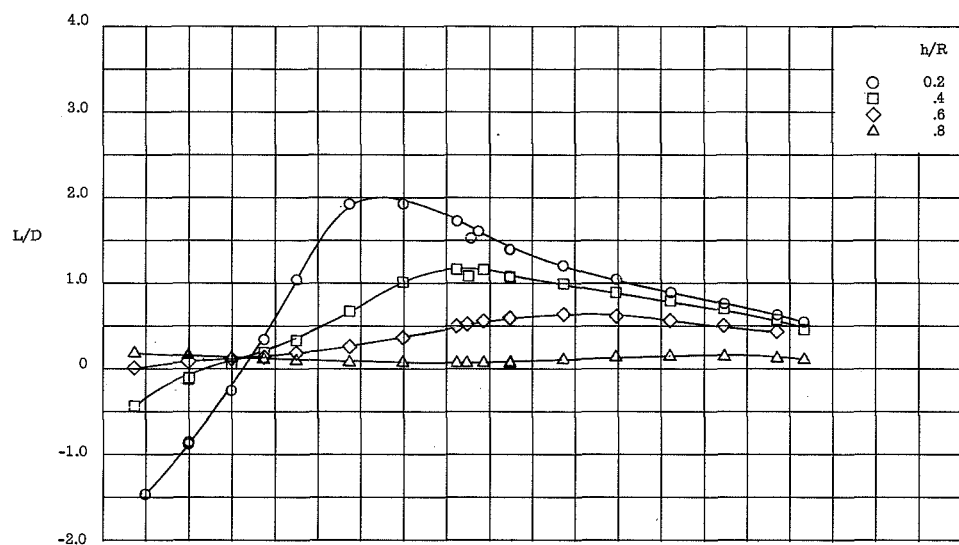
(b) C_D .

Figure 12.- Continued.



(c) L/D and C_m about the body base.

Figure 12.- Concluded.

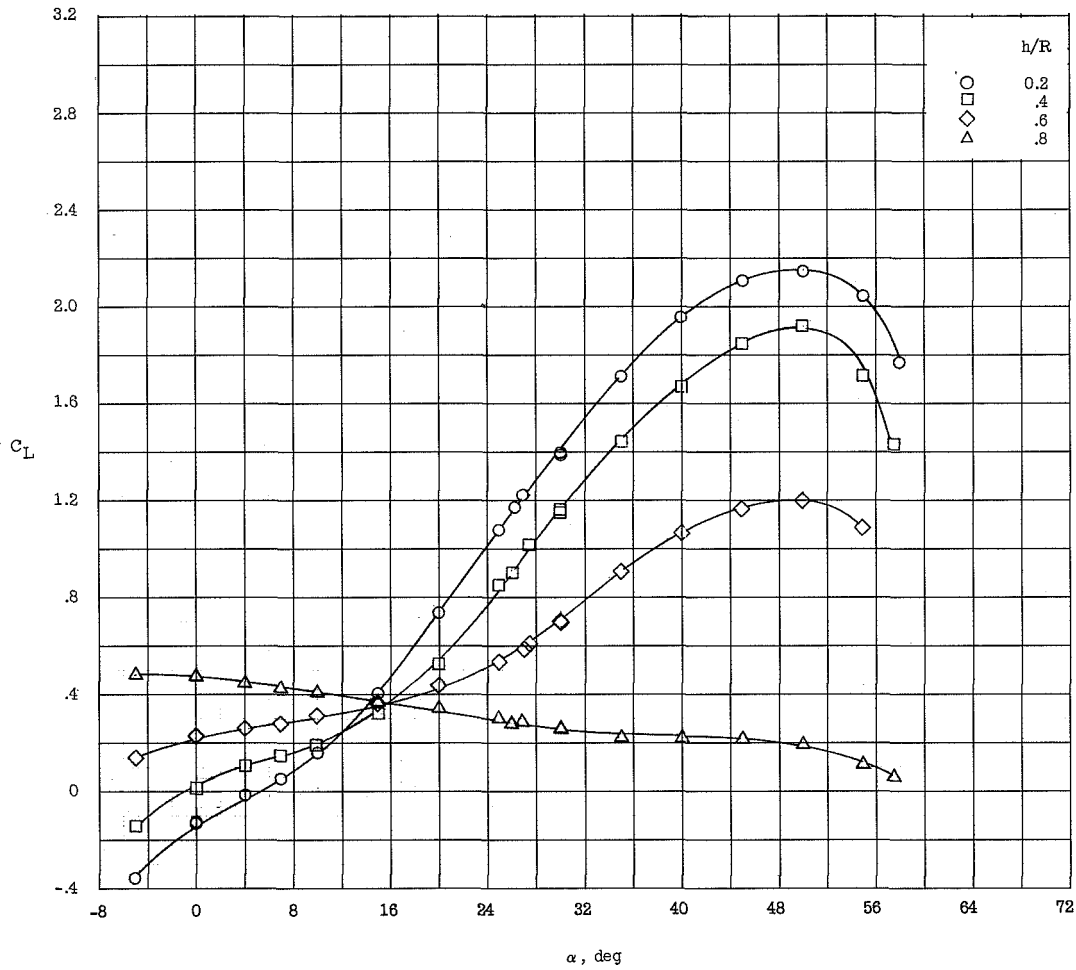
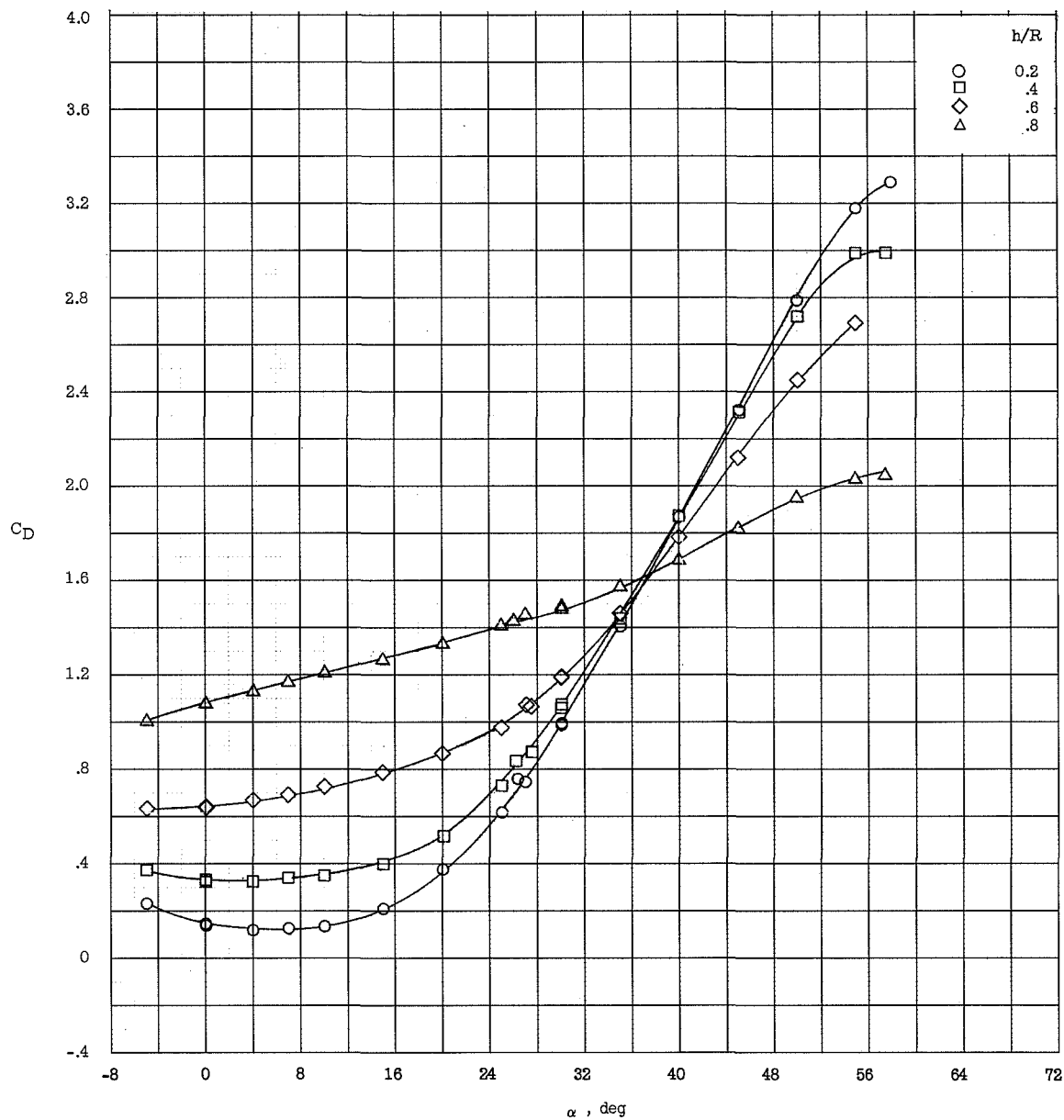
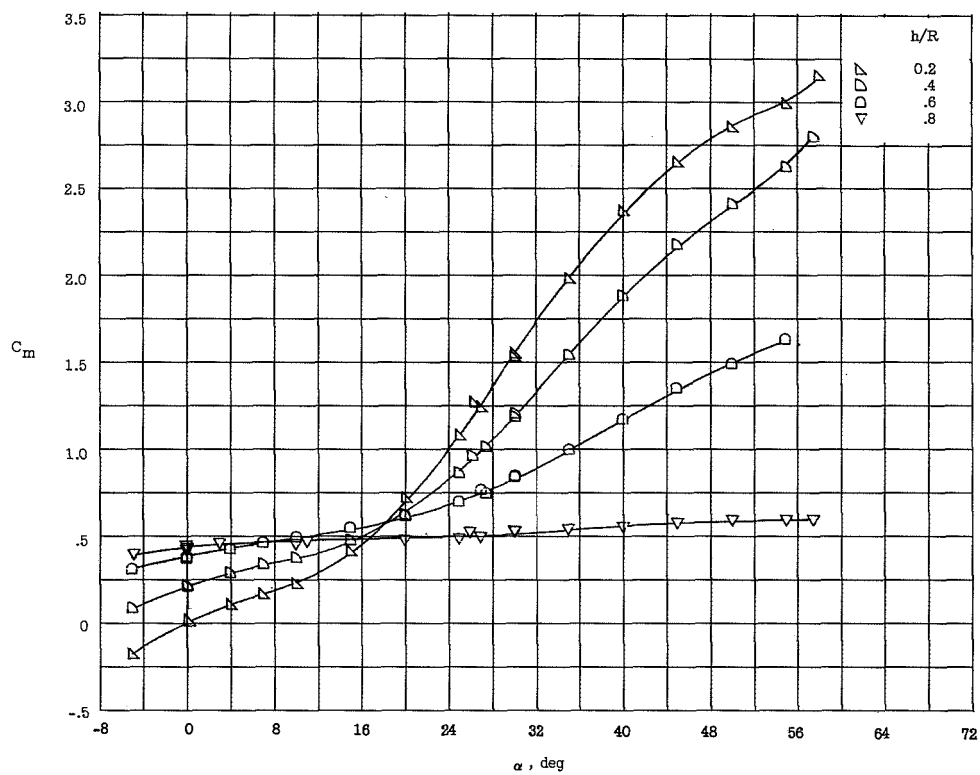
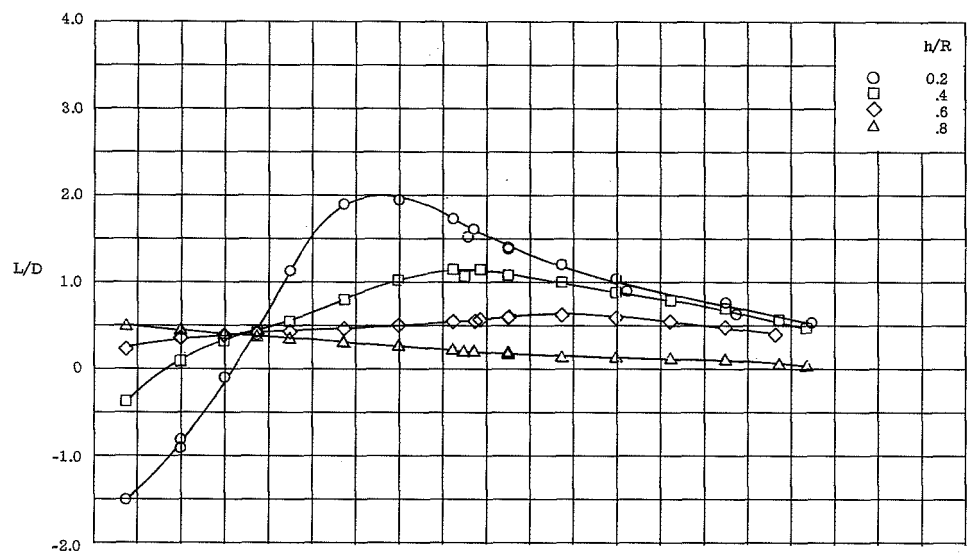
(a) C_L .

Figure 13.- Longitudinal characteristics of the flat-bottom half-cone series of varying bluntness and cant. $\delta_N = 60^\circ$.



(b) C_D .

Figure 13.- Continued.



(c) L/D and C_m about the body base.

Figure 13.- Concluded.

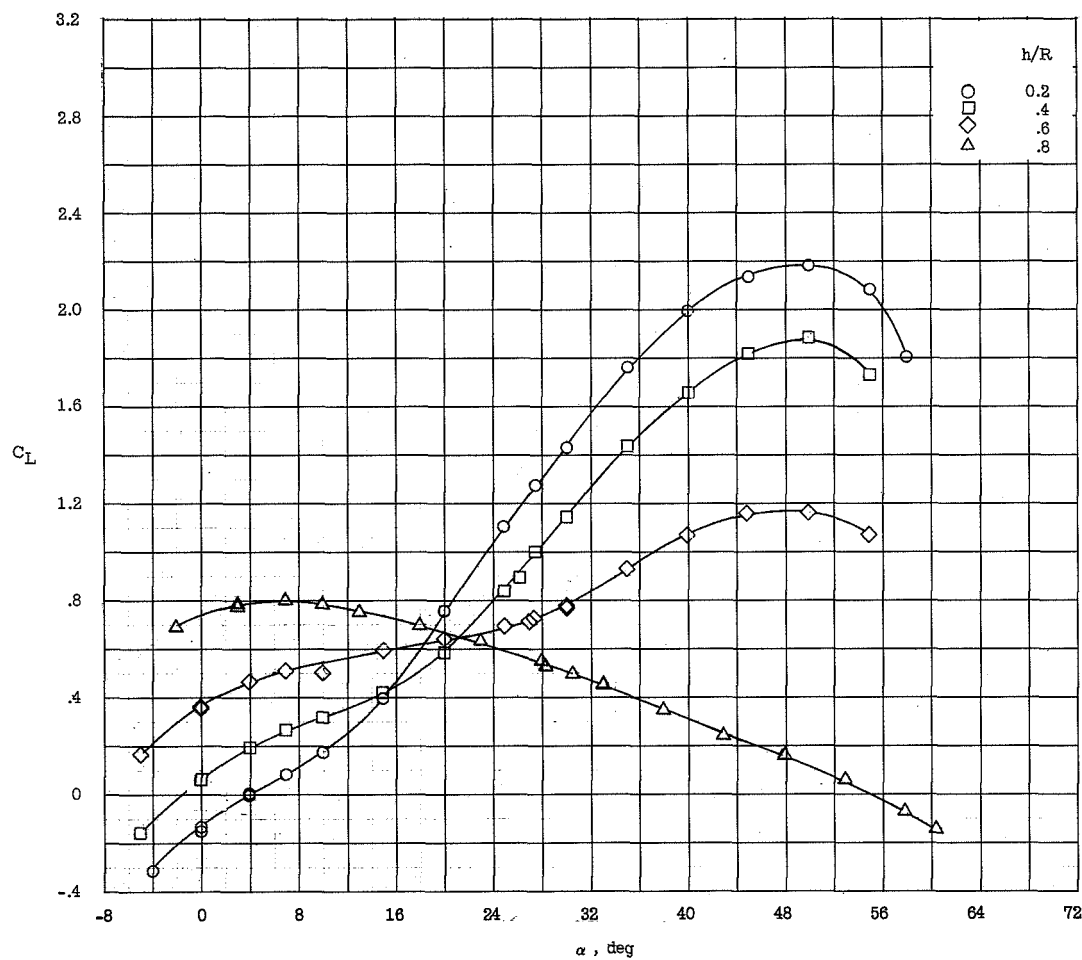
(a) C_L .

Figure 14.- Longitudinal characteristics of the flat-bottom half-cone series of varying bluntness and cant. $\delta_N = 45^\circ$.

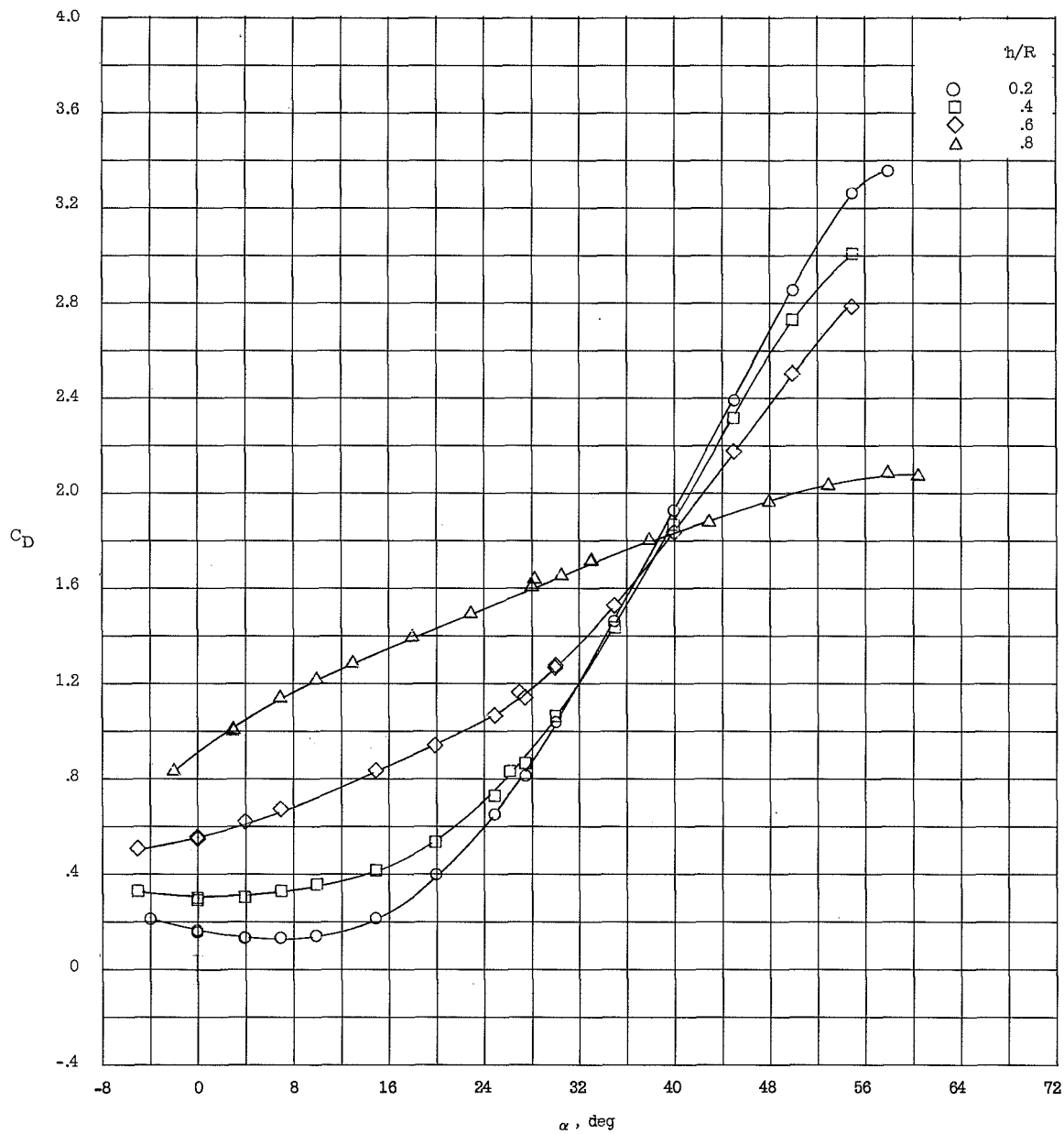
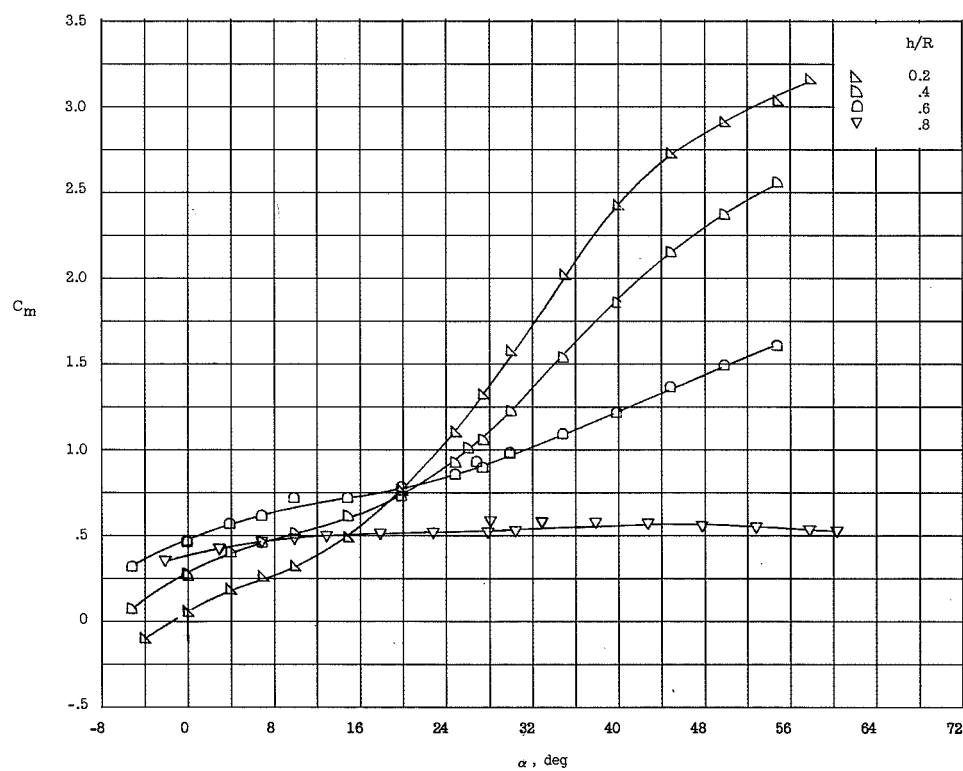
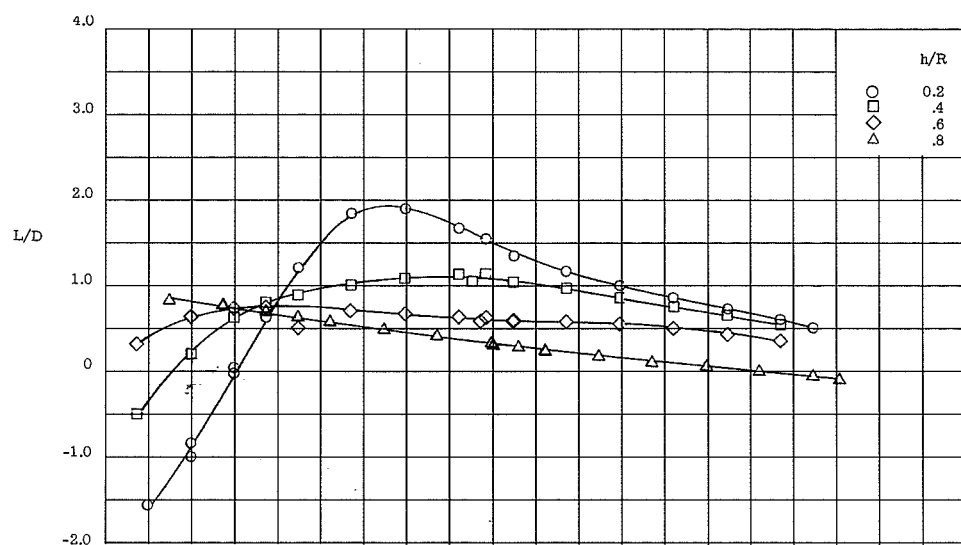
(b) C_D .

Figure 14.- Continued.



(c) L/D and C_m about the body base.

Figure 14.- Concluded.

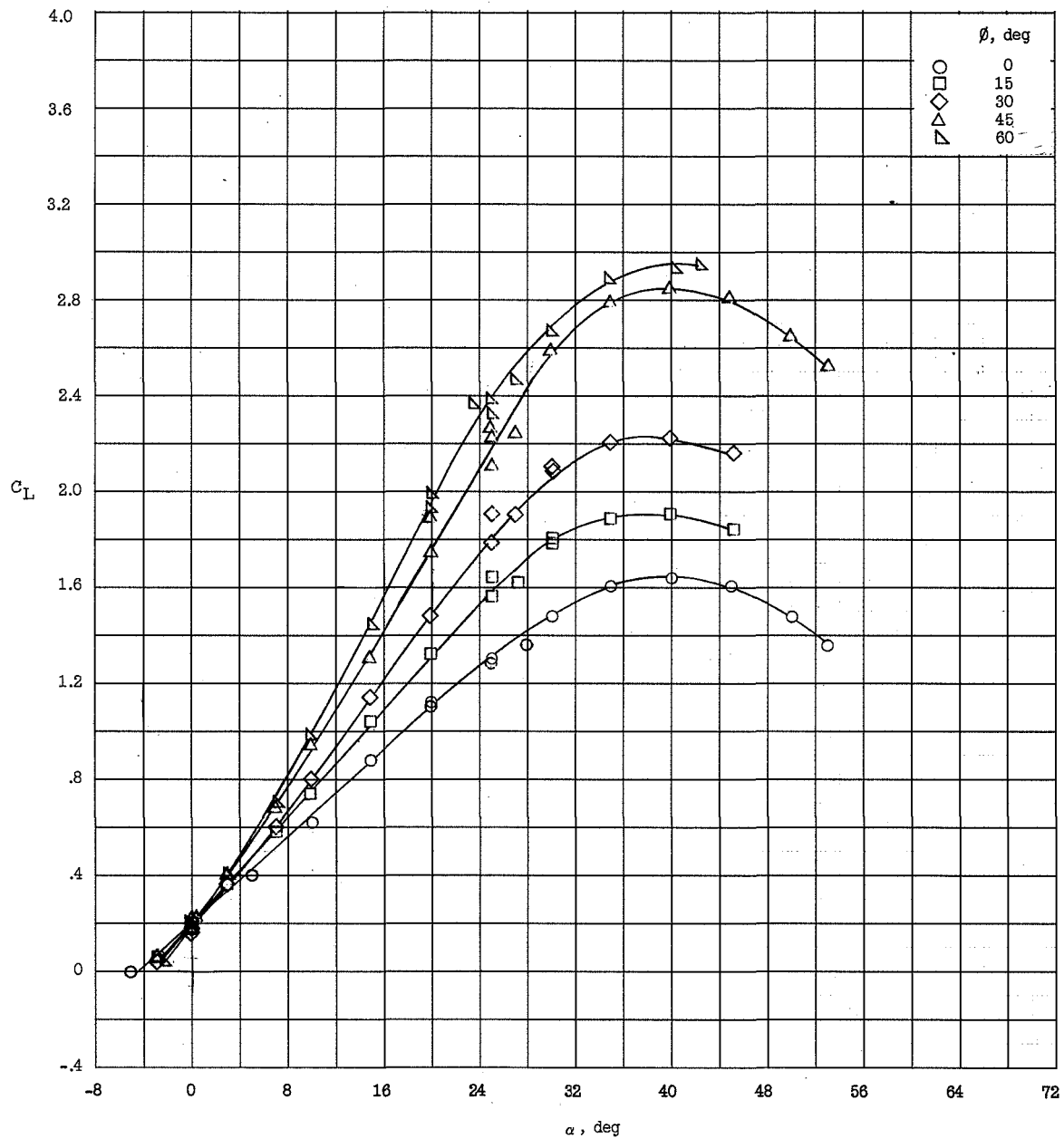
(a) C_L .

Figure 15.- Longitudinal characteristics of the conic-sectored series.
 $\theta_c = 10^\circ$; $h/R = 0$.

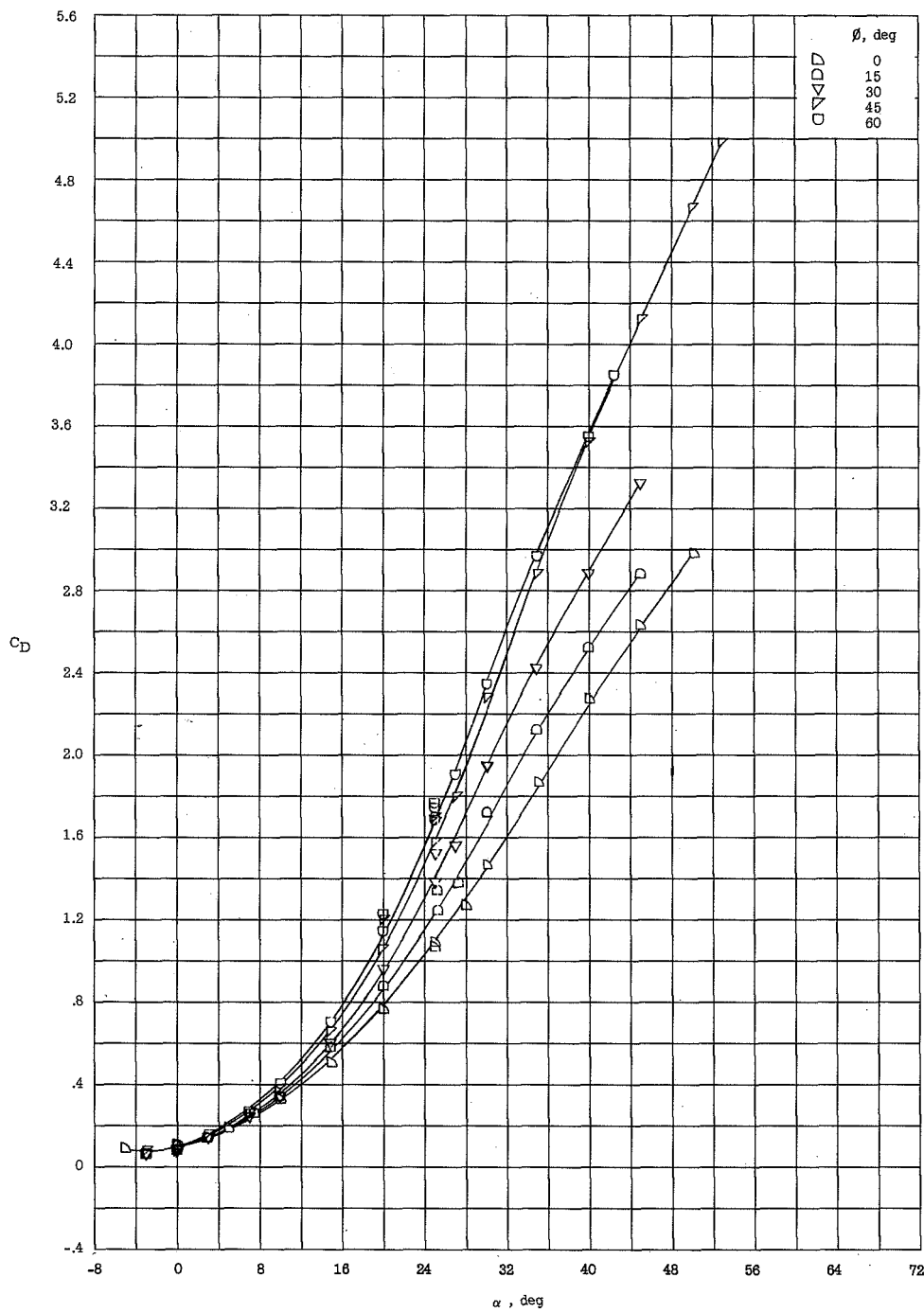
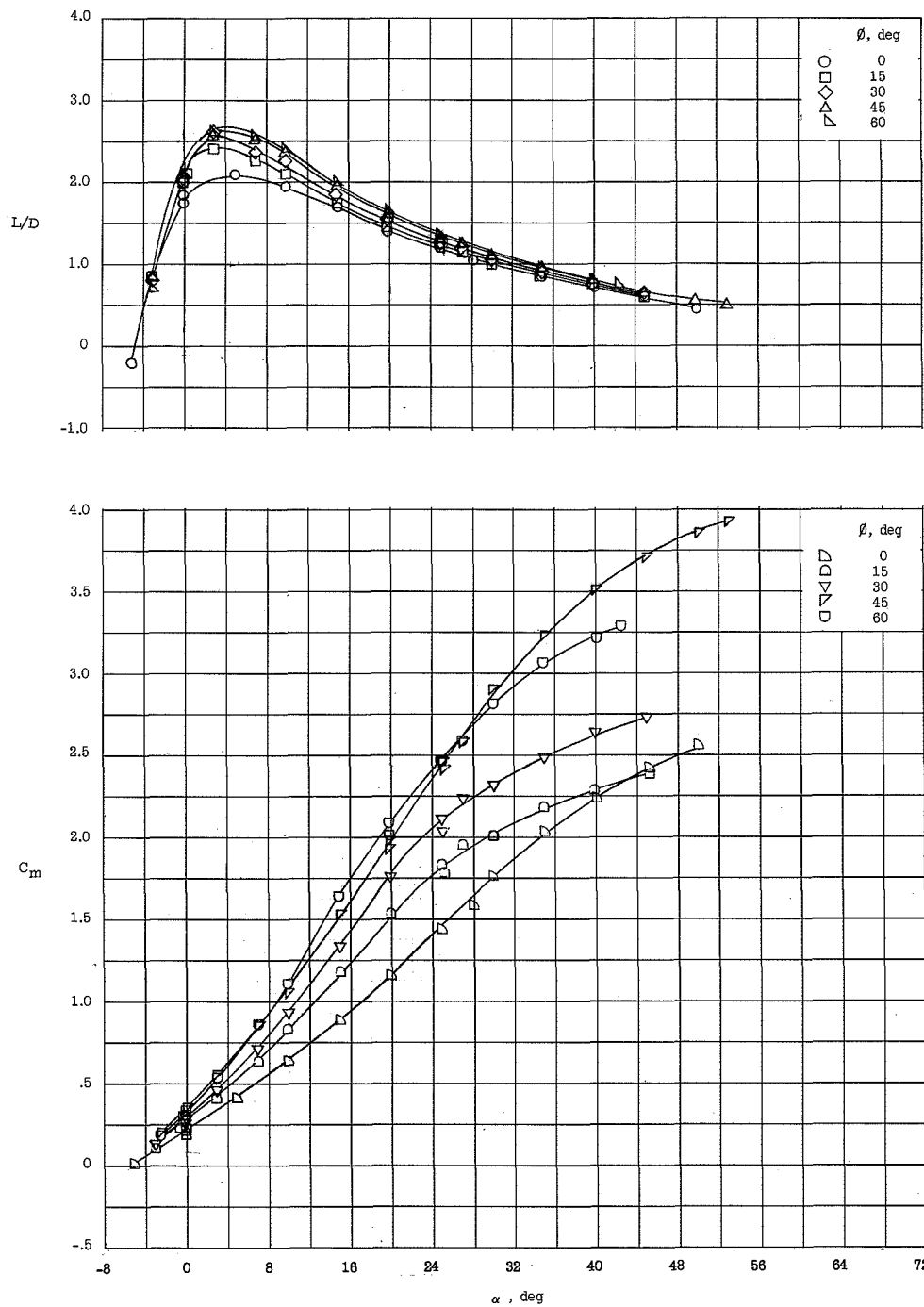
(b) C_D .

Figure 15.- Continued.



(c) L/D and C_m about the body base.

Figure 15.- Concluded.

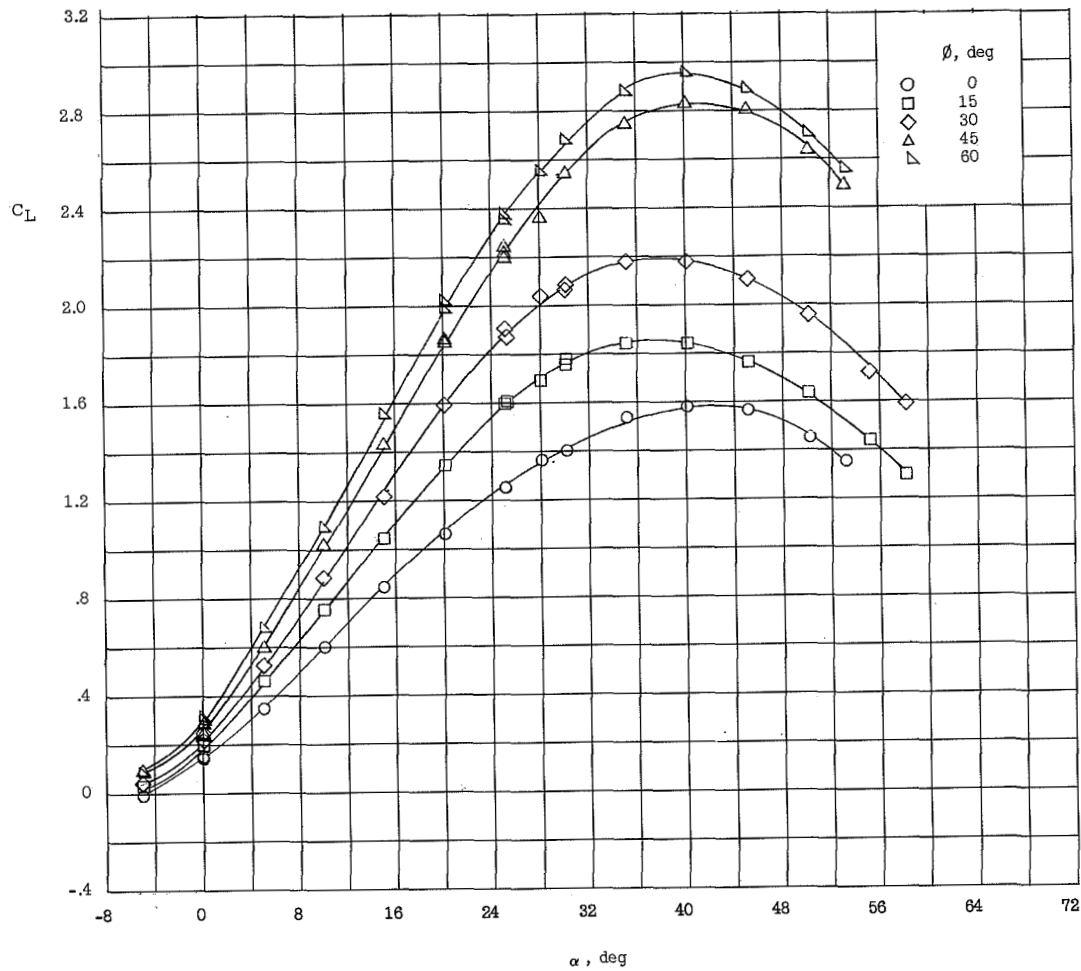
(a) C_L .

Figure 16.- Longitudinal characteristics of the conic-sectored series.
 $\theta_c = 10^\circ$; $h/R = 0.2$.

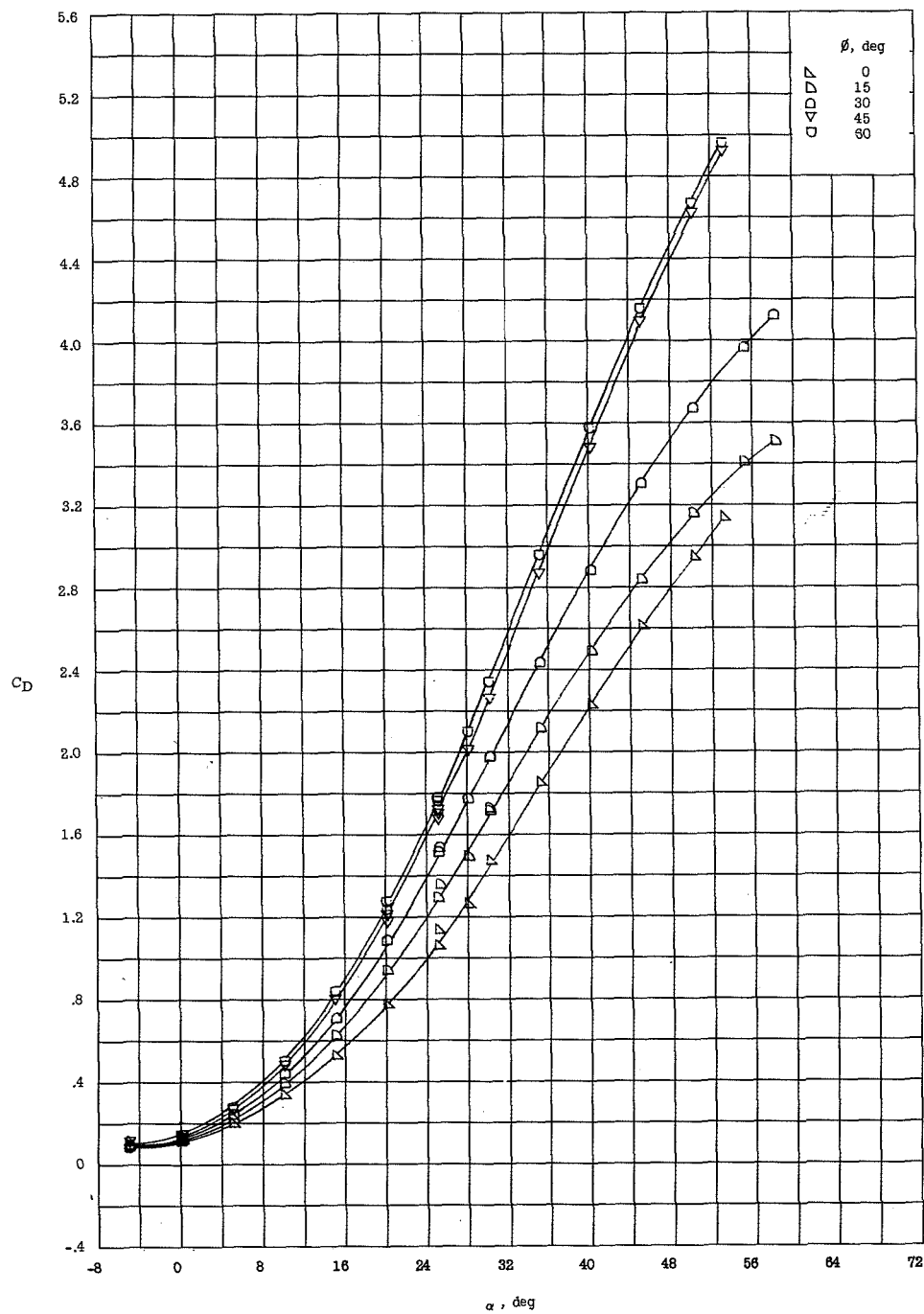
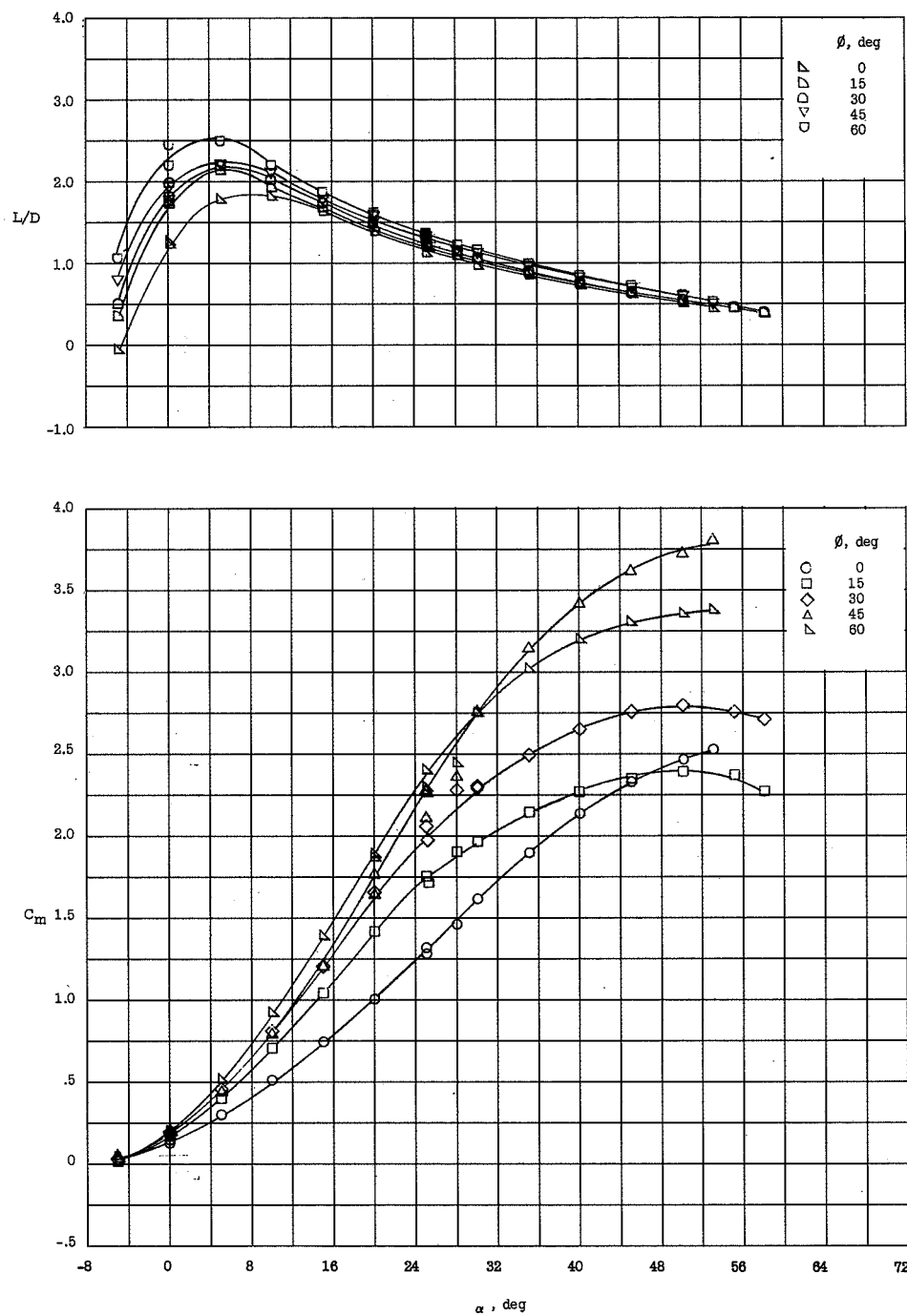
(b) C_D .

Figure 16.- Continued.



(c) L/D and C_m about the body base.

Figure 16.- Concluded.

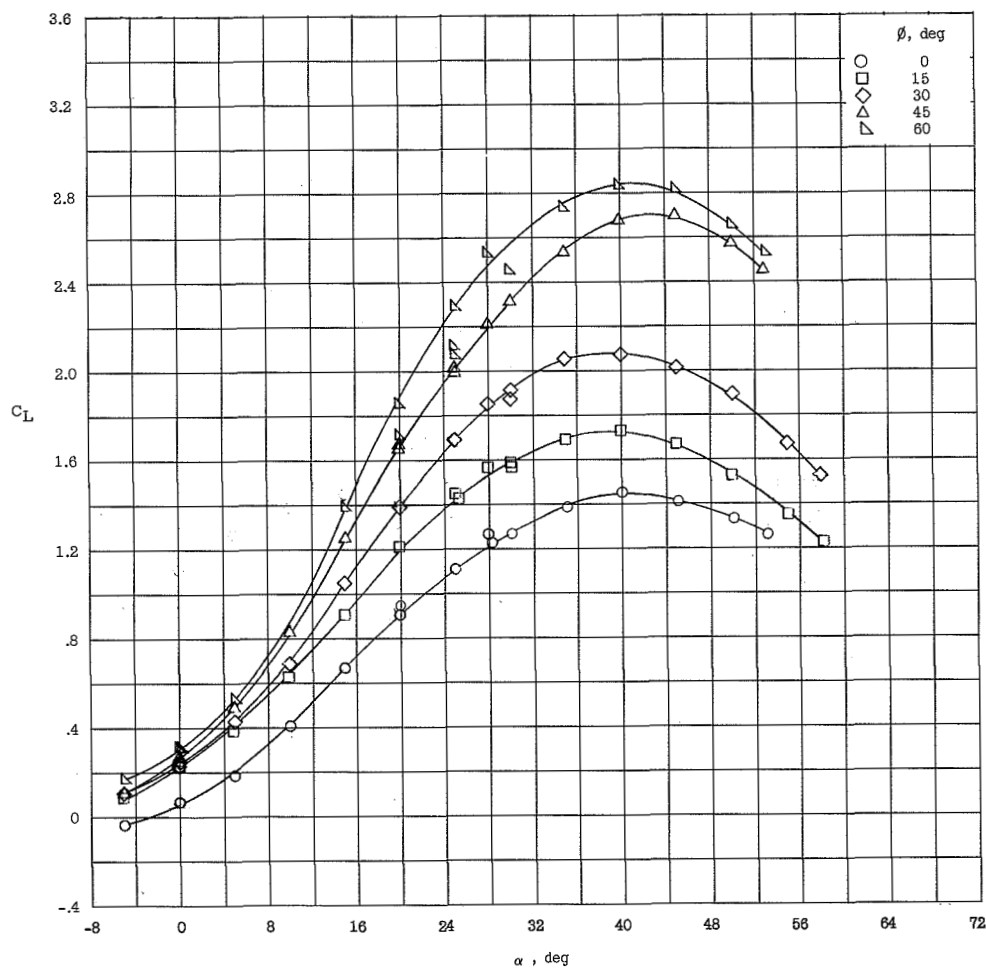
(a) C_L .

Figure 17.- Longitudinal characteristics of the conic-sectored series.
 $\theta_c = 10^\circ$; $h/R = 0.4$.

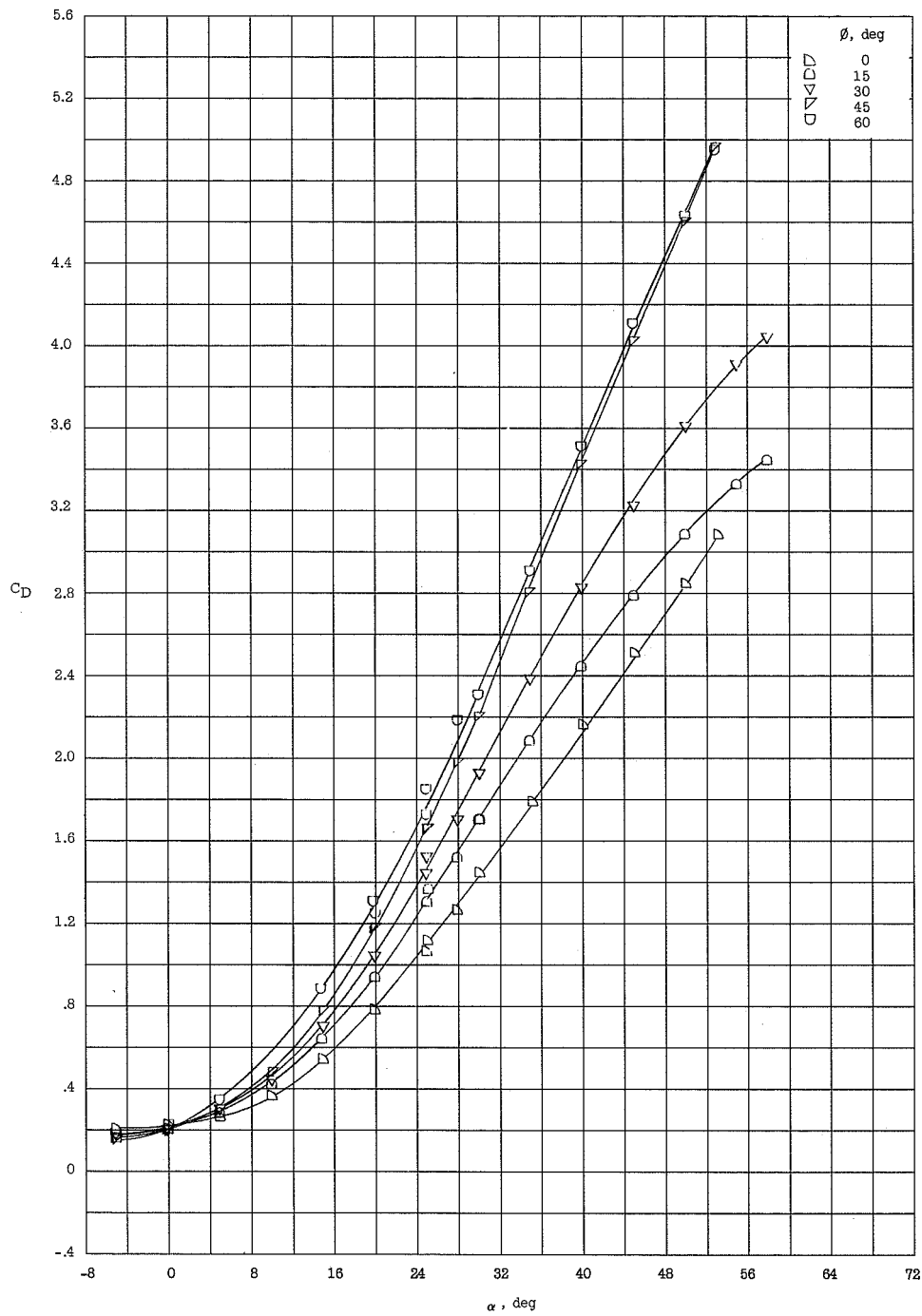
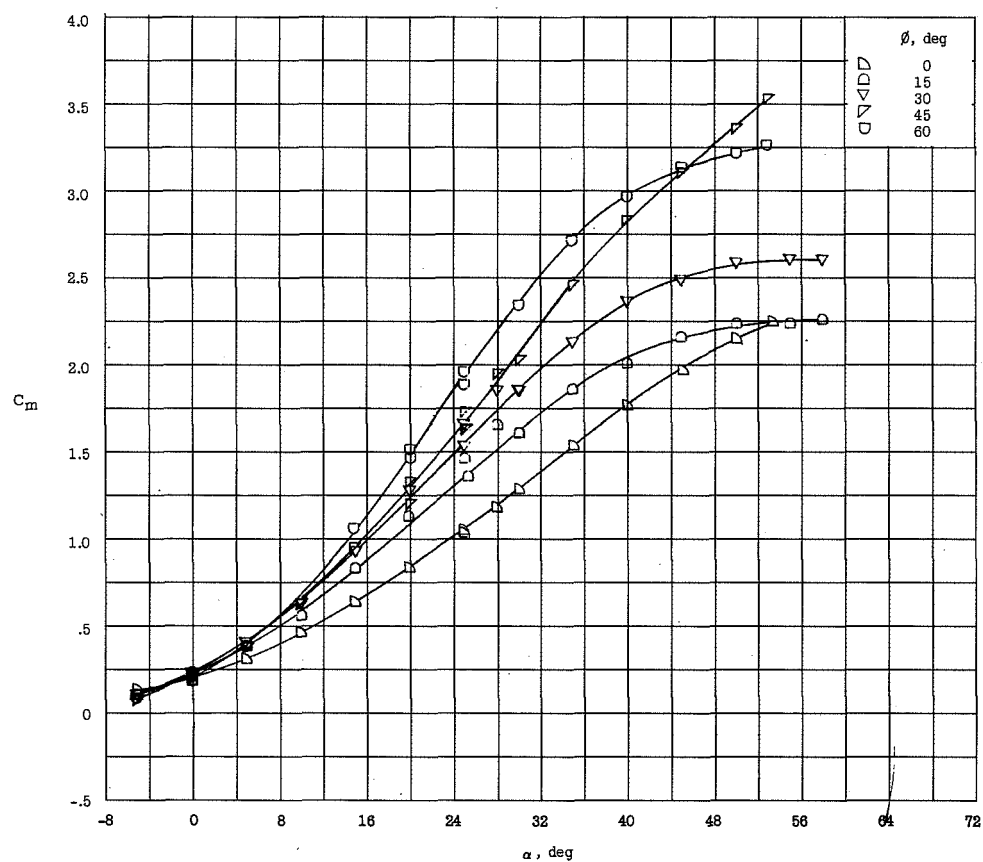
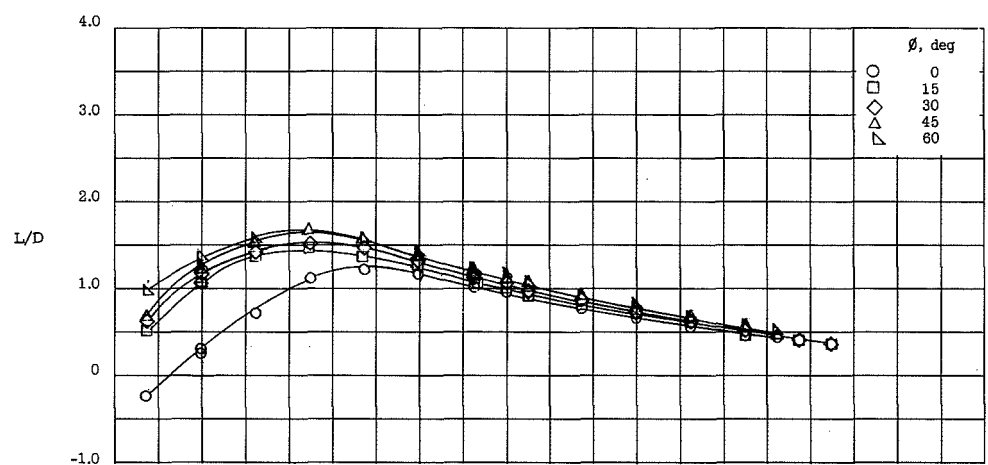
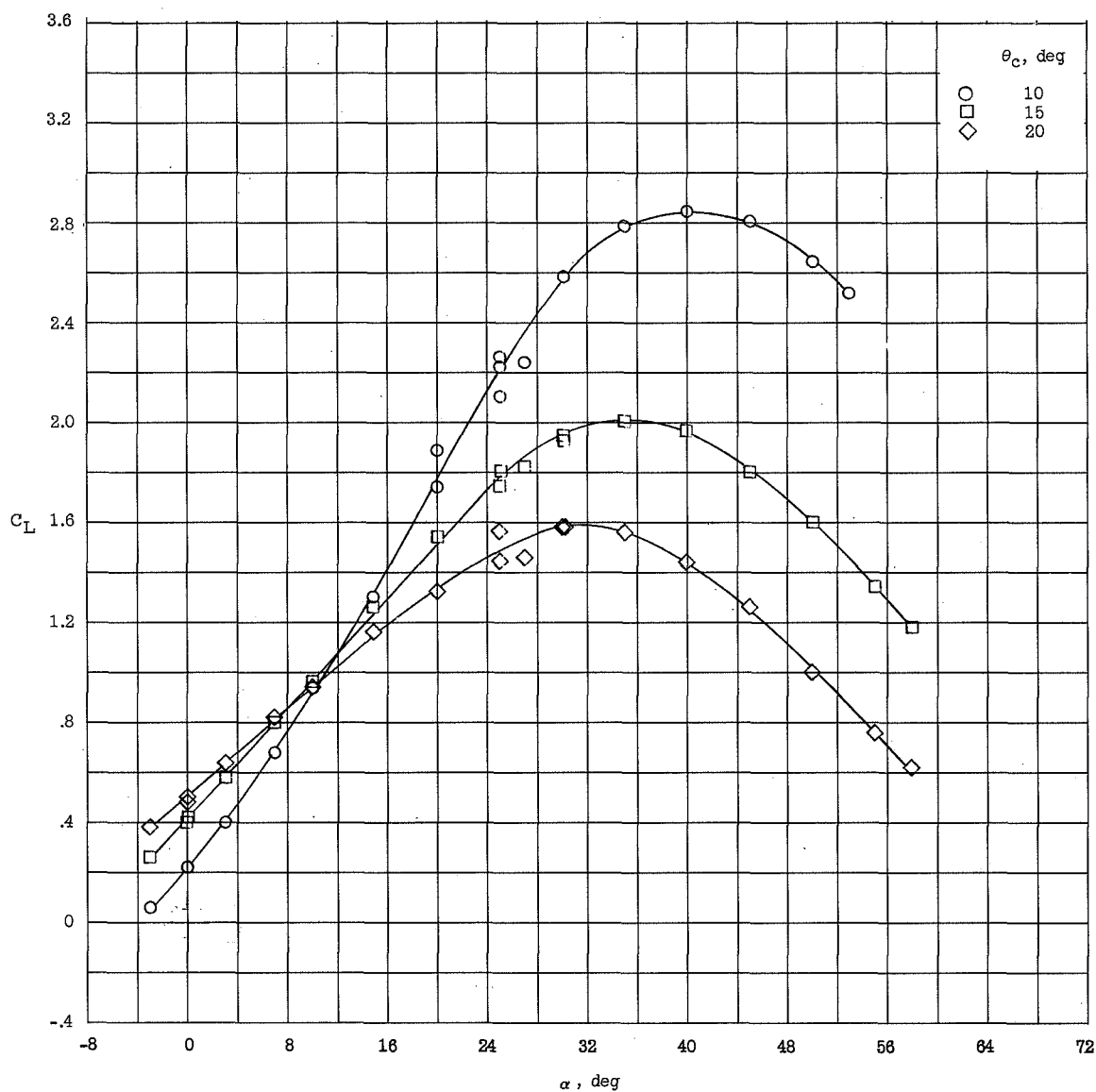
(b) C_D .

Figure 17.- Continued.



(c) L/D and C_m about the body base.

Figure 17.- Concluded.



(a) C_L .

Figure 18.- Longitudinal characteristics of the conic-sectored series.
 $\phi = 45^\circ$; $h/R = 0$.

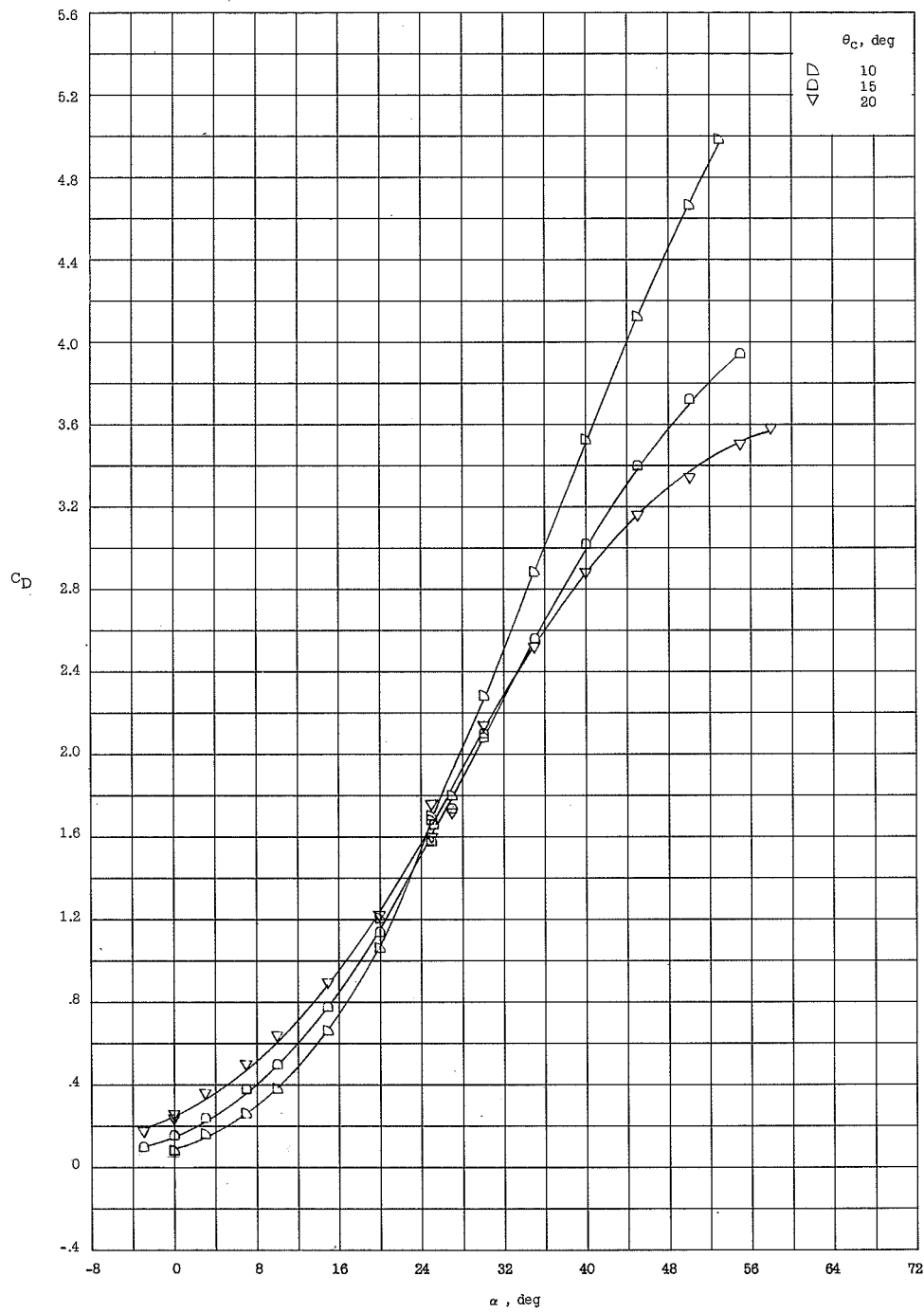
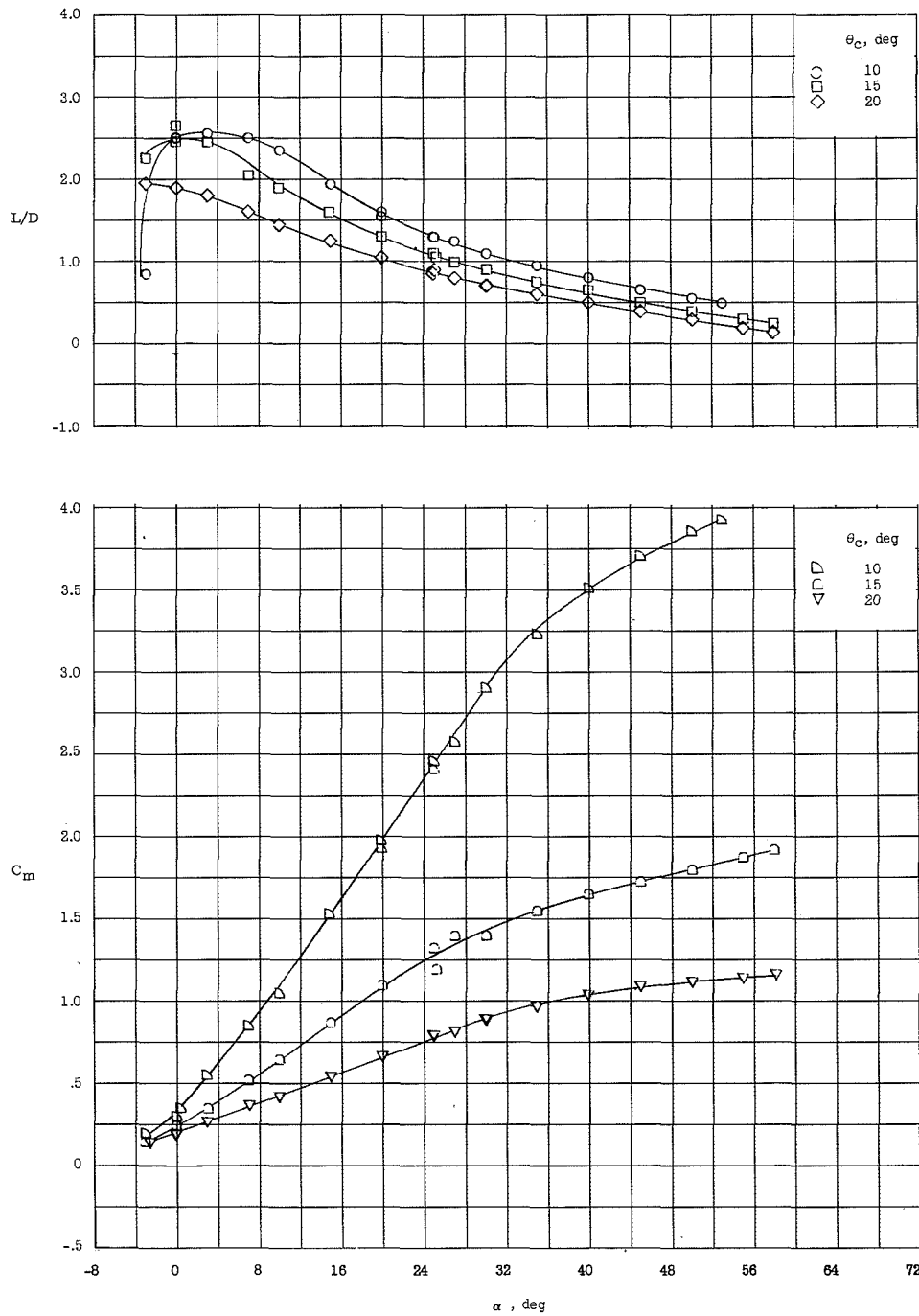
(b) C_D .

Figure 18.- Continued.

L-1437



(c) L/D and C_m about the body base.

Figure 18.- Concluded.

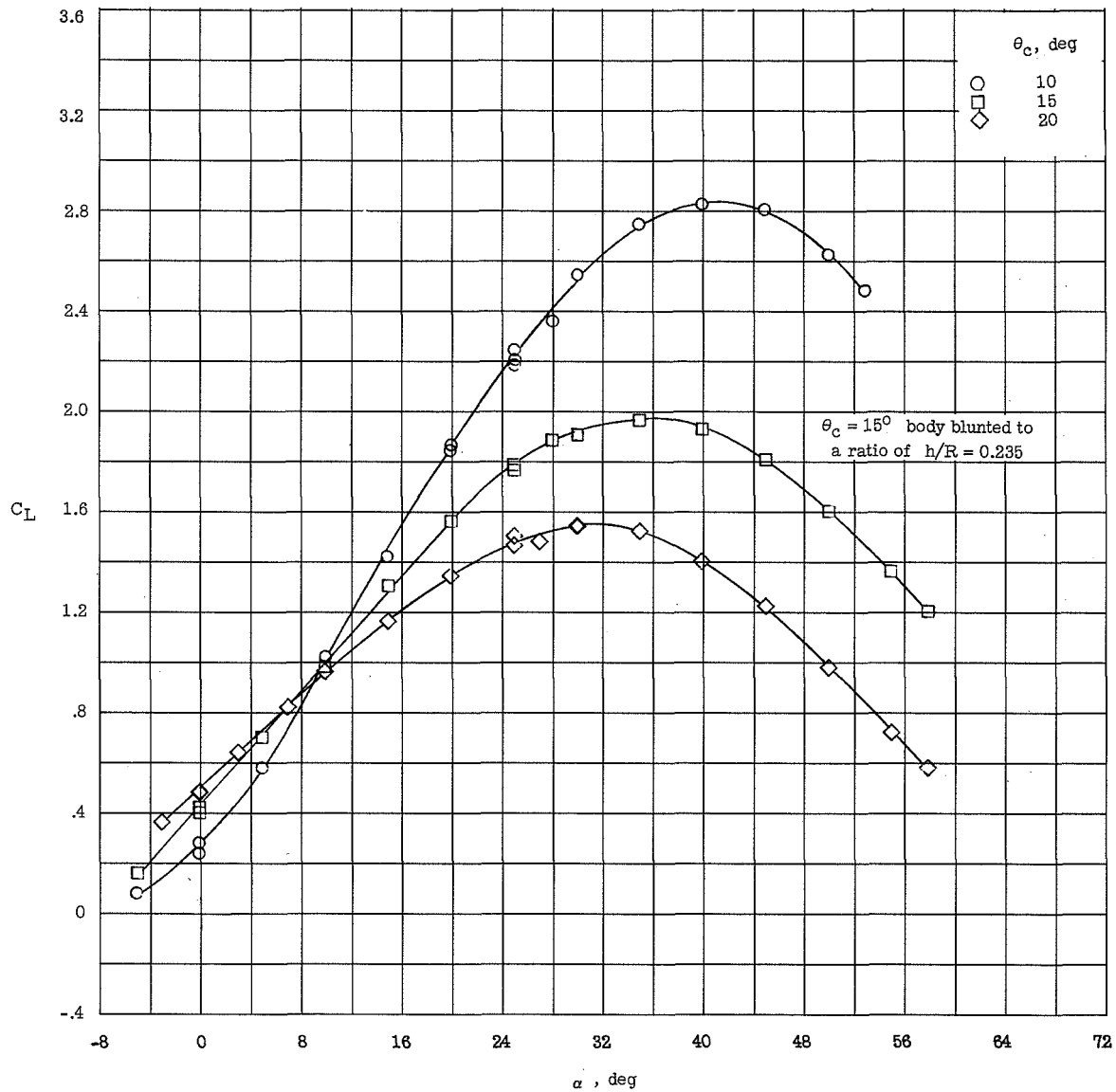
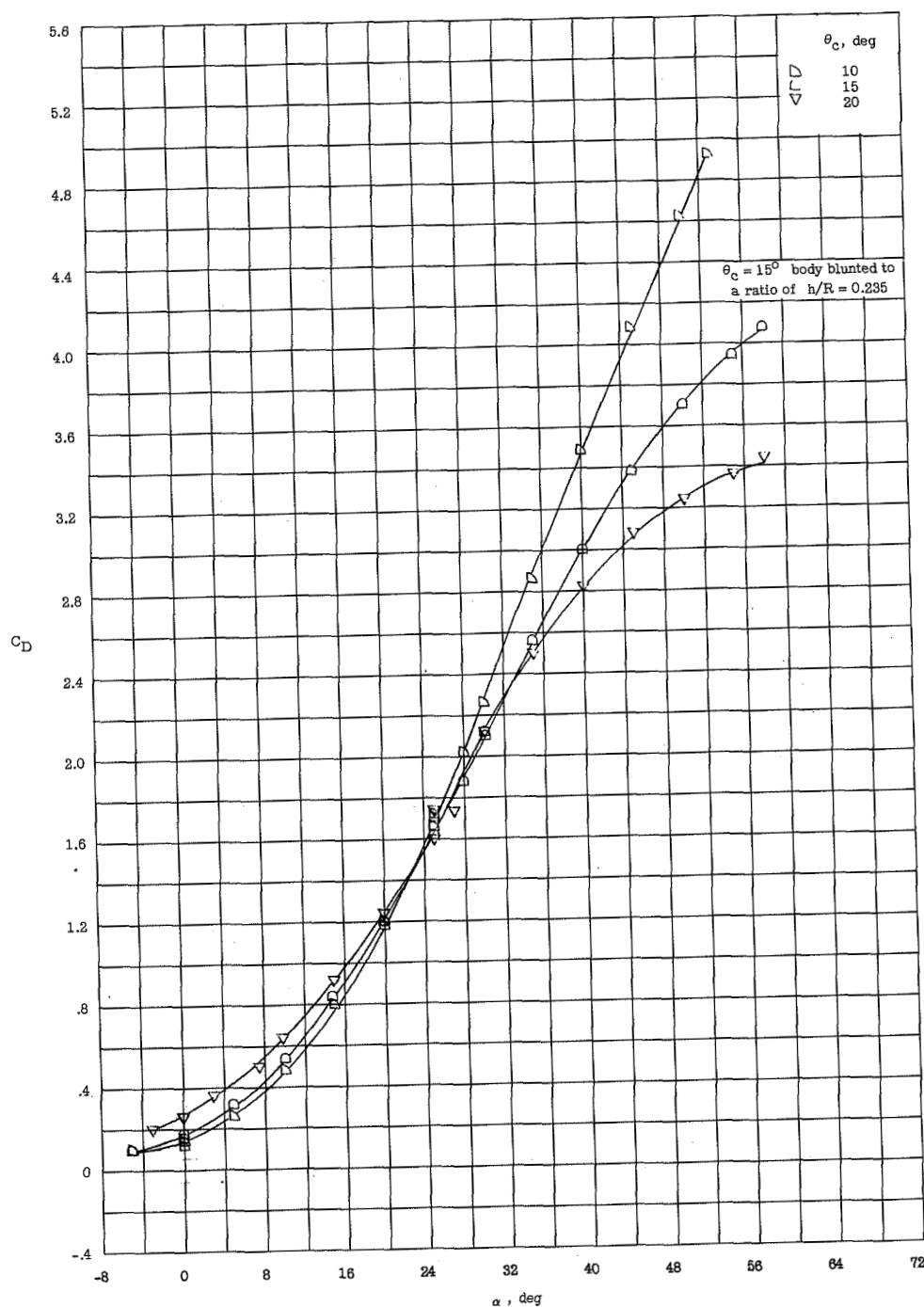
(a) C_L .

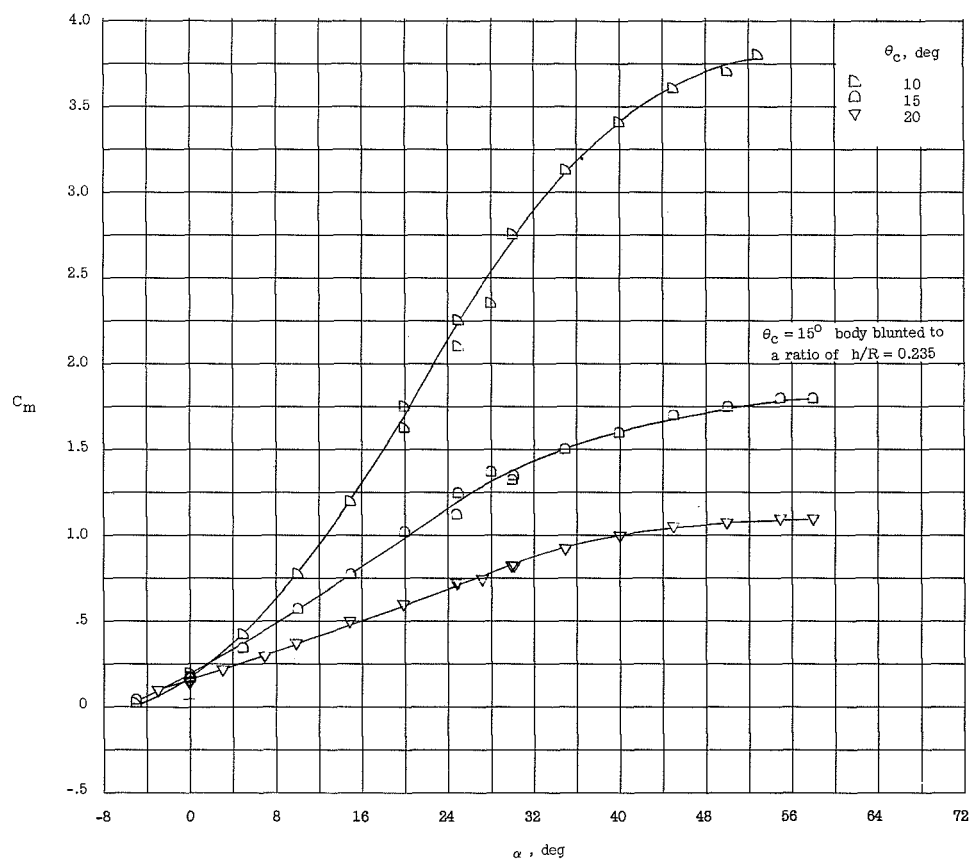
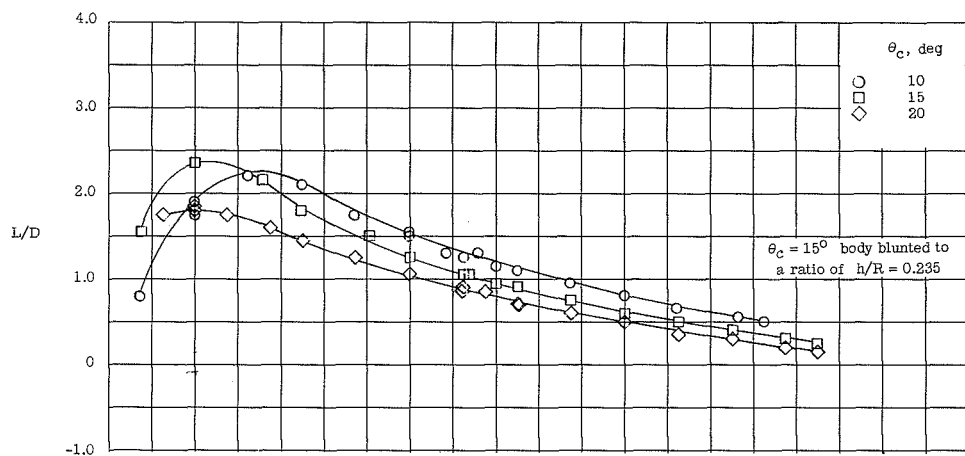
Figure 19.- Longitudinal characteristics of the conic-sectored series.
 $\phi = 45^\circ$; $h/R = 0.2$.

I-1437



(b) C_D .

Figure 19.- Continued.



(c) L/D and C_m about the body base.

Figure 19.- Concluded.

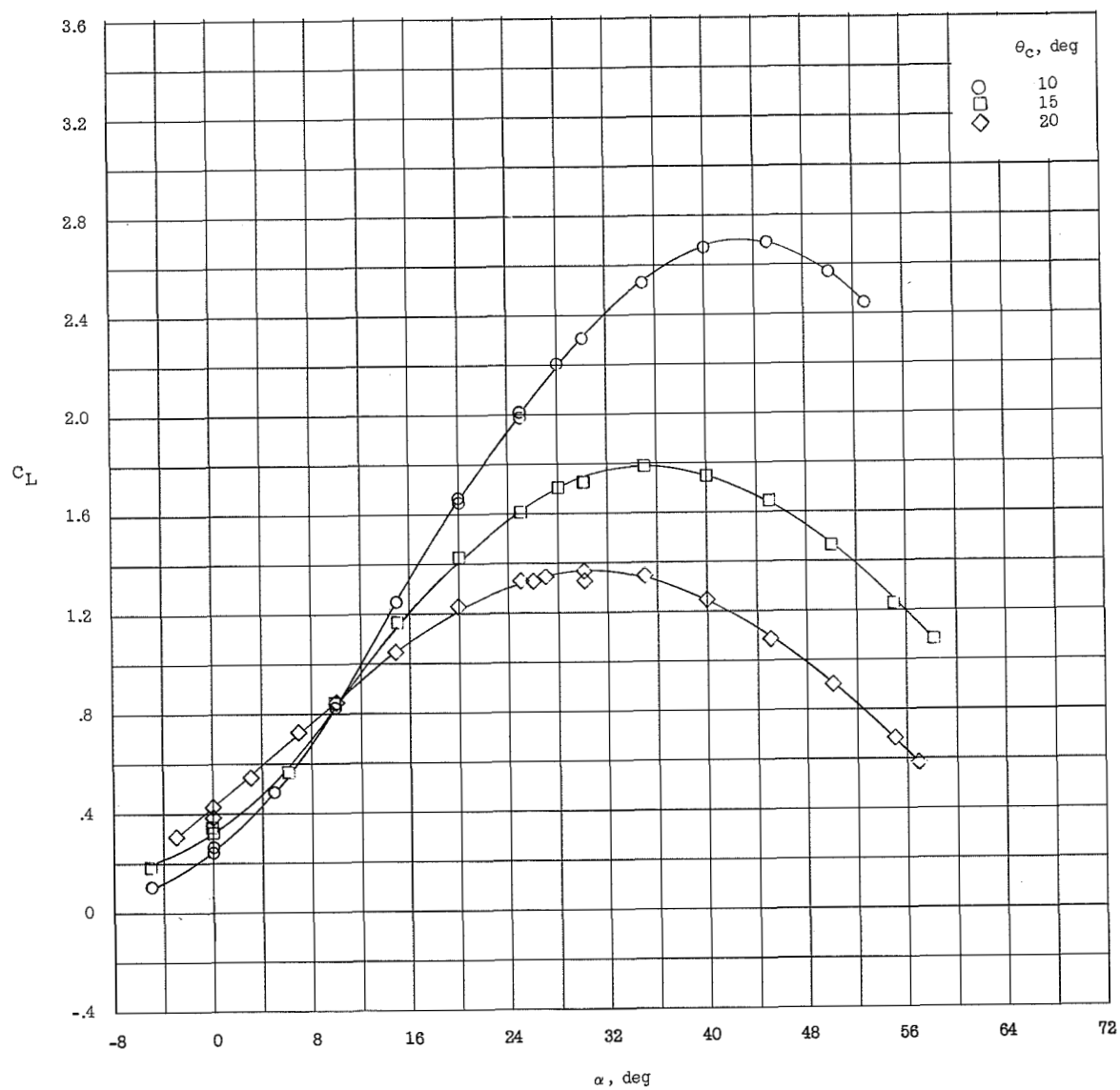
(a) C_L .

Figure 20.- Longitudinal characteristics of the conic-sectored series.
 $\phi = 45^\circ$; $h/R = 0.4$.

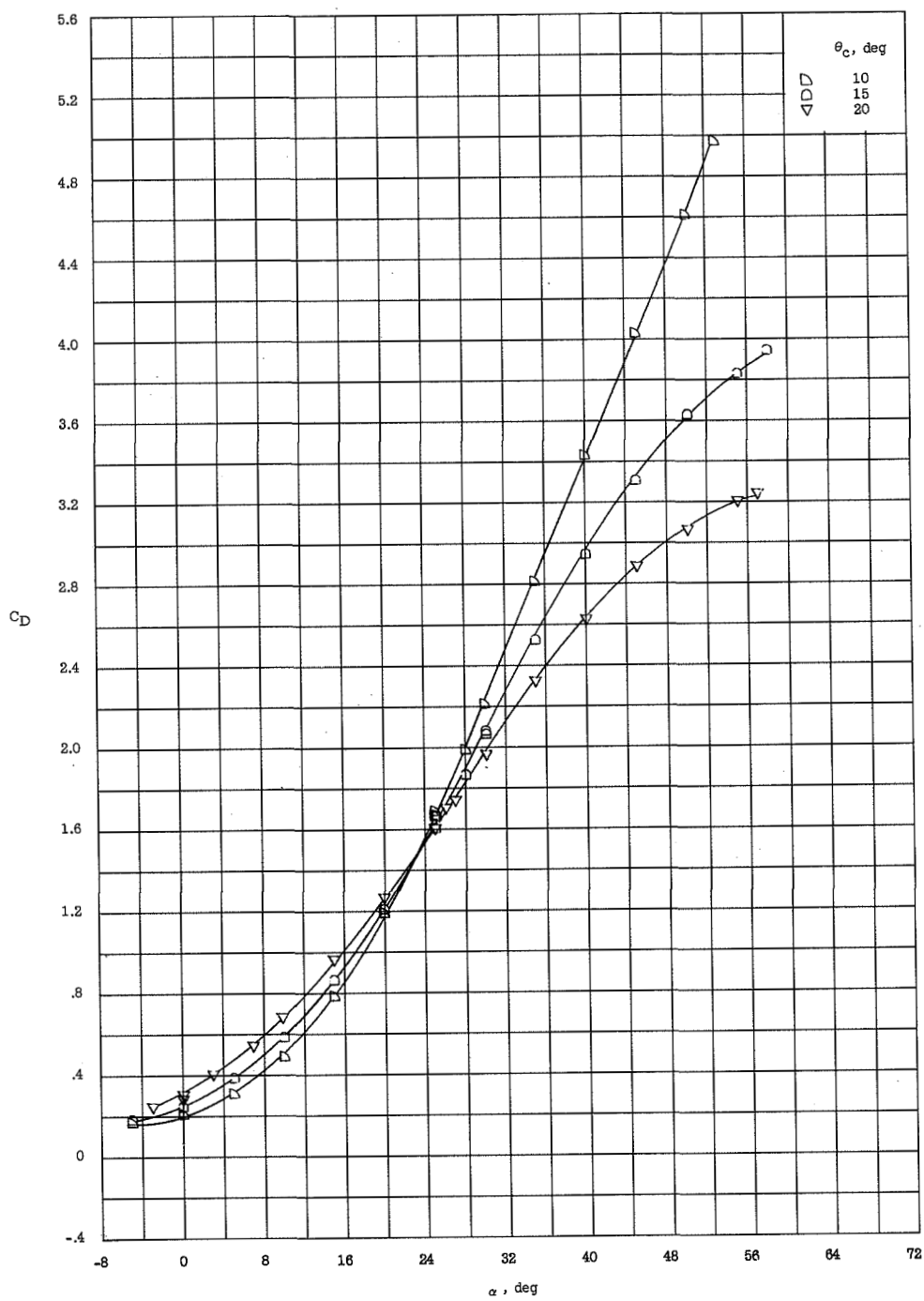
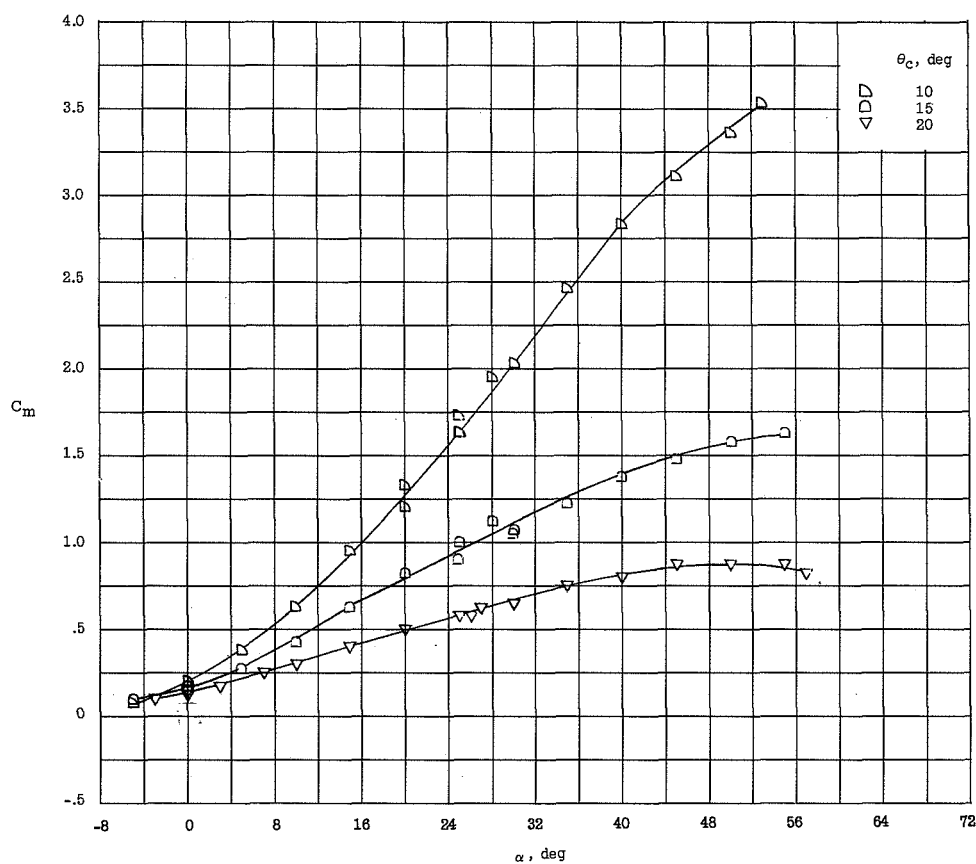
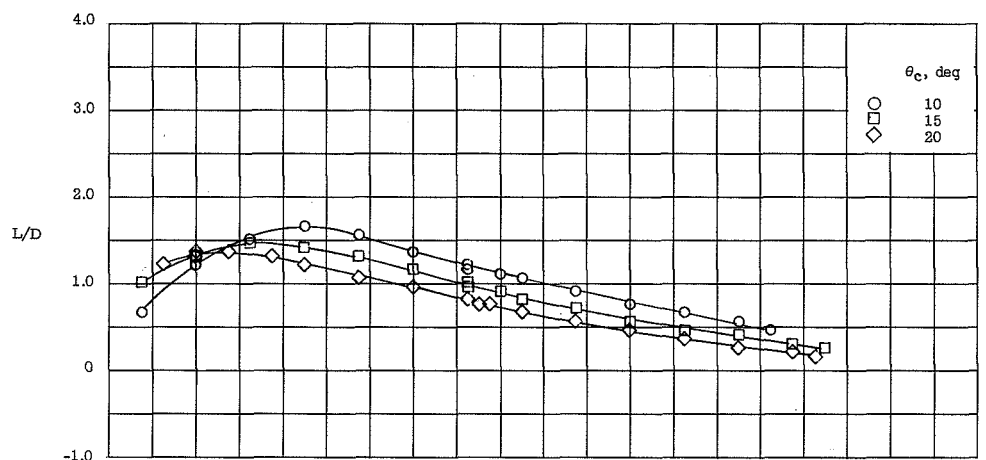
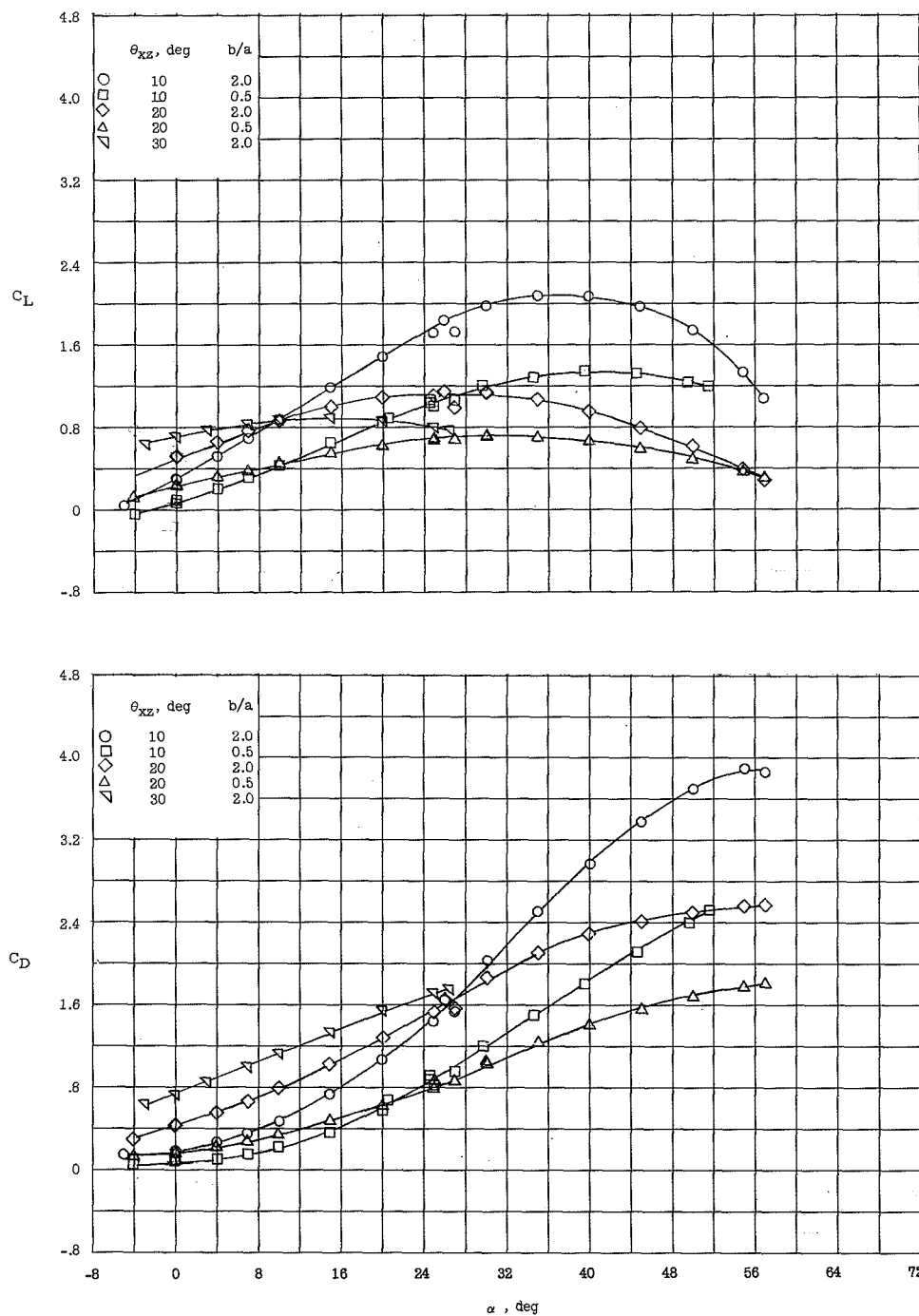
(b) C_D .

Figure 20.- Continued.



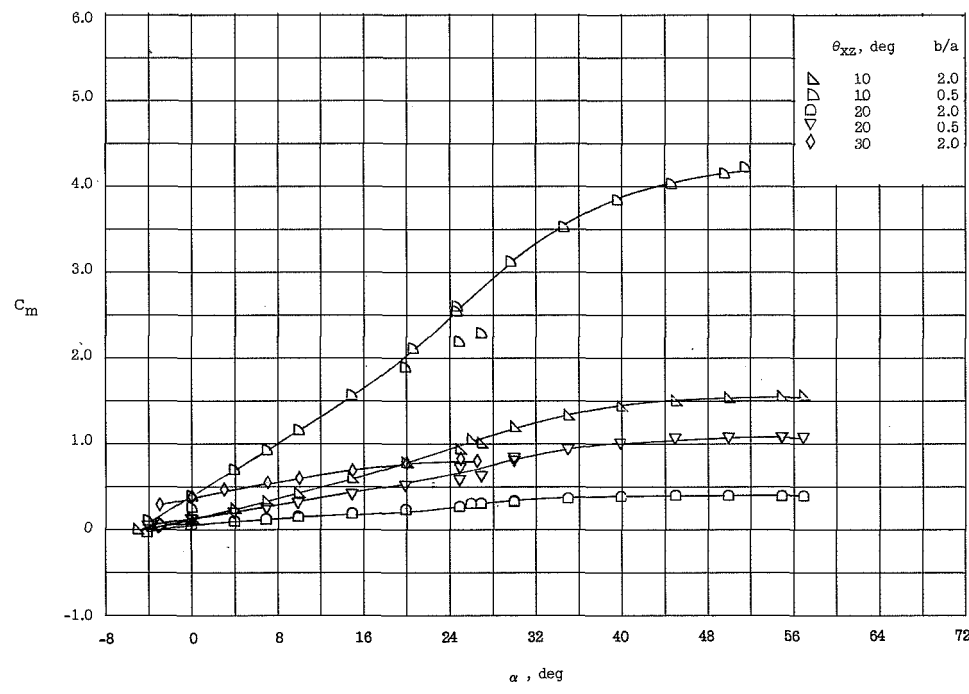
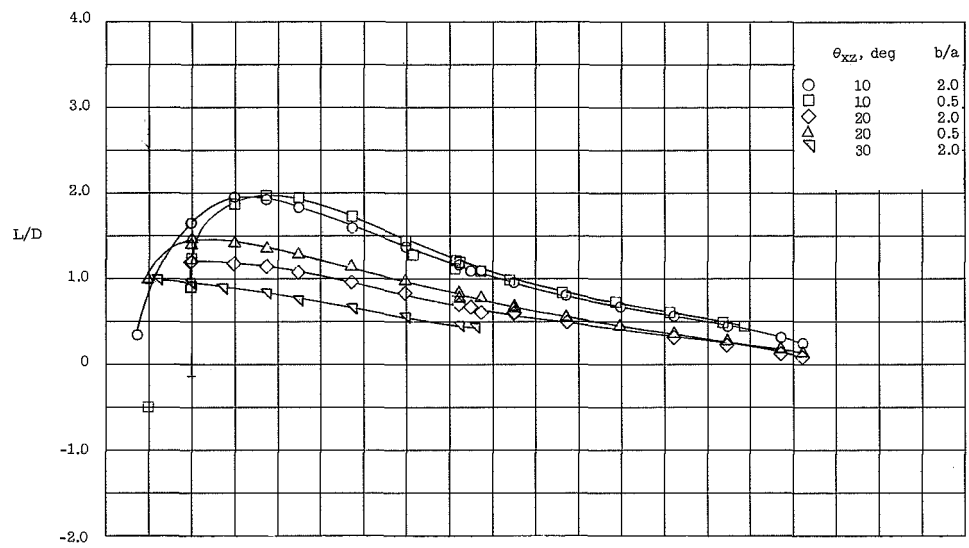
(c) L/D and C_m about the body base.

Figure 20.- Concluded.

(a) C_L and C_D .Figure 21.- Longitudinal characteristics of the elliptic half-cone series. $h/R = 0$.



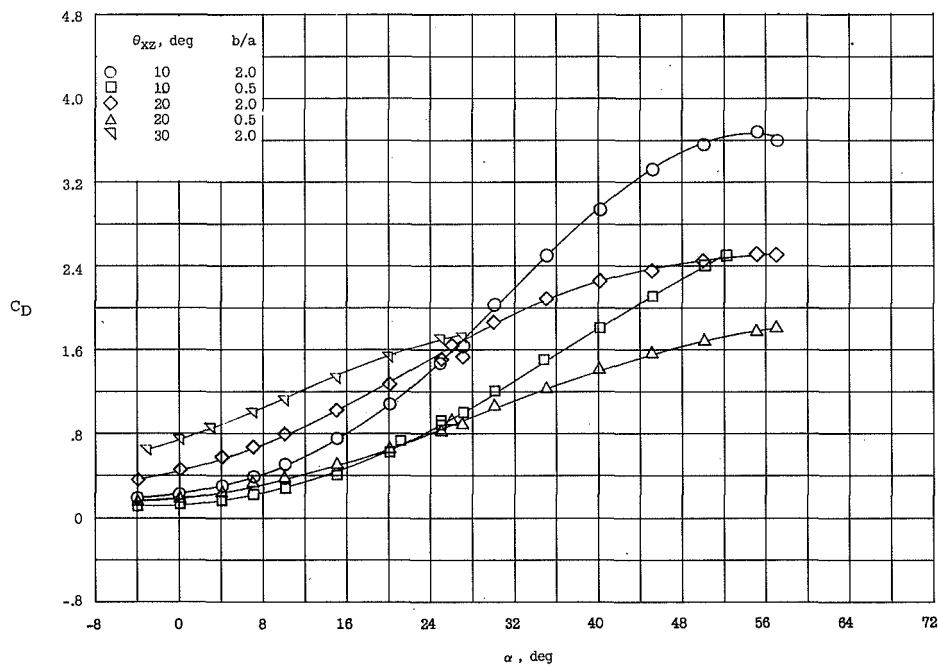
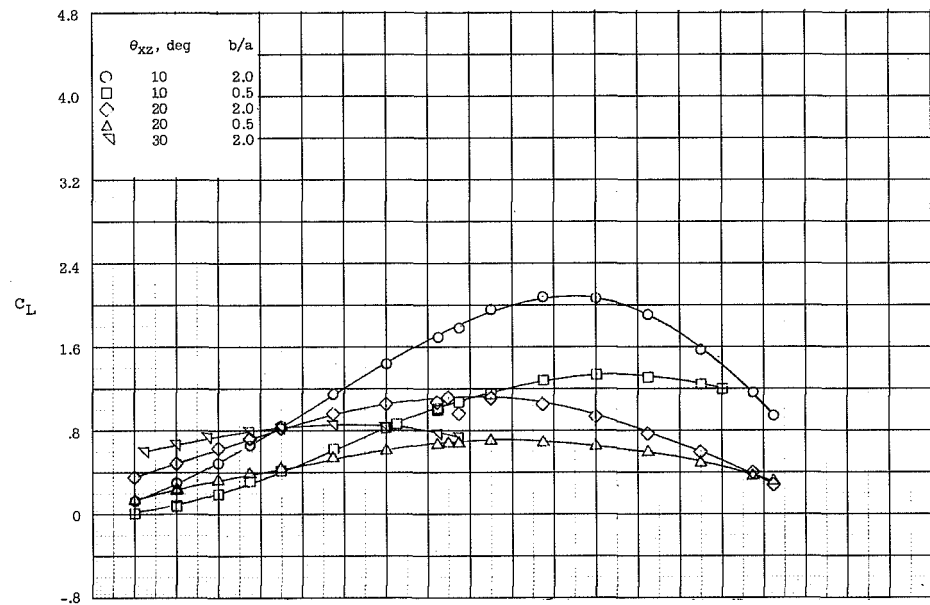
I-1437



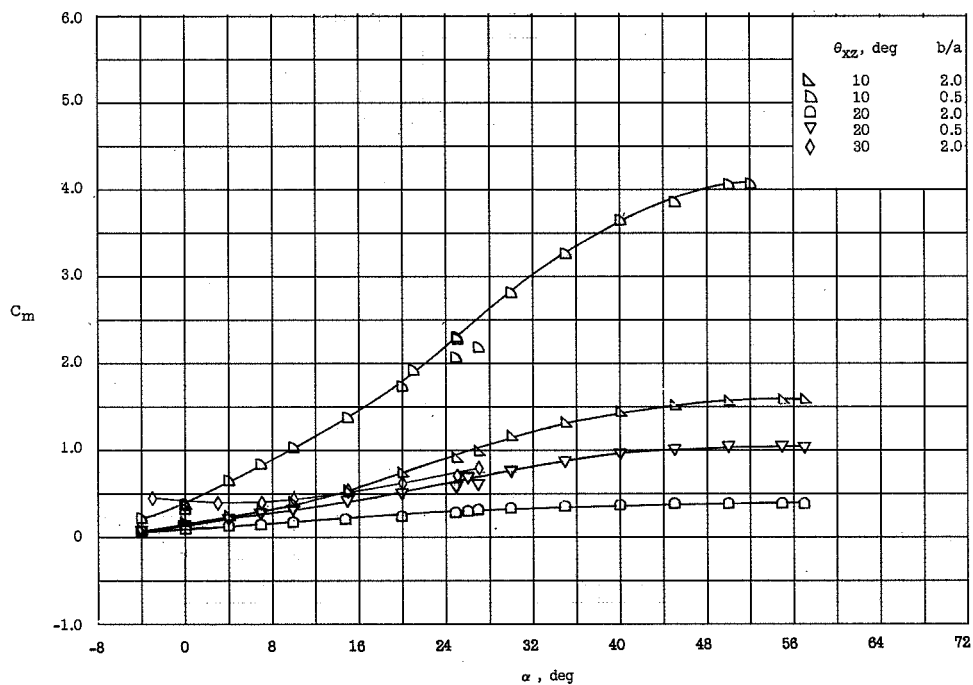
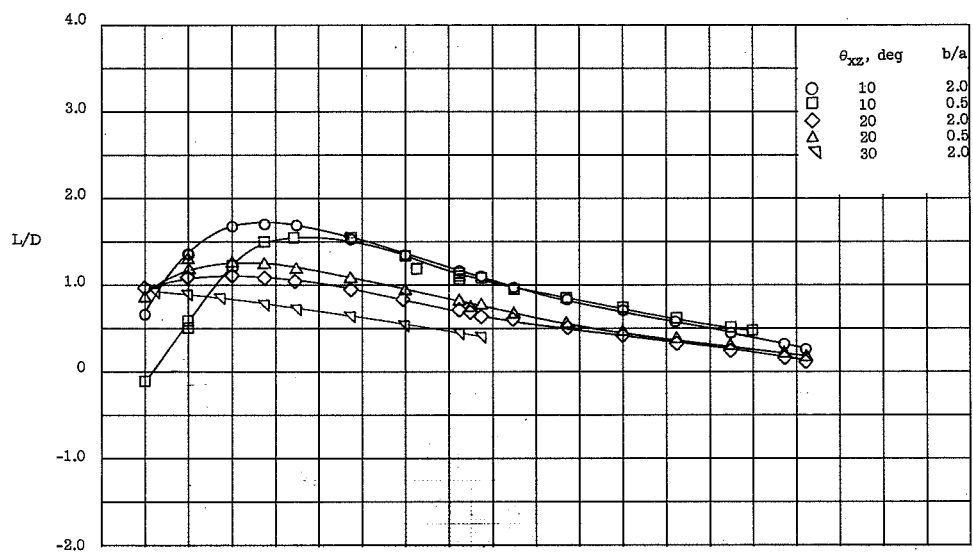
(b) L/D and C_m about the model base.

Figure 21.- Concluded.



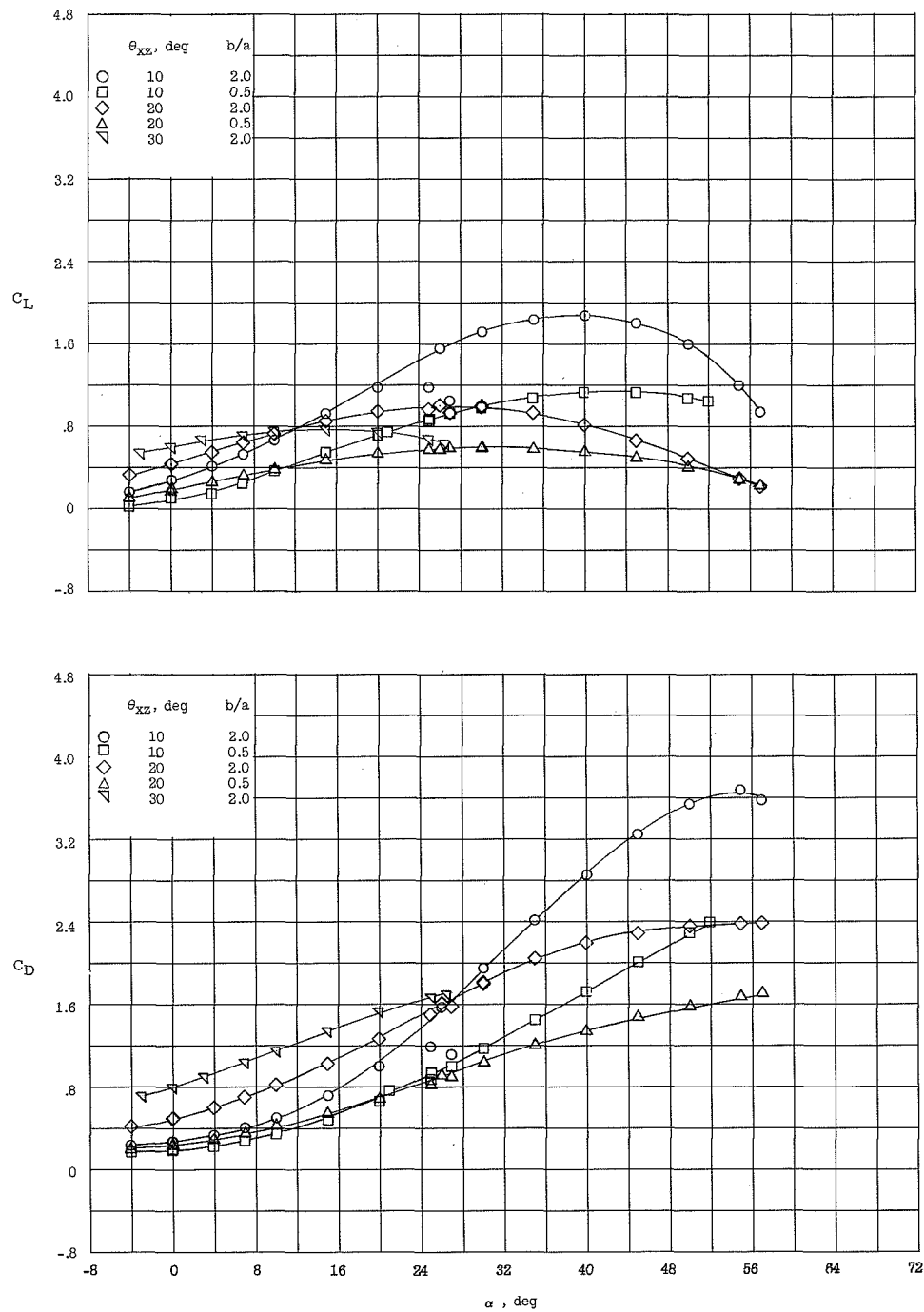
(a) C_L and C_D .Figure 22.- Longitudinal characteristics of the elliptic half-cone series. $h/R = 0.2$.

L-1437

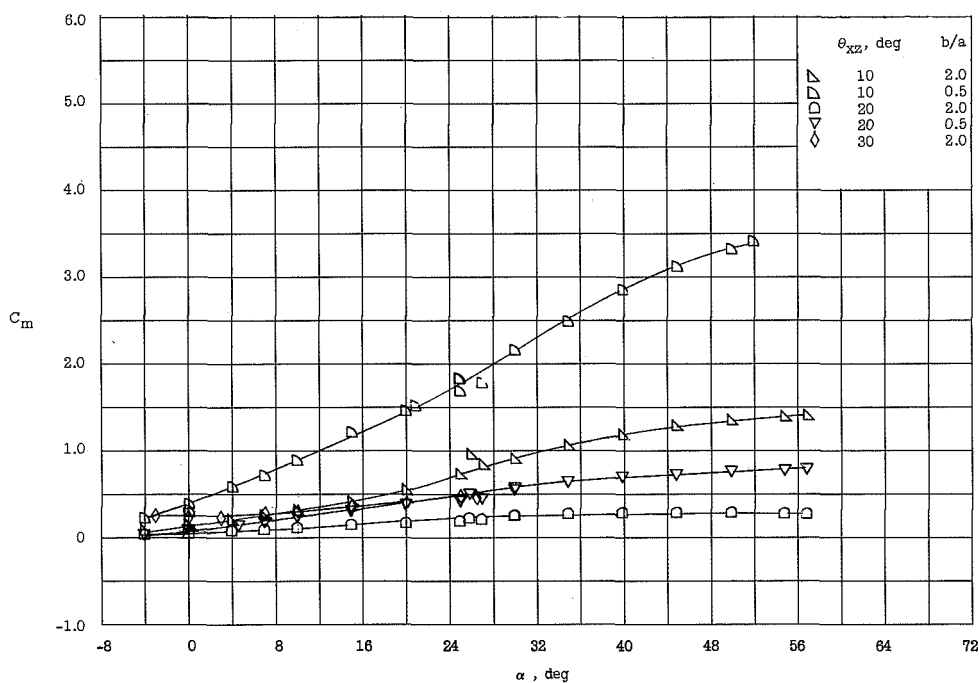
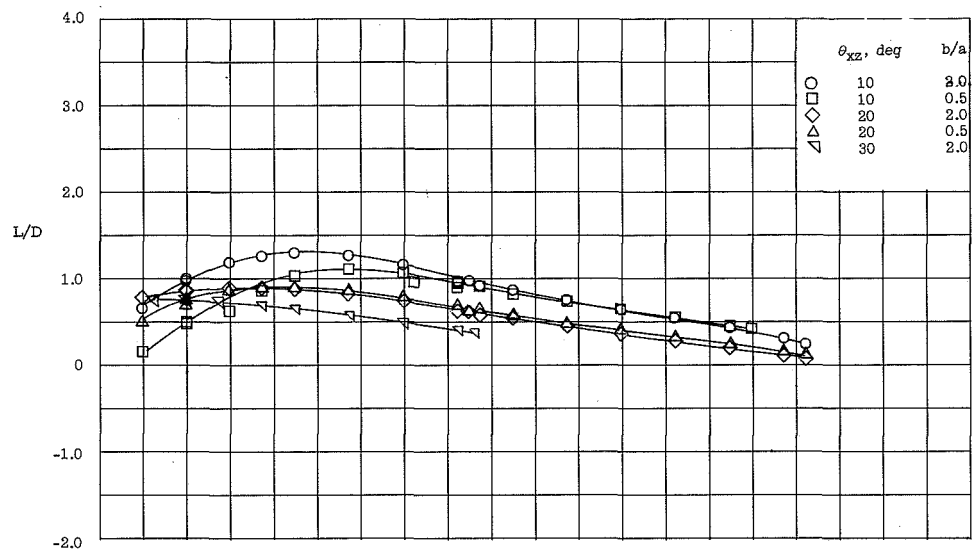


(b) L/D and C_m about the body base.

Figure 22.- Concluded.

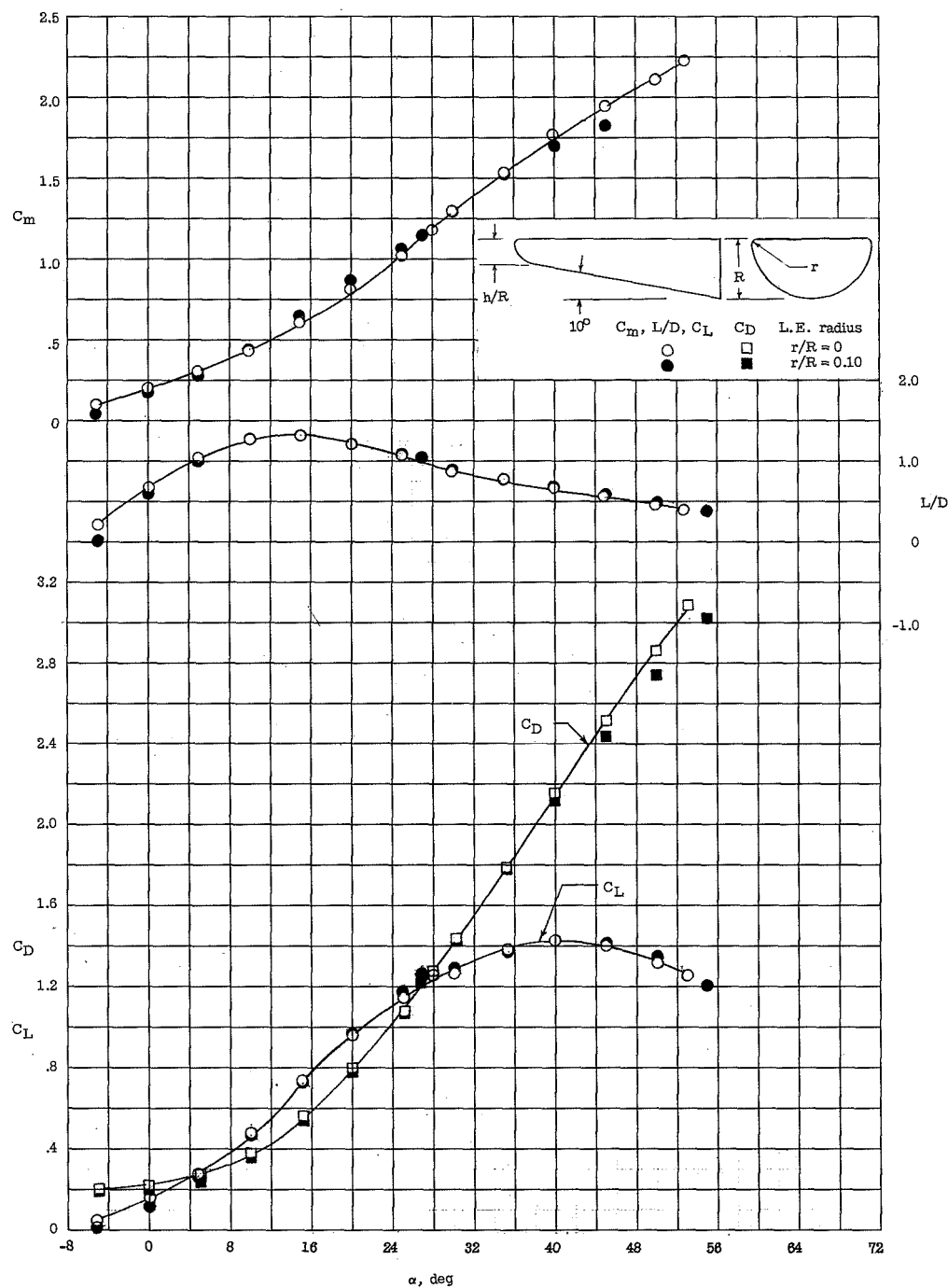
(a) C_L and C_D.Figure 23.- Longitudinal characteristics of the elliptic half-cone series. $h/R = 0.4$.

L-1437



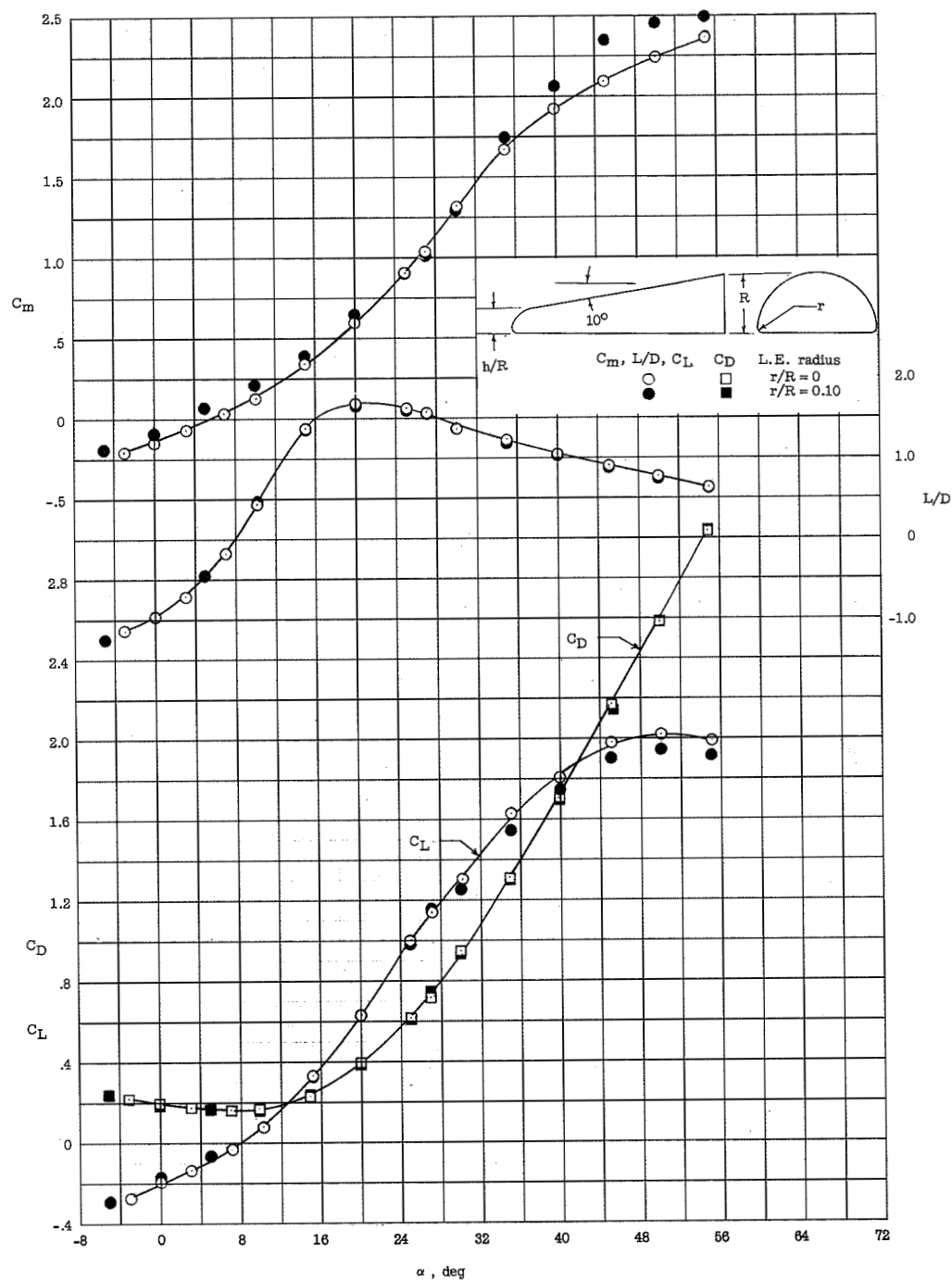
(b) L/D and C_m about the body base.

Figure 23.- Concluded.



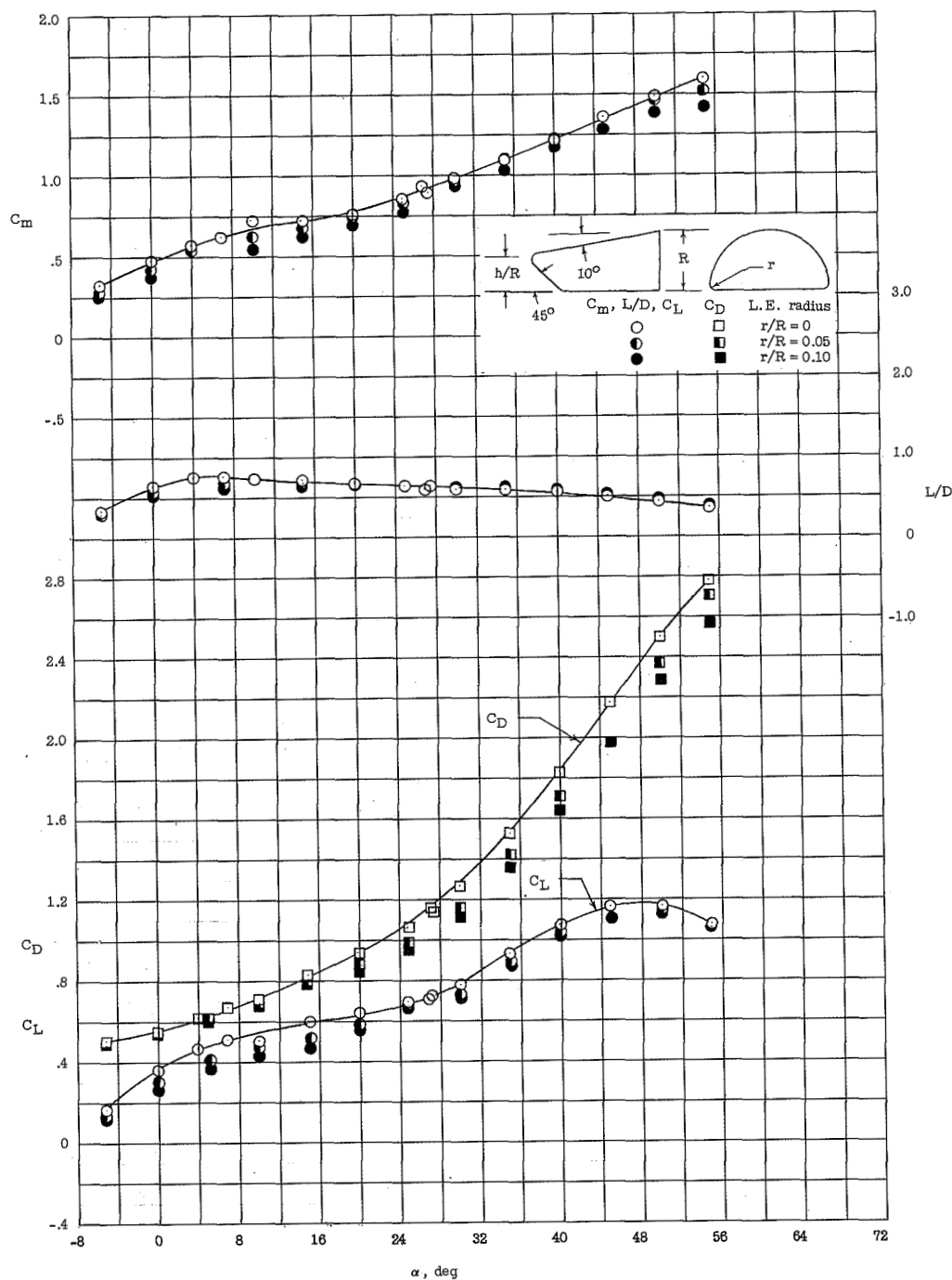
(a) Spherically blunted round-bottom half-cone.

Figure 24.- Effect of leading-edge rounding on the longitudinal characteristics of several lifting-body configurations.



(b) Spherically blunted flat-bottom half-cone.

Figure 24.- Continued.



(c) Flat-bottom half-cone with a flat canted nose.

Figure 24.- Concluded.

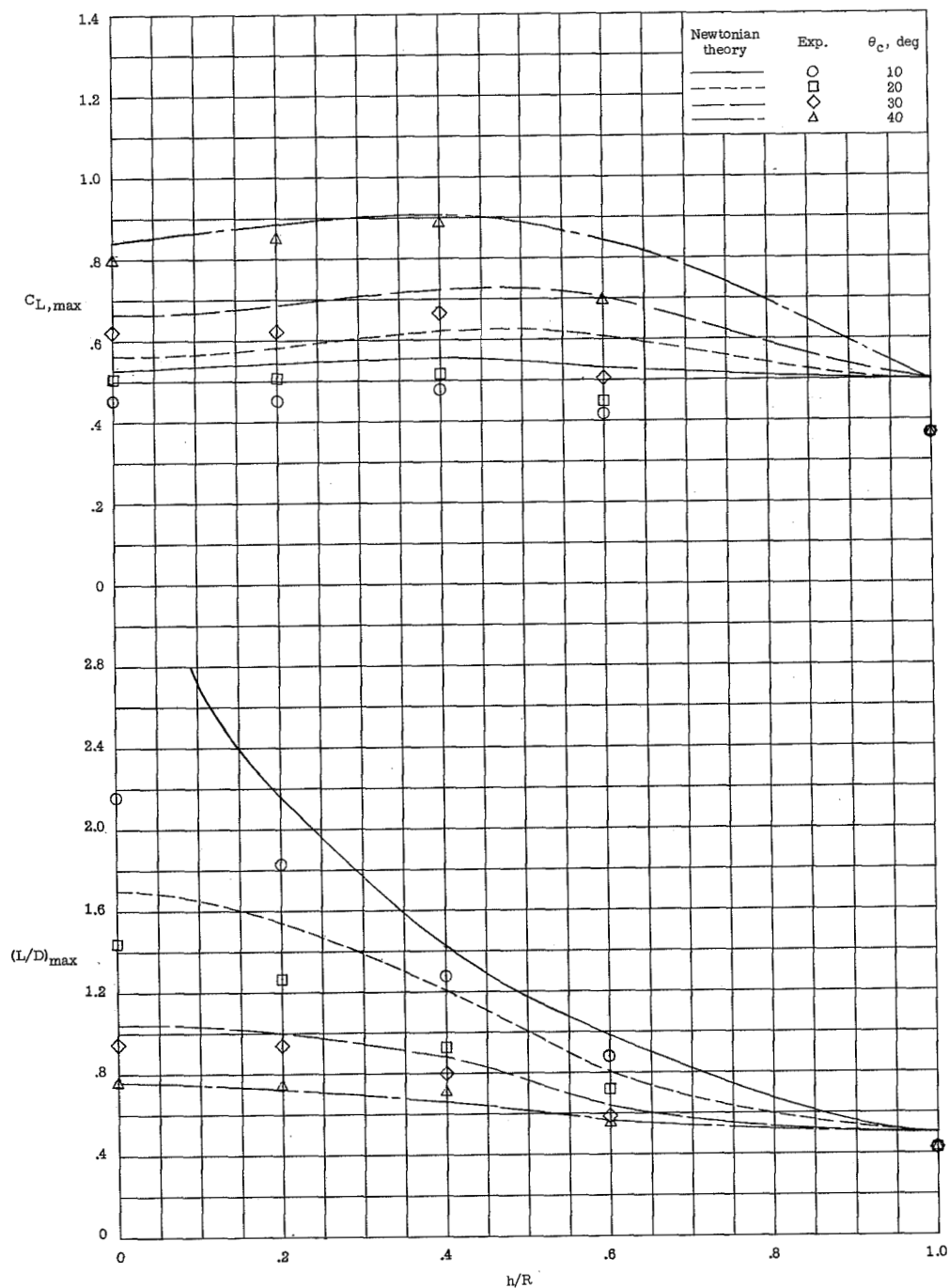


Figure 25.- Effect of varying nose bluntness on $C_{L,max}$ and $(L/D)_{max}$ of the round-bottom half-cone series. ($C_{L,max}$ based on planform area.)

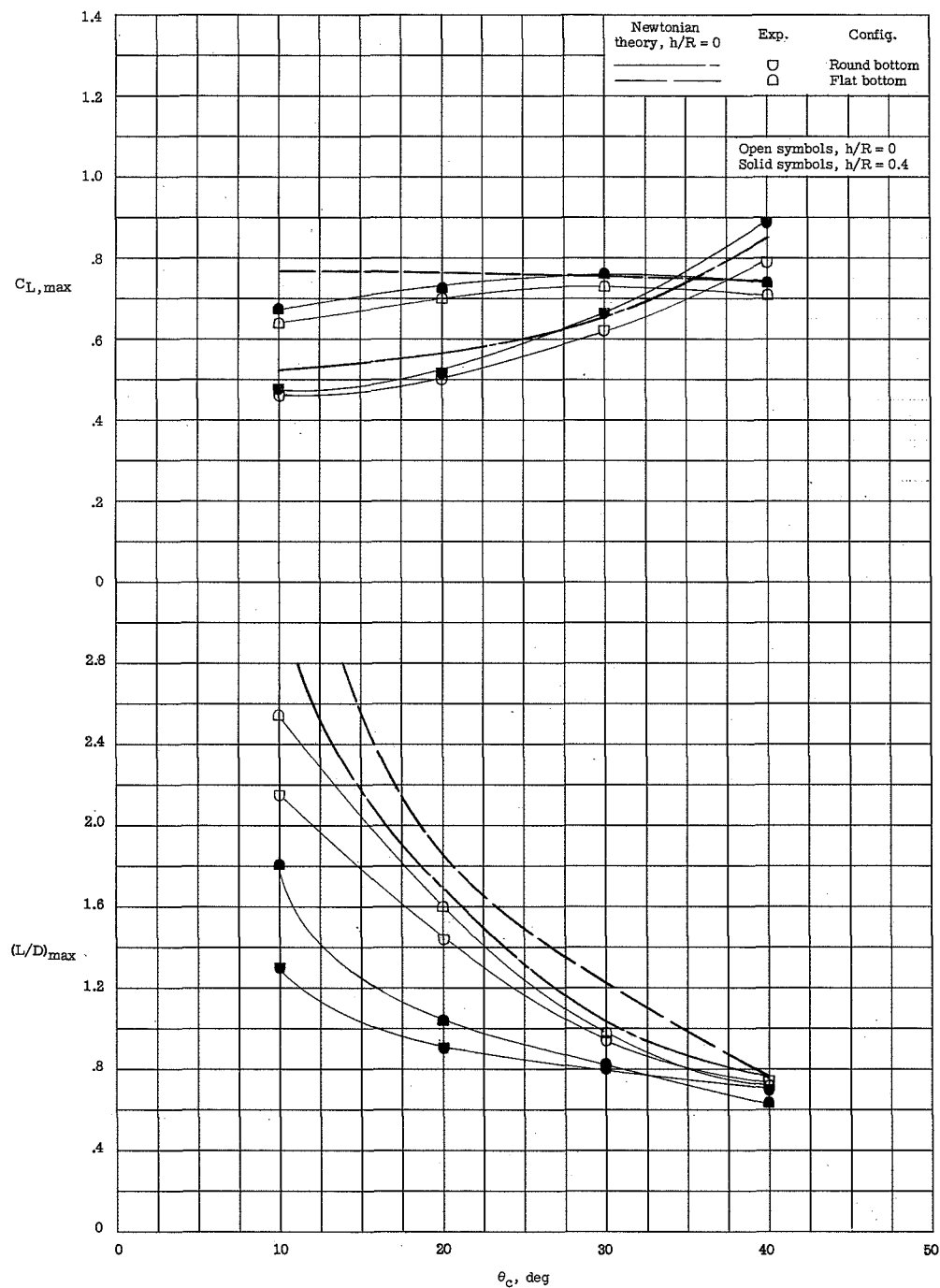


Figure 26.- Comparison of $C_{L,max}$ and $(L/D)_{max}$ of the round-bottom and flat-bottom spherically blunted half-cone series with varying cone semiapex angle. ($C_{L,max}$ based on planform area.)

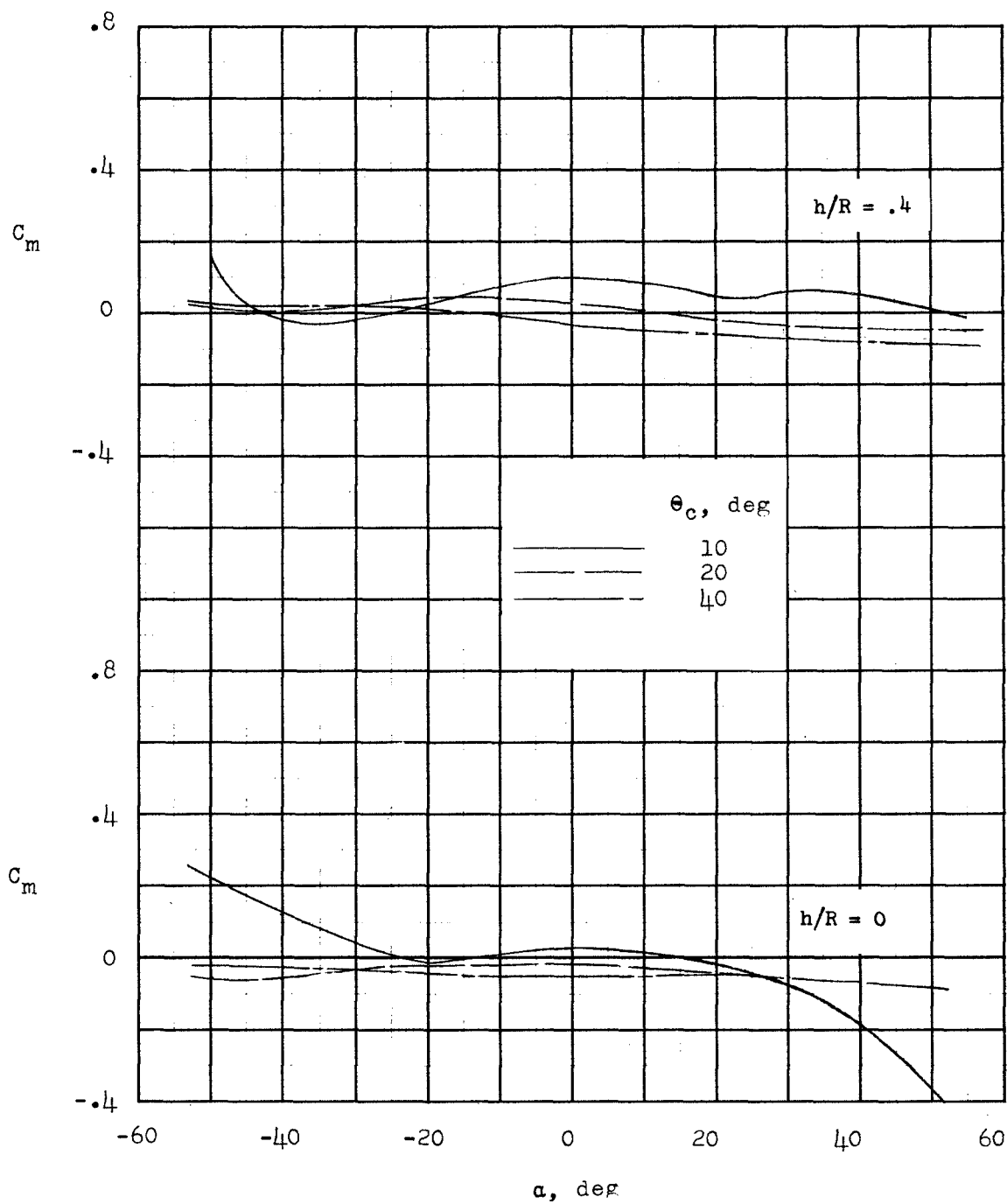


Figure 27.- Faired experimental pitching-moment characteristics about the body center of gravity of the round-bottom half-cone series.

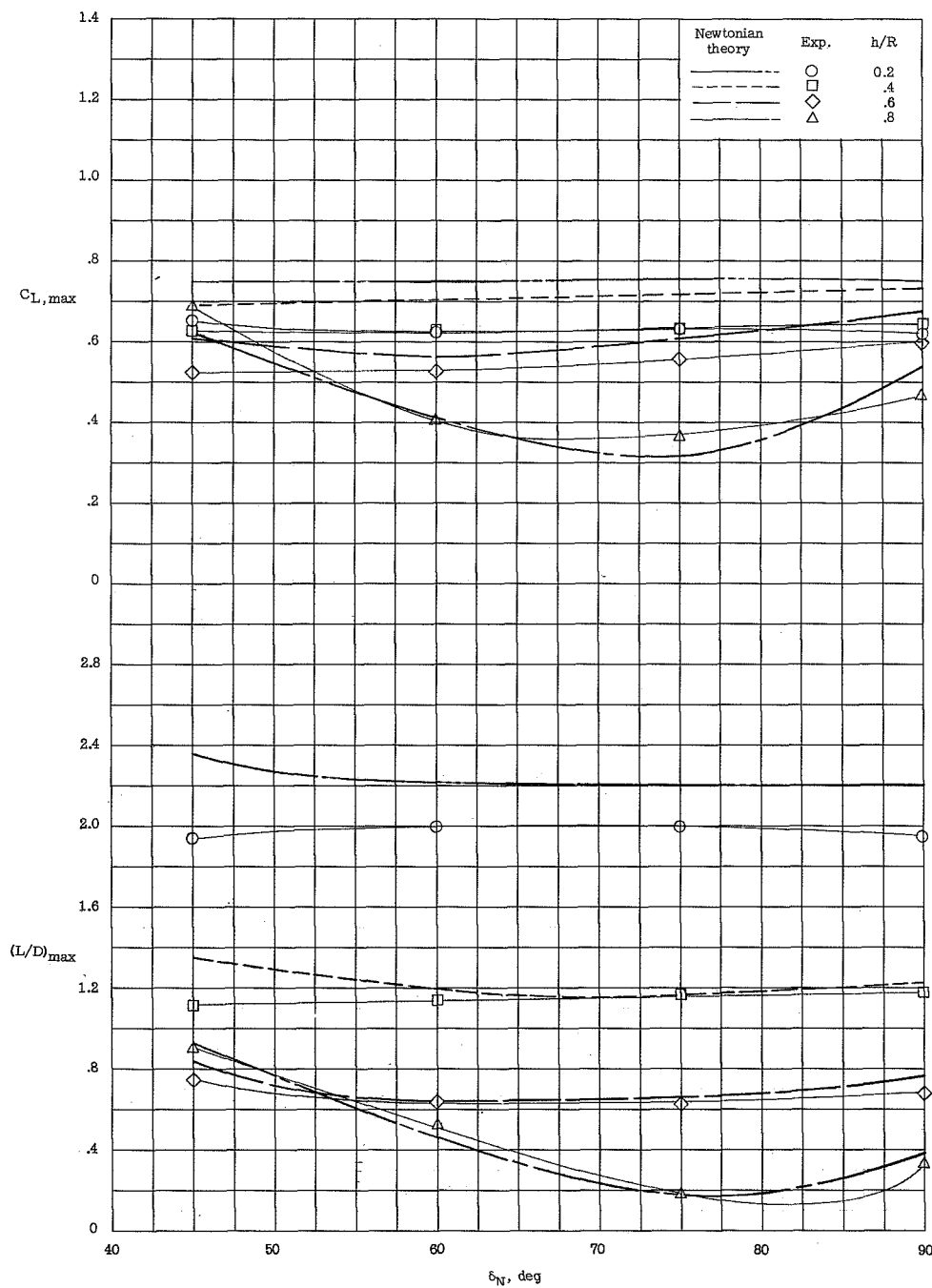


Figure 28.- Effect of varying nose bluntness and cant on $C_{L,max}$ and $(L/D)_{max}$ of the flat-bottom half-cone series of varying nose bluntness and cant. ($C_{L,max}$ based on planform area.) $\theta_c = 10^\circ$.

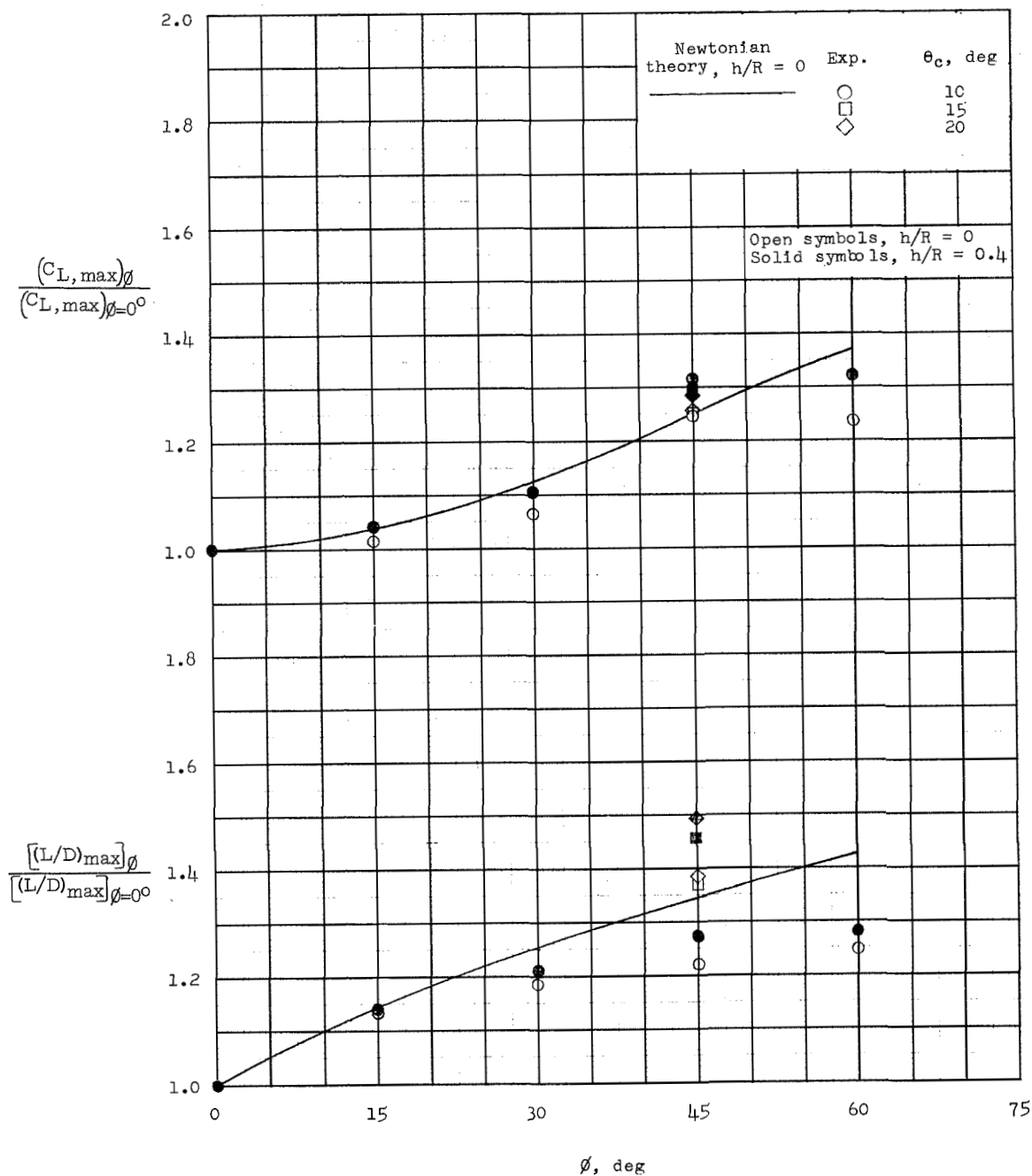


Figure 29.- Effect of increasing the radial cutoff angle ϕ on $C_{L,max}$ and $(L/D)_{max}$ of the conic-sectored series. ($C_{L,max}$ based on plan-form area.)

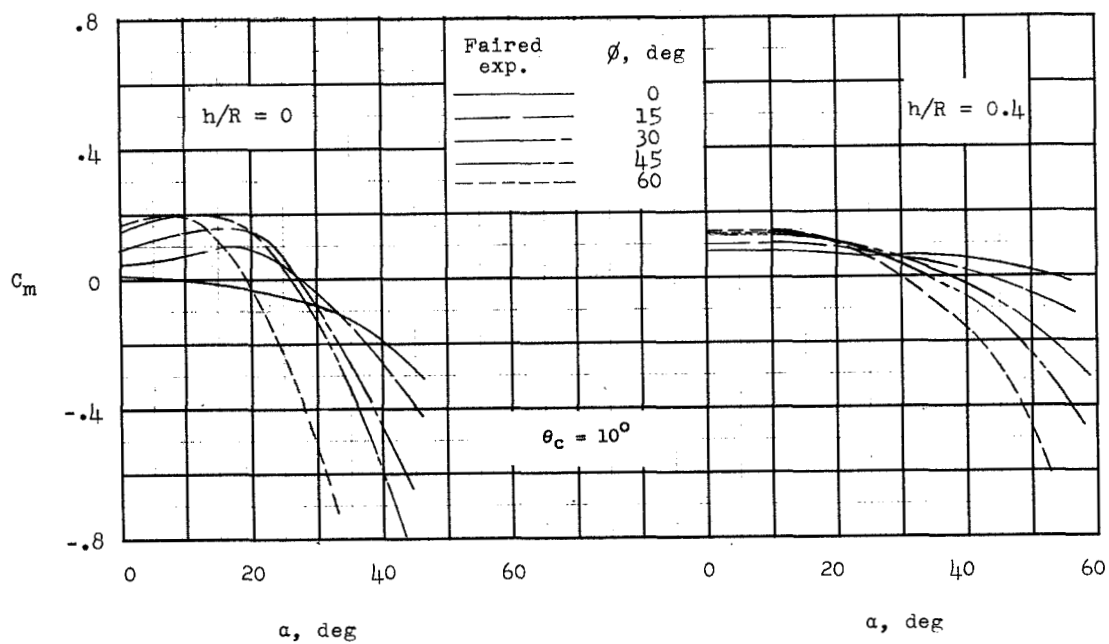
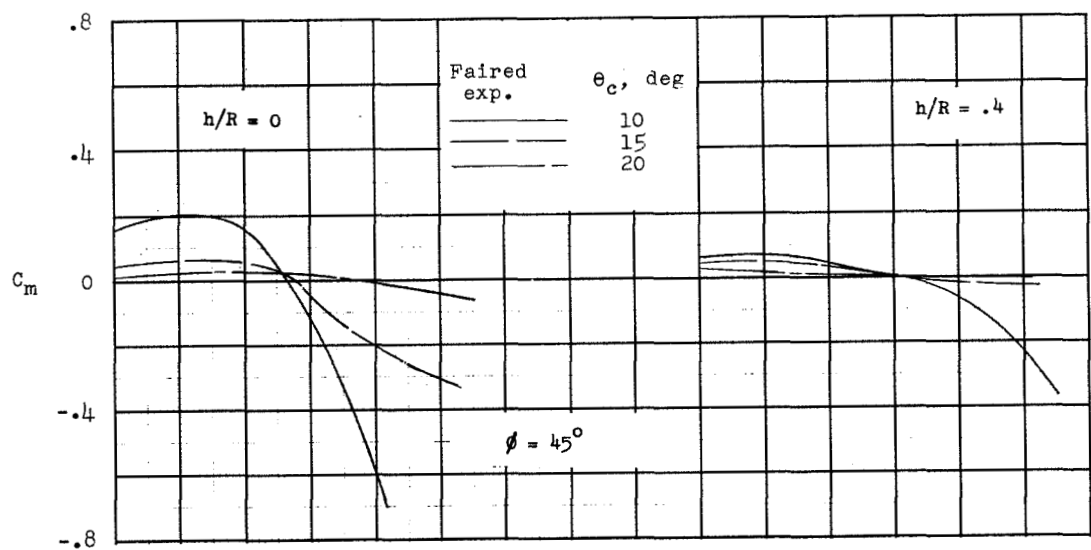


Figure 30.- Faired experimental pitching-moment characteristics about the body center of gravity of the conic-sectored series.

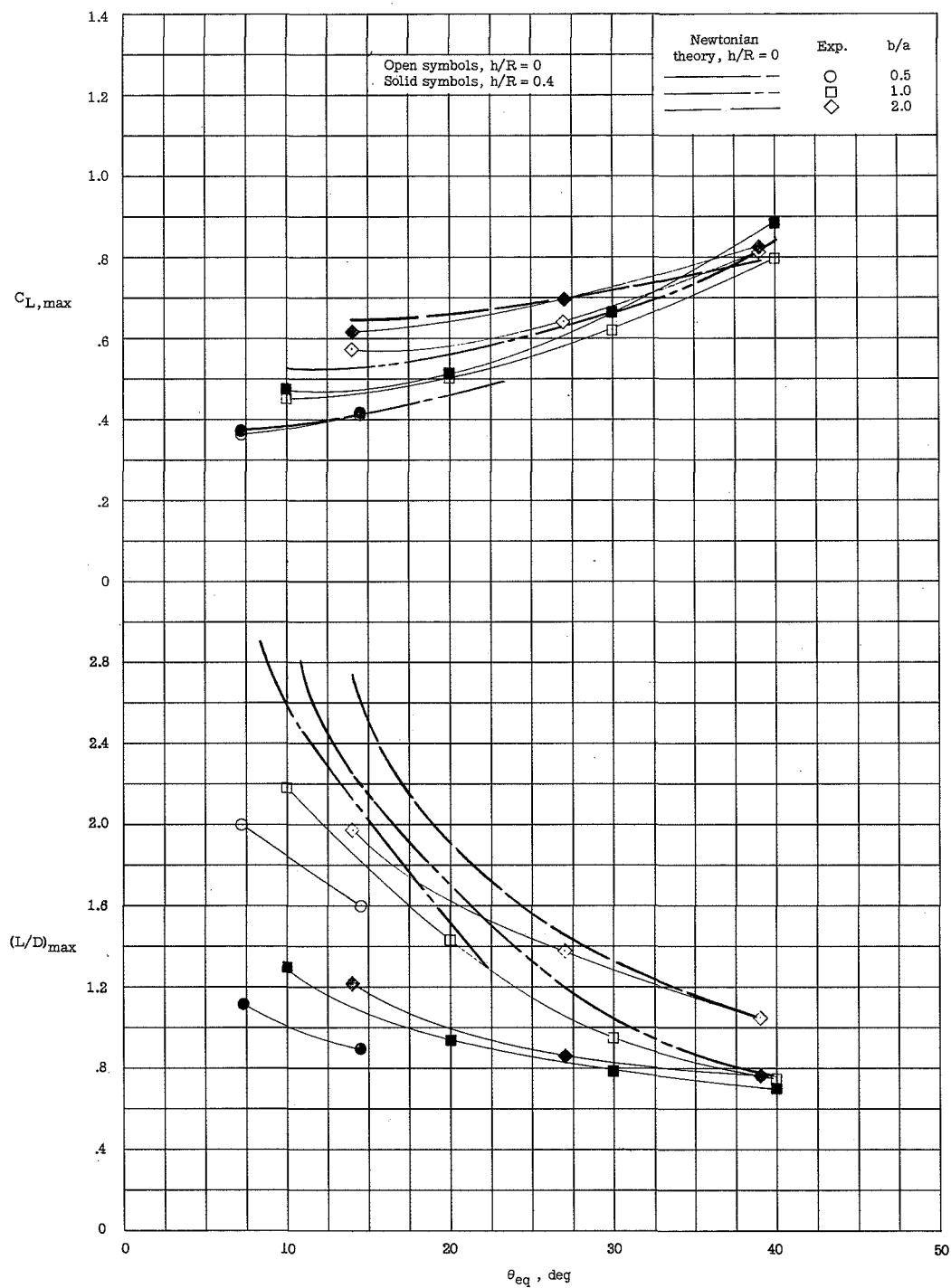


Figure 31.- Comparison of the effects of body span-height ratio on $C_{L,max}$ and $(L/D)_{max}$ of elliptic half-cone bodies of equal volume. ($C_{L,max}$ based on planform area.)

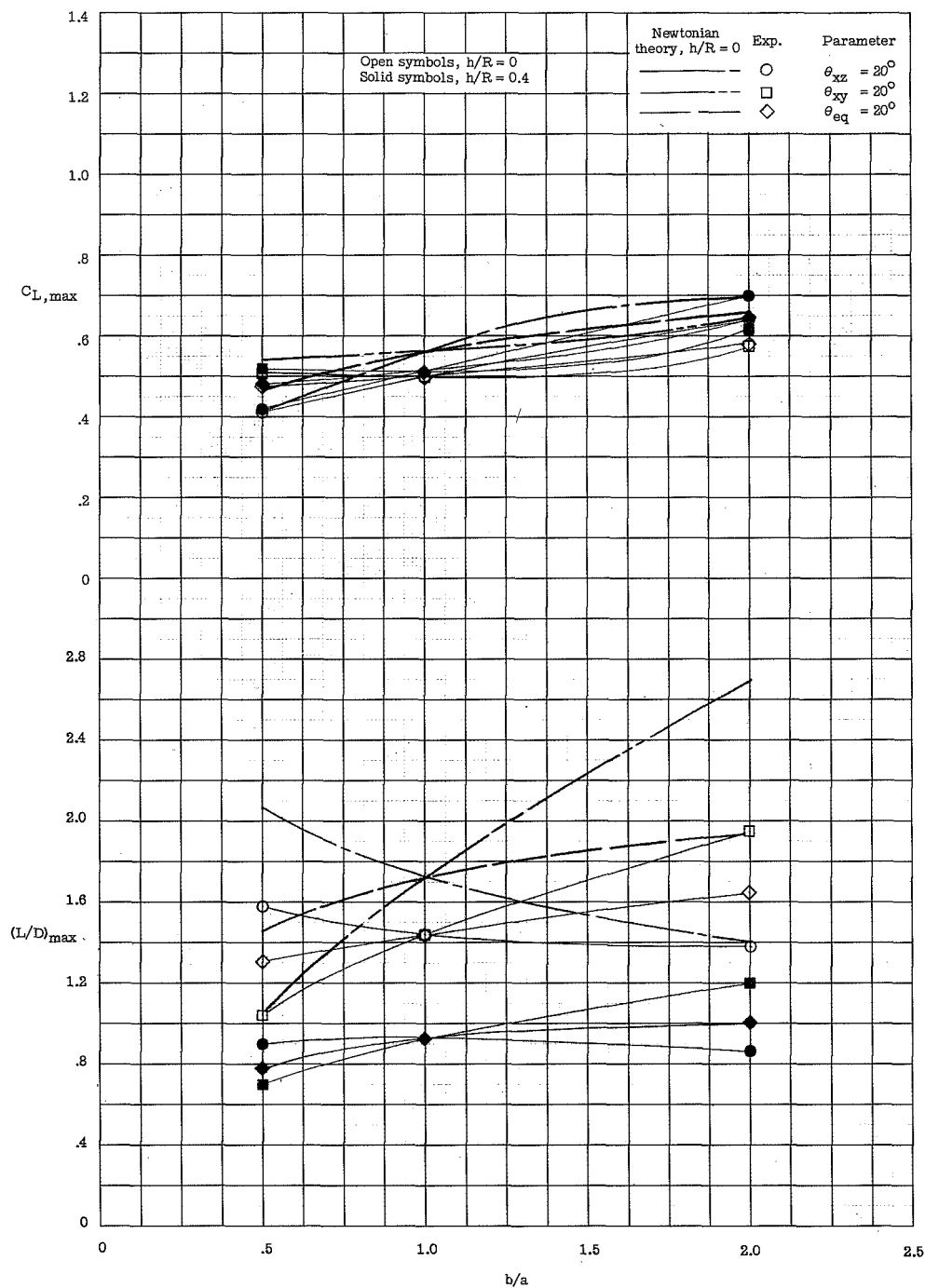
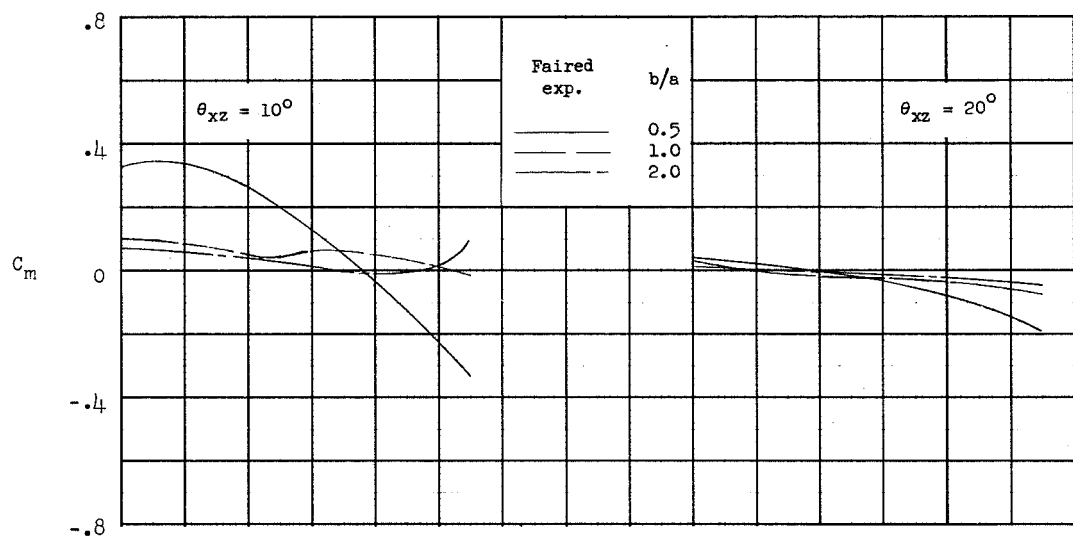
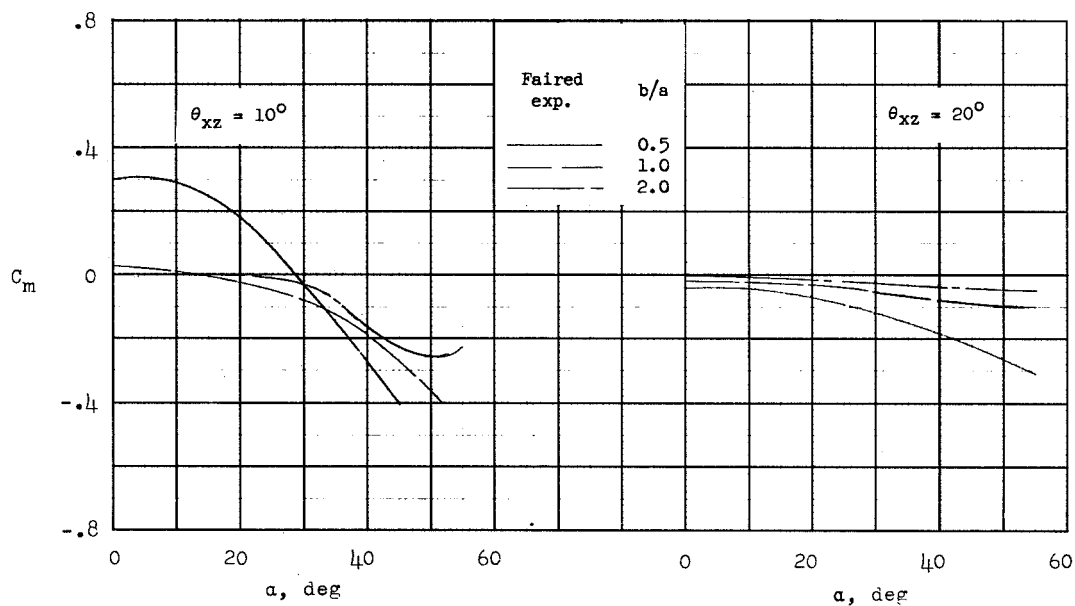


Figure 32.- Variation of $C_{L,max}$ and $(L/D)_{max}$ of a series of elliptic half-cones with span-height ratio. ($C_{L,max}$ based on planform area.)



$h/R = 0.4$



$h/R = 0$

Figure 33.- Faired experimental pitching-moment characteristics about the body center of gravity of the elliptic half-cone series.

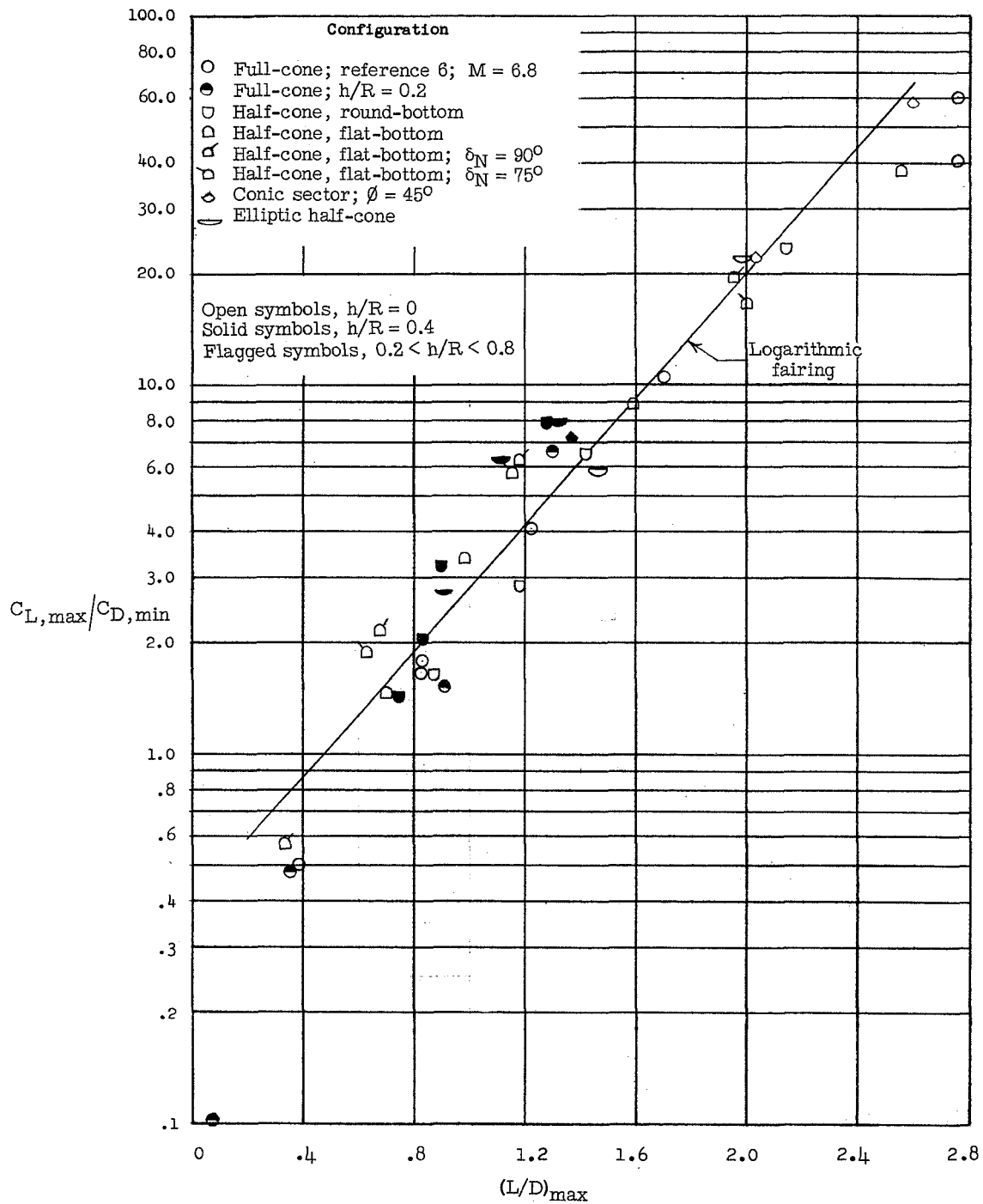


Figure 34.- Variation in the ratio $C_{L,max}/C_{D,min}$ with $(L/D)_{max}$ for a number of configurations of varying body cross section and nose bluntness.

